Dissolution-Precipitation in Porous Media: Experiments and Modelling

Inauguraldissertation der Philosophisch-naturwissenschaftlichen
Fakultät der Universität Bern

Vorgelegt von

Jenna Poonoosamy

von Mauritius

Leiter der Arbeit: PD Dr. Urs Mäder (Institut für Geologie)
Co-Leiter: PD Dr. Georg Kosakowski (Paul Scherrer Institut)
Co-Leiter: Dr. Luc R. Van Loon (Paul Scherrer Institut)
Koreferent: HDR Vincent Lagneau (Mines ParisTech)

Dissolution-Precipitation in Porous Media: Experiments and Modelling

Inauguraldissertation der Philosophisch-naturwissenschaftlichen
Fakultät der Universität Bern

Vorgelegt von

Jenna Poonoosamy

von Mauritius

Leiter der Arbeit: PD Dr. Urs Mäder (Institut für Geologie)
Co-Leiter: PD Dr. Georg Kosakowski (Paul Scherrer Institut)
Co-Leiter: Dr. Luc R. Van Loon (Paul Scherrer Institut)
Koreferent: HDR Vincent Lagneau (Mines ParisTech)

Von der Philosophisch-naturwissenschaftlichen Fakultät angenommen.

Der Dekan:

Bern, den 4. Januar 2016
Prof. Dr. Gilberto Colangelo

Acknowledgments

Financial supports:

The Swiss cooperative for disposal of radioactive waste (Nagra), and PSI are greatly acknowledged.

Swiss Light Source for providing beam time to analyse our samples.

This PhD thesis benefited from the professional contribution of many people:

Dr. Urs Mäder is thanked for sharing interest in this scientific work and his pertinent remarks.

Dr. Georg Kosakowski is thanked for initiating this project and for having given me the opportunity to take this PhD position despite my initial lack of knowledge in hydrology and reactive transport modelling. I also thank him for his pedagogy and patience.

Dr. Luc Van Loon for his interest in this work and keeping my motivation up.

Dr. Dmitrii Kulik who always shared his geochemical knowledge and excitement.

Dr. Enzo Curti for helping me to understand nucleation mechanisms and participation in my project.

Dr Daniel Grolimund for his measurement (µ-XRD and µ-XRF) at the Swiss light source and also for his excitement in the project.

Sabrina Frick for IC measurement.

Ekaterina Zapolnova for carrying out 1D column experiments.

Members of the rock-water interaction group at the University of Bern are warmly thanked: Thomas Aebi for the thin section preparation, Dr. Jebril Hadi for his assistance in resin impregnation, Priska Baehler for ICP-OES measurement, Cristine Lemp for assistance with powder XRD and BET measurement and finally Dr. Andreas Jenni for his assistance in SEM operation.

Dr Christoph Wanner, Dr. Peter Alt-Epping, Dr. Janvier Samper and Jesus Águila for their contribution to the SeS benchmark.

And finally Dr. Nikolaos Prasianakis for his interest in my work and the development of a pore scale model based on my experimental work.

LES members are greatly thanked for making my stay at PSI enjoyable:

I would like to thank Beatrice for her precious help, my supervisors who were encouraging and gave me sufficient freedom to test new things in the laboratory. I would also like to thank Mike and Tres for the English revision on my publications and Thomas who always carried my samples from PSI to Bern. I also thank Sergey Churakov, head of our laboratory for his encouragements. All LES members (Annamarie, Allan, Bruno, Amir, Louis, Urs, Wilfried and Urs…) who were always very helpful and provided a friendly environment for work.

Last but not least, many thanks to my family, especially my husband and parents.

Table of content

Abstract: 15

Chapter 1: Introduction 17

1. Motivation of this study 19

2. Overview of numerical and experimental benchmark 22

3. Material and Methods 26

3.1. Experimental Approach 26

3.2 Analytical techniques 29

3.2.1. Analytical techniques during the experiments 29

3.2.2. Analytical techniques for post-mortem analysis 29

3.3. Modelling approach 30

3.4. OpenGeosys-GEM 31

3.4.1. Flow and mass transport solver 32

3.4.2. Chemical solver 34

4. Outline of the thesis 36

References 38

Chapter 2: Dissolution-precipitation processes in tank experiments for testing numerical models for reactive transport calculations: Experiments and modelling 45

Abstract 47

1. Introduction 47

2. Material and methods 49

2.1. Experimental setup 49

2.1.1. Transport experiment without chemical reaction 50

2.1.2. Reactive transport experiment 50

2.1.3. Post mortem analysis 51

2.2. Numerical models 51

3. Results and discussions 53

3.1. Experimental results 53

3.1.1. Advective transport experiments 53

3.1.2. Reactive transport experiment 53

3.1.3. Mineral evolution in the tank 54

3.2. Summary of experimental results and their interpretation 55

3.3. Modelling results 58

3.3.1. Modelling the transport experiment with no chemical reaction 58

3.3.2. Modelling the reactive transport experiment 59

4. Summary and conclusions 60

Acknowledgments 60

Appendix A 61

References 62
Chapter 3: Barite precipitation following celestite dissolution in a porous medium: a SEM/BSE and μ-XRD/XRF study 65
Abstract 67
1. Introduction 68
2. Experimental Methods 69
2.1. Setup of reactive transport experiments (including fluid chemistry) 69
2.2. Analytical techniques (optical microscope/SEM/BSE/EDX) 71
2.3 Micro XRF and micro XRD measurement and data analysis 71
3. Results 72
3.1. Microscopic analysis 72
3.1.1. Optical microscopy 72
3.1.2. Scanning electron microscopy (SEM) 72
3.2. μ-XRF measurements 74
3.3. μ-XRD measurements 75
4. Interpretation 77
4.1. Thermodynamic and kinetic considerations 77
4.2. Application of classical nucleation theory 78
5. Conclusions and outlook 83
Acknowledgments 84
References 84
Appendix 84
Chapter 4: PSI - Reactive transport benchmark 89
1. Definition of the problem set-up 91
2. Description of the coupled code 94
3. Results 99
4. Summary 104
Annex 106
Erratum 109
References 110
Chapter 5: Dissolution precipitation reactions in a 2D setup for testing concepts of reactive transport codes 113
1. Introduction 115
2. Benchmark problem setup 118
3. Mathematical model formulations and numerical implementations 121
3.1. Numerical codes 121
3.1.1. OpenGeoSys-GEM 121
3.1.2. CORE2D 122
3.1.3. TOUGHREACT 122
3.1.4. Pflotran 122

3.2. Model formulations 122

3.2.1. Density Flow 122

3.2.2. Porosity, diffusivity and permeability 123

3.2.3. Activity corrections 124

3.2.4. Kinetics of precipitation and dissolution reactions of minerals 124

3.2.5. Solid solution 125

4. Results 129

4.1. Case 1 129

4.2. Case 2 132

4.3. Case 3a 133

4.4. Case 3b 135

4.5. Case 4 137

5. Conclusions 139

References 140

Appendix 145

Chapter 6: Concluding remarks and future work 147

Erklärung 159

CV 160

Abstract:

The evolution of porosity due to dissolution/precipitation processes of minerals and the associated change of transport parameters are of major interest for natural geological environments and engineered underground structures. We designed a reproducible and fast to conduct 2D experiment, which is flexible enough to investigate several process couplings implemented in the numerical code OpenGeosys-GEM (OGS-GEM). We investigated advective-diffusive transport of solutes, effect of liquid phase density on advective transport, and kinetically controlled dissolution/precipitation reactions causing porosity changes. In addition, the system allowed to investigate the influence of microscopic (pore scale) processes on macroscopic (continuum scale) transport. A Plexiglas tank of dimension 10 × 10 cm was filled with a 1 cm thick reactive layer consisting of a bimodal grain size distribution of celestite ($SrSO_4$) crystals, sandwiched between two layers of sand. A barium chloride solution was injected into the tank causing an asymmetric flow field to develop. As the barium chloride reached the celestite region, dissolution of celestite was initiated and barite precipitated. Due to the higher molar volume of barite, its precipitation caused a porosity decrease and thus also a decrease in the permeability of the porous medium. The change of flow in space and time was observed via injection of conservative tracers and analysis of effluents. In addition, an extensive post-mortem analysis of the reacted medium was conducted. We could successfully model the flow (with and without fluid density effects) and the transport of conservative tracers with a (continuum scale) reactive transport model. The prediction of the reactive experiments initially failed. Only the inclusion of information from post-mortem analysis gave a satisfactory match for the case where the flow field changed due to dissolution/precipitation reactions. We concentrated on the refinement of post-mortem analysis and the investigation of the dissolution/precipitation mechanisms at the pore scale. Our analytical techniques combined scanning electron microscopy (SEM) and synchrotron X-ray micro-diffraction/micro-fluorescence performed at the XAS beamline (Swiss Light Source). The newly formed phases include an epitaxial growth of barite micro-crystals on large celestite crystals (epitaxial growth) and a nano-crystalline barite phase (resulting from the dissolution of small celestite crystals) with residues of celestite crystals in the pore interstices. Classical nucleation theory, using well-established and estimated parameters describing barite precipitation, was applied to explain the mineralogical changes occurring in our system. Our pore scale investigation showed limits of the continuum scale reactive transport model. Although kinetic effects were implemented by fixing two distinct rates for the dissolution of large and small celestite crystals, instantaneous precipitation of barite was assumed as soon as oversaturation occurred. Precipitation kinetics, passivation of large celestite crystals and metastability of supersaturated solutions, i.e. the conditions under which nucleation cannot occur despite high supersaturation, were neglected. These results will be used to develop a pore scale model that describes precipitation and dissolution of crystals at the pore scale for various transport and chemical conditions. Pore scale modelling can be used to parameterize constitutive equations to introduce pore-scale corrections into macroscopic (continuum) reactive transport models. Microscopic understanding of the system is fundamental for modelling from the pore to the continuum scale.

Chapter 1: Introduction

1. Motivation of this study

Water-rock interactions are important processes that govern the evolution of many natural and engineered subsurface systems. These interactions include, among others, the precipitation and dissolution of minerals which also alters the rock porosity. As pore space geometry, pore connectivity, pore radii and pore shapes define the transport of fluids and solutes, the alteration of porosity also modifies the transport properties of the rocks.

Porosity changes are involved in complex interactions between physical and (bio) chemical processes. The understanding of porosity evolution is important and widely studied, as this is a key factor for the behaviour or performance of natural and engineered systems in the underground.

- Precipitation of minerals such as carbonates, silicates, sulphates and phosphates of calcium, barium and magnesium are commonly found in the subsurface. They can cause a significant reduction in porosity and permeability by plugging pore throats of aquifer and reservoir media (Saripalli et al., 2001).
- During bioremediation, pore space clogging due to mineral precipitation as well as gas production by microbial activity, can lead to a reduction of the effective porosity and hydraulic conductivity (Seifert and Engesgaard, 2012; Thullner et al., 2002). This decreases the efficiency of bioremediation of polluted groundwater.
- During injection of CO_2 into geological formations, the CO_2 mixes with ground waters (or brines) and interacts with rock minerals. It is expected that the binding of CO_2 in newly formed mineral phases causes significant changes in porosity and permeability (Cailly et al., 2005).
- Porosity changes due to mineral precipitation/dissolution are also being actively investigated in connection with the deep geological disposal of nuclear waste. In such installations chemically very different materials such as clays and concretes, come into contact (Gaucher and Blanc, 2006). At interfaces between cement based materials and clay based materials or clay host rocks the mixing of pore waters will lead to the dissolution and precipitation of minerals and might result in pore clogging after long times (Jenni et al., 2014; Gaboreau et al., 2012; Dauzeres et al., 2010).
- Permeable reactive barriers (PRB) are used for the remediation of contaminant water. The PRB concept for remediation of contaminant water involves the emplacement of a reactive medium perpendicular to the trajectory of the contaminant plume. As the contaminant plume passes through the reactive medium, processes involving precipitation/dissolution takes place leading to less harmful compounds. PRB can operate several decades exhausting the reactivity of the reactive material. However the efficiency of PRB is further reduced by clogging. Clogging through secondary mineral precipitation in the pore space decreases the hydraulic conductivity of the barrier, reducing flow through the barrier (Mackenzie et al., 1999).

The investigation of many natural and artificial geo-systems in which the coupling of chemical reactions and transport is important, is often done with help of reactive transport models as information on their evolution in time and space is scarce. The applications of reactive transport models include geothermal systems (Alt-Epping et al. 2013a; 2013b; Wanner et al., 2014;

Diamond and Alt-Epping, 2014), nuclear waste repositories (De Windt et al., 2004, Gaucher and Blanc, 2006; De Windt et al., 2007; Kosakowski and Berner, 2013; Berner et al., 2013), geologic carbon dioxide storage (Class et al., 2009; Bildstein et al., 2010), and environmental remediation (Wanner et al., 2012; Jamieson-Hanes et al., 2012; Wanner and Sonnenthal, 2013).

The numerical models for reactive transport are typically based on a continuum approach using a representative elementary volume (REV) (Bear, 1972). A continuum description of rock properties is applied i.e. chemical and physical variables are locally averaged over a REV. This is because field scale simulation using pore-scale description of solute transport and precipitation-dissolution reactions are computationally expensive (Scheibe et al., 2015).

Modern reactive transport models solve complex couplings between chemical reactions, water saturation, mechanical deformation, heat transport and changes of material properties such as rock diffusivity and permeability. Although the numerical models are capable of investigating such systems, the application of these codes to real systems is hampered by one major problem: the coupling between chemistry and changes in material properties (porosity, diffusivity, saturation, permeability, dissolution/precipitation kinetics and specific surface areas). System-dependent coupling parameters, such as kinetic rates, effective surface areas and porosity-permeability relationships must be provided by independent measurements or other data sources. Such data are often not available, such that empirical relationships and parameters have to be used. In fact, changes in porosity also change other material parameters which in reality depend on more complicated pore space changes that are not included in the “porosity” and cannot be calculated with continuum approaches.

Porosity changes due to precipitation/dissolution reactions, and their feedback on transport properties, are accounted in numerical models by considering empirical formulae: Kozeny-Carman for porosity/permeability (Carman, 1937), and Archie's law for porosity/diffusivity (Archie, 1942). These empirical laws need to be parameterised, either experimentally (e.g., Boving and Grathwohl, 2001; Van Loon et al., 2007; Marica et al., 2011), or by up-scaling from micro-scale models (e.g., Liu et al., 2014; Tyagi et al., 2013). It is however worth stating that these studies did not focus on porosity evolution due to mineral dissolution or precipitation.

Well-defined experiments can be used to evaluate porosity (and thus transport properties) induced by mineral precipitation and dissolution. These experiments along with testing numerical models gives insight on how to upscale microscopic data/model for use in the continuum scale models. A fundamental understanding on the sub-continuum scale processes (in the pore space) is needed to overcome experimental parameterization of permeability-porosity and diffusivity-porosity or other porosity dependent laws. Studies combining a macroscopic experiment with microscopic understanding are rare (e.g. Tartakovsky et al., 2008, specific to mixing induced precipitation systems) and incomplete considering only modelling work (e.g. Cochepin et al., 2008 where the experiments were not carried out).

In this context, we propose a reactive transport experiment involving porosity changes that could be used to test numerical models. Our approach will also focus on a microscopic investigation of the system that gives insight on the pore scale processes involved. This information can at a later stage be used for upscaling to the continuum scale.

The objectives for this thesis are:

- Develop an experimental benchmark for porosity change in a porous medium due to mineral dissolution/precipitation reactions.
- The experiments should be fast, reproducible and with simple chemical set up. The system should be flexible enough to test the influence of various transport process on the porosity change.
- Investigate in detail the evolution of the pore space and gain microscopic understanding of processes that drive the pore space changes. This is important for testing of continuum scale models.
- Model the experiments with a reactive transport code (OpenGeosys-GEM) based on the continuum approach.
- Propose a benchmark for the SeS initiative (Steefel et al., 2015) and compare the numerical simulations of the reactive transport code OpenGeoSys-GEM with other reactive transport codes.

2. Overview of numerical and experimental benchmark

There is a need to evaluate the capabilities, the correctness of the implemented features and the performance of reactive transport codes. This process is called “benchmarking” and is normally done by comparing model results with analytical solutions, by reproducing results from laboratory or field experiments and by code inter-comparison.

Finding the exact solution for simplified 1D and 2D systems is important to test the correctness of the numerical implementation of reactive transport codes. Analytical solutions for problems coupled with porosity changes are few. The only investigations on this topic include Lagneau and van der Lee (2010a), and Hayek et al., (2011, 2012). Lagneau and van der Lee (2010a) proposed an analytical solution for a one dimensional system containing one species and one mineral. The analytical solution was used to verify implementation of porosity change in the reactive transport code HYTEC (van der Lee, 2003). Their solution was only applicable to small and moderate porosity changes. Hayek et al., (2011) developed analytical solutions for a 1-D coupled diffusion-reaction problem with feedback on porosity change for benchmarking reactive transport. Their numerical experiment consisted in the precipitation of a solid phase from two aqueous species inside a porous medium leading to strong porosity reduction and even clogging. They proposed analytical solutions that are only suitable for non-equilibrium chemistry. Good agreement between numerical and analytical solution was obtained when sufficient spatial and temporal discretization was used for the numerical solution. Their study also demonstrated, in agreement with Lagneau and van der Lee (2010a) that numerical codes with explicit schemes did not always converge to the analytical solution. Only implicit schemes produced accurate solutions independent of time stepping. Analytical solutions describing transport of several aqueous species coupled to precipitation and dissolution of a single mineral in two and three dimensions with porosity change were proposed by Hayek et al. (2012).

Testing of the correct implementation of single processes by comparison with analytical solutions is a standard approach during code development. Testing of the correctness and predictive capabilities of codes and the implemented concepts, the so called model validation (Refsgaard and Henriksen, 2004), is mainly done in benchmarks that are developed during organized benchmarking initiatives.

Several international projects have been devoted to model validation. The international projects (INTRACOIN, HYDROCOIN, INTRAVAL and GEOVAL) in the early 1980’s were created to build confidence on the use of performance assessment models and associated conceptual models and mathematical codes in assessing the safety of nuclear waste repositories (Larson, 1992). The objectives were to investigate the possible implications that the coupling of various physico-chemical phenomena and different solution algorithms have on transport calculations.

An international cooperative project DECOVALEX was initiated in 1992 and aims to advance the understanding and modelling of coupled thermo-hydro-mechanical-chemical (THMC) processes in geologic systems foreseen for the disposal of radioactive waste (Tsang et al., 2005). The objective of the initiative is to propose hypothetical problems, as well as laboratory and field experiments that are used to advance the state of mathematical modelling for coupled THMC processes in fractured rocks and buffer material. Analytical and semi-analytical solutions to coupled problems were also developed. The characteristic of the DECOVALEX project is that each proposed case study is modelled by different research teams, using their own approaches, conceptual models and computer codes. The comparison of the results from these teams give insight on the effect of the coupled THM processes, the strength, the weaknesses and adequacies of the various approaches and computer codes.

The MoMas initiative (Modelling, Mathematics and numerical Simulations related to nuclear waste management problems), is not based on code evaluation with experiments or analytical solution, but focuses on the efficiency of numerical codes as well as the evaluation of different numerical couplings between transport and chemistry. The major objective of the MoMas initiative is to provide more efficient numerical methods and mathematical solution schemes in order to improve reactive transport models, in particular for applications in the domain of deep underground radioactive waste disposal (Lagneau and van der Lee, 2010b). Carrayou et al. (2010) proposed a benchmark within the MoMas initiative where different coupling schemes for reactive transport were tested: sequential non-iterative approach (SNIA) based on transport operator splitting and no iteration between transport and chemistry, sequential iterative approach (SIA) where transport is solved first, then chemistry with iteration between the two processes until concentration on certain locations reaches convergence, and global methods based on implicit schemes where transport and chemical reactions are solved simultaneously. The main outcome of their benchmark was that all approaches were able to solve the benchmark test cases and captured the characteristic features both in time and space with some localized differences. With the same perspective, another benchmark was used to investigate different coupling schemes within the same code. Samper et al. (2009) implemented and tested the sequential partly iterative approach (SPIA) against SNIA and SIA in CORE2D V4. In SPIA, the iteration between transport and chemistry is performed only in nodes with large mass transfer between solid and liquid phases. The authors demonstrated that SPIA produces more accurate results than SNIA. Usually, the computation time for SNIA is much less than SIA but the numerical solutions obtained with SNIA are less accurate than SIA solutions with more numerical dispersion. SNIA errors depend on the type of chemical reactions and the grid Peclet and Courant numbers.

Recently an initiative for benchmarking Subsurface Environmental Simulation methods (SeS bench) was created with a focus on reactive transport processes. Its aim is to use numerical benchmarks to test specific existing and new concepts of reactive transport codes (Steefel et al., 2015).

Several of the proposed benchmarks involved porosity change due to mineral precipitation/dissolution reactions (Perko et al., 2015, Xie et al., 2015). Specifically the benchmark described in Xie et al. (2015) investigated the implementation of the Kozeny-Carman equation as porosity-permeability relationship and Archie’s law as porosity-diffusivity relationship in reactive transport codes by inducing porosity changes by mineral precipitation and dissolution. The benchmark considered different processes influencing the mineral reactions including advective-dispersive transport in saturated media and kinetic control of mineral precipitation and dissolution rates. Results from different reactive transport codes (HP1, MIN3P, Pflotran and TOUGHREACT) showed good agreement of the predicted mineral assemblage and clogging locations while absolute values of mass fluxes differed substantially. The differences could be attributed to differences in implementation of permeability-porosity and tortuosity-porosity relationships, different activity correction models, and numerical methods (e.g. spatial weighing schemes). Their results also highlighted the difficulties to simulate problems with pore clogging.

A benchmark that evaluates the influence of porosity change on transport parameters such as diffusivity and permeability was already proposed earlier. Cochepin et al. (2008) proposed a numerical benchmark which involved the replacement of a primary mineral phase (portlandite) by a secondary mineral phase with a larger molar volume (calcium oxalate) that could lead to porosity clogging. A reactive layer of portlandite was sandwiched between two layers of sand assumed to be unreactive during the simulation as shown in Fig. 1. An asymmetric injection of a reactive fluid caused a spatially heterogeneous porosity change with subsequent changes to the flow field. Cochepin et al. (2008) made a comparative study of this numerical benchmark using Crunch (Steefel et al., 2005) and Hytec (van der Lee et al., 2003). The results given by the two codes were in fairly good agreement. Discrepancies were explained by the different models used for describing the reactive surface area of precipitating and dissolving minerals. It should be stressed that it was originally planned to also experimentally implement this setup, but these plans were never realised.

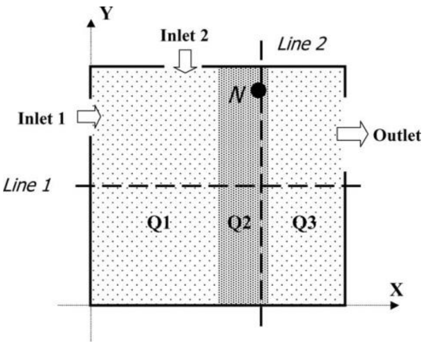

Fig. 1: Geometry of the experiment proposed by Cochepin et al., (2008). Q2 is the reactive media consisting of portlandite. Q1 and Q3 are inert quartz media. Inlet 2 and inlet 1 supply sodium chloride and sodium oxalate, respectively.

In addition, simple laboratory experiments are gaining interest for the evaluation of specific concepts of reactive transport codes. Lagneau (2000) conducted column experiments to investigate the feedback of porosity changes on transport parameters in both diffusive and advective regimes. Porosity change was forced by the injection of a reactive solution which triggered the replacement of a primary mineral phase by secondary mineral phases of larger molar volumes. The advective experiments consisted of the ingress of mildly acidic zinc sulphate into a porous medium of calcite which resulted in the formation of gypsum ($CaSO_{4(s)}$) and smithsonite ($ZnCO_{3(s)}$). In their diffusive system, the porous medium was replaced by portlandite ($((CaOH)_2)$) which after reaction was transformed to gypsum and zinc hydroxide ($Zn(OH)_2$). These experiments were used to test the feedback between chemistry and transport in the reactive transport code Hytec.

Tartakovsky et al. (2008) not only compared laboratory experiments with reactive transport models, but also investigated the micro-structure of the pore space changes and used this information to modify the continuum scale description of reactive transport. The experiments conducted by Tartakovsky et al. (2008) involved the uniform parallel injection of two reacting solutions into a cell filled with quartz grains. This created a uniform flow field with mixing (diffusive and dispersive) at the interface of the two reacting solutions. They observed the formation of a narrow zone of calcite precipitate with a uniform width of less than 5 mm along the middle of the cell. The pore scale modelling of the system revealed large pore scale concentration gradients. Continuum (Darcy) simulations based on the commonly used advection-dispersion reaction equation (ADRE) showed that only a model with grid sizes in the mixing zone smaller than the size of the quartz grains could reproduce the main features of the experiment. As an alternative to high resolution simulations, the ADRE was modified to include transport and mixing indices in the reaction terms. These parameters account for highly non-uniform pore scale concentration gradients and localised precipitation at the sub-grid scale.

Katz et al. (2011) proposed an experiment similar to that of Tartakovsky et al. (2008). The authors triggered the precipitation of calcite in homogeneous and heterogeneous media by the injection of sodium bicarbonate and calcium chloride (matched to the same density) through parallel inlets into the flow cell. They successfully reproduced the conservative transport of solutes with an ADRE based model, but the ADRE based reactive transport model failed to reproduce porosity clogging and measured concentrations at the sampling ports. These results - in agreement with those from Tartakovsky et al. (2008) - suggested the inappropriateness of using the ADRE in the continuum models to predict pore scale reactions.

3. Material and Methods

3.1. Experimental Approach

Our aim is to design a reactive transport experiment where a porosity decrease is induced by mineral precipitation. The experiments should be fast and reproducible and with a simple chemical setup. The system should be flexible enough to test the influence of various transport process on the porosity change.

We conducted our experiments in a plexiglas tank of 10 cm × 10 cm and 1 cm width as shown in Fig 2. The tank was filled with celestite ($SrSO_4$) sandwiched between two layers of quartz (SiO_2).

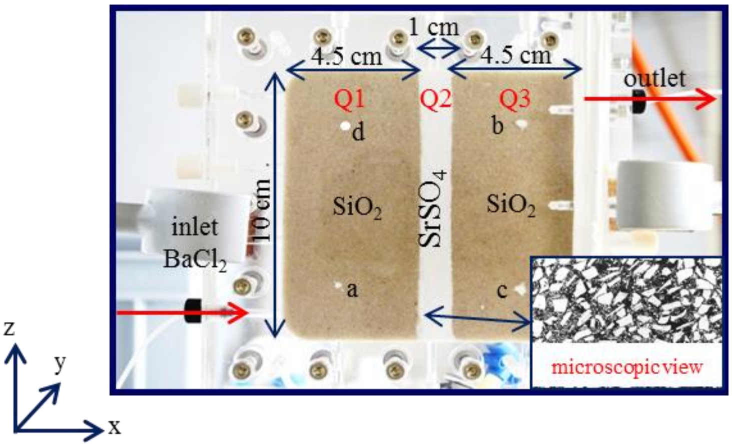

Fig. 2: Experimental setup.

The choice of the chosen set-up can be explained as follows:

- **Porous media:** For the purpose of testing reactive transport codes, complex media with complicated pore structure and slow transport/alteration are often difficult. Clogging at clay/cement interfaces is particularly interesting for the safety of nuclear waste repositories, however, experiments involving transport in clay and cement media are difficult to conduct at the laboratory scale in a short period of time, as slow diffusive processes are involved. Furthermore, the pore size distribution in clay media covers many orders of magnitudes down to nanometres. Pore space changes might be difficult to observe. Instead a system involving a simple porous medium, sand, was chosen. In addition, a porous medium composed of grains offers the flexibility of varying pore sizes by the mechanical mixing of different grain sizes or having a homogeneous pore size distribution by considering grains that are of a similar size. In case of spherical grains like sand, pore size can be varied without changing the global porosity of the medium just by varying the size of grains.

- **Inducing precipitation:** One possibility was to consider mineral precipitation induced by injecting two reacting solutions into a porous medium. This would lead to a sharp precipitation front of a few µm which was already investigated by (Tartakovsky et al. 2008). A second option was to dissolve a primary mineral which would be replaced by a secondary mineral of larger molar volume as was done by Lagneau (2000). This has several advantages including the possibility of tuning several parameters such as initial porosity of the system for a sharper porosity decrease. In addition, in such a setup, concentration gradients can also be controlled by the dissolving phase. For these reasons we opted for a mineral replacement reaction in porous media.

- **Transport regime:** A purely diffusive transport regime in sand (relatively high permeability) is difficult to realize, as small pressure differences between the reservoirs of reactants might induce advective flow. In addition, the solution with reactants might have a significant higher density than the equilibrium solutions and could therefore disturb the transport regime by inducing density driven flow. Advection might allow an easier control of the flux of reactants. The reaction can be controlled by transport or by the precipitation/dissolution kinetics. Advective transport will allow larger fluxes of reactants whereas in a diffusive regime, the diffusion coefficients and concentration gradients in the medium control the flux which would lengthen our experiment.

- **Geometry setup:** A 1D setup involving mineral precipitation and dissolution with an advective flux was already tested by Lagneau (2010). We thus considered a 2D setup based on the numerical setup proposed by Cochepin et al. (2008). The geometry of their 2D setup (shown in Fig. 1) with a portlandite layer (Q2) in between 2 layers of sand (Q1 and Q3) had the main advantage of a non-uniform porosity/permeability decrease which would allow visualization of the changes in flow path as transport properties of the reactive media change. For visualization purposes, we chose an acrylic (plexiglas) containment for our reactive transport experiment.

  In the Cochepin et al. (2008) numerical setup, two inlets and one outlet were positioned as shown in Fig. 1. Inlet 2 allowed an inflow of sodium oxalate solution which would dissolve portlandite and precipitate calcium oxalate. Inlet 1 ensured the dissolution of the portlandite and newly formed calcium oxalate by an inflow of sodium chloride. In practice, this setup has the advantage of inhibiting fractures after clogging in the Q2 region. However monitoring the simultaneous dissolution and precipitation of calcium oxalate will present some inconvenience for understanding the kinetics of dissolution/precipitation of the system. The system was thus simplified by the choice of 1 inlet and 1 outlet positioned as shown in Fig. 2. The positioning of the inlet at the lowest and outlet at the upper most part ensured a complete and constant saturation of the porous medium.

- **Chemical setup:** We had to adapt the chemical reaction involved in Cochepin et al. (2008) as the one they proposed would involve the dissolution of sand (assumed unreacting in their numerical model) by a highly alkaline leaching solution derived from portlandite. In addition, the chemicals involved had to be compatible with the containment (i.e. plexiglas) which narrowed our choice. For instance, the replacement of barium fluoride by calcium fluoride involving a volume increment of ~ 22% was rejected as fluoride ions involved in the reaction would also react with plexiglas. We thus opted for the replacement of celestite ($SrSO_4$) by barite ($BaSO_4$). The volume increment involved is ~ 12%. In order to reach complete clogging (replacement of all $SrSO_4$ by $BaSO_4$), the initial porosity of the porous medium should be 0.1. The chemical reaction considered is as follows:

$$BaCl_{2(aq)} + SrSO_{4(s)} \rightarrow BaSO_{4(s)} + SrCl_{2(aq)} \qquad (1)$$

The advantage of using barium and strontium sulphate minerals is that their kinetics of dissolution and precipitation has been widely studied (Liu and Nancollas, 1976; Campbell and Nancollas 1969; Dove and Czank, 1995; Prieto et al., 1997). Also its precipitation in porous media has also been the subject of several studies (Prieto et al.; 1990; Prieto et al., 1993; Putnis et al., 1995; Sánchez-Pastor et al., 2005; Sánchez-Pastor et al., 2006). A literature review on their work and their findings is given in chapter 3.

A naturally occurring celestite from Madagascar, which comes in form of polished stones, was used. The natural celestite was analysed by X-ray diffraction which revealed a purity of 99.7% and 0.3% of anhydrous calcium sulphate. The stones were crushed and sieved to give batches of different grain size. Unlike sand grains, strontium celestite grains are not spherical, but more brick-shaped. In order to further decrease the initial porosity of the reactive medium, particles of different grain sizes were mixed: ~ 30wt.% with a size less than 63 µm and ~ 70wt.% with a size of 125 – 400 µm. This resulted in a heterogeneous pore size distribution in the reactive medium. The strontium sulphate was compacted to a porosity of 0.33. The dissolution of 1 mol of $SrSO_4$ followed by the precipitation of 1 mol of barium sulphate results in a volume increase of 5.85 mL and thus in a decrease in the porosity from 0.33 to 0.25 within the reactive medium. It should however be noted that the global porosity does not give any information about pore space geometry and connectivity.

The use of commercial celestite was rejected. The latter comes in forms of pellets consisting of agglomerated particles of strontium sulphate which made its grinding and compaction difficult. In addition the injection of water in a porous material consisting of compacted commercial celestite material immediately induced cracks. Grinded natural celestite stones offered more mechanical stability.

The concentration of $BaCl_2$ should be high enough to allow a fast reaction but low enough such that its modelling with the Extended Debye Huckel activity model (see section 3.4.2.) valid for 1 - 2 Molal (mol kg^{-1}) solution, can still be used. A 0.3 M $BaCl_2$ solution was injected.

- **Flow rate:** The flow rate was set such that it allowed a complete exchange of the pore solution within 24 hours (20 µL min^{-1}). This facilitates monitoring of the experiment. 0.3 M of barium chloride solution was injected which would allow a complete replacement of $SrSO_4$ by $BaSO_4$ within 430 hours if the reaction were to take place under thermodynamic equilibrium (no kinetics involved) and complete with complete mixing.

The chosen experimental setup complied with all predetermined requirements: fast to conduct, reproducible, simple chemical setup, but still flexible in order to allow the investigation of several processes.

After reaction, but before dismantling the tank, isopropanol was injected in order to stop further chemical reactions. The reacted celestite medium was found to be solidified into a rectangular block. The reacted media was dried and impregnated under vacuum with Araldite XW396/XW397. An extensive post mortem analysis of the reacted celestite layer was performed with different techniques (see section 3.2.2.).

3.2 Analytical techniques

3.2.1. Analytical techniques during the experiments

Dye tracer tests: In order to make the flow field visible, and to detect any inhomogeneity in media packing or preferred flow paths along the Plexiglas walls, we injected a pulse (0.5 mL) of a dye tracer (Eosine 3 g L^{-1}) at the inlet followed by a continuous inflow of solution. Eosine acquires a negative charge under our experimental conditions (pH 5.6) and does not sorb on the negatively charged sand grains and was thus used as a conservative tracer in the beginning of the experiment.

It should be noted that because of the large uncertainties in the experimental tracer concentration calibration w.r.t its colour, the tracer tests were used for qualitative comparison only. Colour changes were only used to get a rough estimate of dispersion length (see section 3.4.1.).

Pressure measurements: Tubes with inner and outer diameters of 0.5 mm and 1.5 mm, respectively, were inserted through the ports at the back of the tank and fixed with silicon glue to the front face of the tank. Two tubes (a and b) were connected to pressure sensors (PX26-001DV, Omega Engineering Inc.) which allowed to measure pressure differences from 0 mbar (0 Pa or 0 cm hydraulic head) to 70 mbar (7000 Pa or 70 cm hydraulic head) with a sensitivity of 0.1 mbar (10 Pa or 0.1 cm hydraulic head). The differential pressure between ports “a” and “b” was also monitored.

Sampling: The outlet ports (c and d) were used for sampling. The concentration of ions (Cl^-, SO_4^{2-}, Ba^{2+} and Sr^{2+}) were measured by ion chromatography (DIONEX, DX500). Sampling from the ports disturbs the flow field and also the spatial/temporal distribution of concentrations throughout the tank because liquid is removed from the system. To minimise this interference, the sampling volumes were kept as small as possible (100 µL) and time gaps of 24 hours were set between samplings. The sampling of the effluents at the outlet port enabled the net mineral transformation in the tank to be evaluated.

3.2.2. Analytical techniques for post-mortem analysis

X-ray fluorescence (XRF): X-ray fluorescence is a non-destructive analytical technique used to quantify the elemental composition of a sample. We use this technique to determine where the mineral transformation has occurred in the reactive layer i.e. to localize the barium rich phases by making elemental maps.

Scanning electron microscopy (SEM): The scanning electron microscope (SEM) uses a focused beam of high-energy electrons to produce a variety of signals at the surface of solid samples. The signals reveal information about the morphology, chemical composition, and crystalline structure of materials of the sample. Our SEM measurements include mainly the use of secondary electrons and backscattered electrons for imaging samples. Secondary electrons give the morphology and topography while backscattered electrons (BSE) are mainly used to demonstrate the contrast in composition of the mixed phases in the sample. Because of their greater cross-sectional area, larger atoms with a greater atomic number, (Ba in our system) have a higher probability of producing an elastic collision. The number of BSE detected is proportional to the mean atomic number constituting the sample. As a result, a "brighter" and "darker" BSE intensity correspond to an element of greater and lower atomic number respectively. BSE images provide high-resolution compositional maps of our sample and for discrimination between Ba rich and Sr rich phases.

X-ray diffraction (XRD): X-ray diffraction is a technique destined to characterise crystalline materials. It provides information on the structure, phases and crystallographic orientations as well as structural parameters such as cell parameters, the crystallography, strains and defects of crystals. X-ray diffraction peaks are produced by the constructive interference of a beam of monochromatic X-ray diffused at angles specific to the family of lattice planes that constitutes the sample. We included powder and synchrotron XRD in our analytical techniques. We first conducted powder diffraction analysis from crushed samples of the reacted celestite as well as from the sand compartment to determine the new crystalline phase present. We also conducted synchrotron XRD to determine if there was any amorphous phase or solid solution of strontium and barium sulphate present.

3.3. Modelling approach

Two different approaches are used to describe liquid flow, solute transport and chemical reactions in a porous medium; the microscopic approach and the macroscopic approach.

The **microscopic approach** considers detailed structural information of the porous media as input, i.e. mineral crystal geometry, pore size distribution, tortuosity. With current progress in calculation power, it is nowadays possible to resolve problems (flow, transport, perturbation, etc.) with microscopic models (Molin et al., 2011). However, such a description becomes difficult as the size of the system increases and many pore volumes become involved. Calculations at the scale of our experimental tank are still out of reach. In addition it is experimentally difficult to measure the complete pore space in a tank without disassembling it and drilling cores of 5 mm maximum diameter for obtaining the necessary spatial resolution of a few µm. We will therefore model the system in a more convenient way, i.e. with a macroscopic scale approach.

In a **macroscopic/continuum description**, a heterogeneous porous medium is approximated by a representative elementary volume (REV), i.e. by a volume that provides a meaningful statistical average of the microstructural properties of the porous medium (Bear, 1972). The REV is much smaller than the size of the entire flow domain but large enough so that it includes a sufficient number of pores to permit a meaningful statistical average required in the continuum concept as shown in Fig. 3.

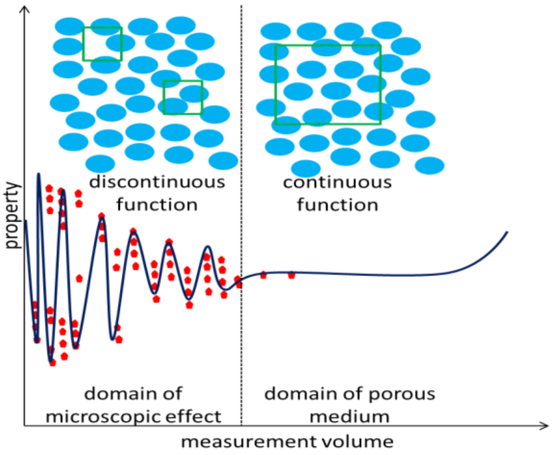

Fig. 3: Representative elementary volume concept (Bear 1972).

Our reactive transport experiment is modelled based on the continuum approach with the reactive transport code OpenGeosys-GEM.

3.4. OpenGeosys-GEM

The fluid flow and mass transport equations are solved by OpenGeoSys, and the chemical processes by the GEMS3K kernel code of GEM-Selektor V3 (Kulik et al., 2013). The coupling of these two codes is referred as OpenGeoSys-GEM, and its capabilities are described in Shao et al. (2009) and Kosakowski and Watanabe (2014). Mass transport and chemical reactions are solved in a sequential non-iterative approach (SNIA), i.e. first the transport equation is solved and then the reaction is solved by the chemical solver. The results are used as the output for this time step. The coupling of the processes in OpenGeoSys-GEM is given in Fig. 4, of which a detailed explanation is given in Shao et al. (2009).

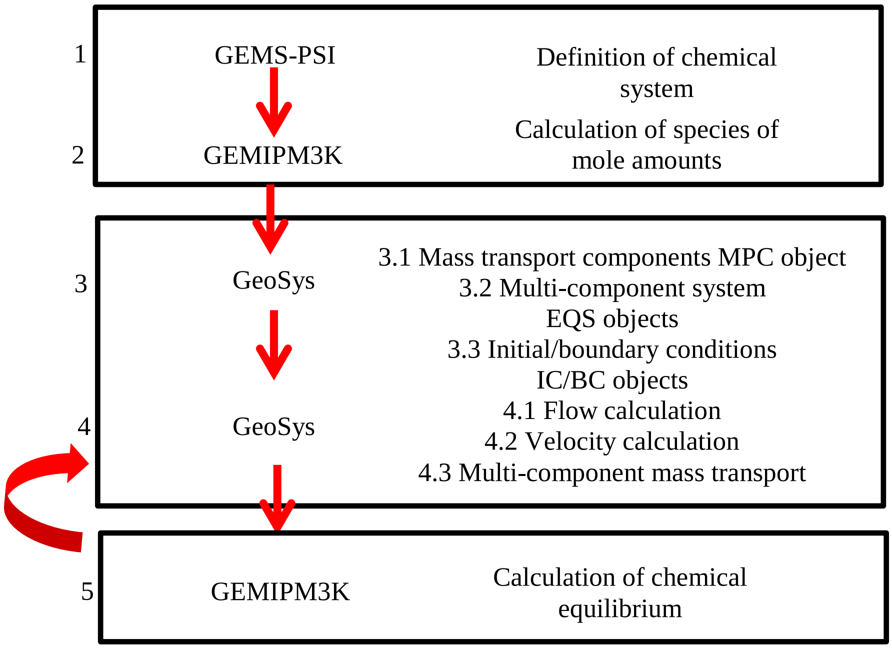

Fig. 4: Coupling structure applied for OpenGeoSys-GEM.

3.4.1. Flow and mass transport solver

In this section we summarized the main transport processes occurring in the tank. We introduce a set of mathematical equations that will be solved by the flow solver during the course of our modelling.

Although advective flow is the main transport process to be considered in our tank experiment, other processes such as diffusion become dominant in regions of low flow velocities. Such regions occur due to the in-homogeneity of the flow field in regions with low pressure gradients and in regions with lower hydraulic permeability (when pores are blocked due to mineral precipitates).

Advection: Advective solute transport is the movement of solute by a fluid due to the fluid's bulk motion. For 1D flow normal to a cross sectional area of a porous medium, the advective mass flux, F_a [mol m^{-2} s^{-1}], due to advection is given as

$$F_a = qC \qquad (2)$$

where C [mol m^{-3}] is the concentration of dissolved solutes and q [m s^{-1}] is the volumetric flux of the fluid, the so called Darcy flux, which is calculated from Darcy's equation (equation 3).

Darcy's equation (Darcy, 1856) establishes proportionality between the Darcy flux, q, and the hydraulic gradient, $\frac{dh}{dx}$:

$$q = \overline{\mathrm{K}}\frac{dh}{dx} \qquad (3)$$

The proportionality factor K [m s^{-1}] is defined as the hydraulic conductivity of the porous medium. It depends on the nature of the porous medium (porosity, shape and size of pores) and also on the fluid (viscosity and density).

For a 1 dimensional flow normal to a unit cross sectional area of the porous medium, the seepage velocity, v_i i.e. the average linear velocity is equal to the Darcy flux (q) divided by the porosity (w).

$$v_i = \frac{q}{w} \qquad (4)$$

Diffusion: Diffusive solute transport is the mass transfer of solutes due to a concentration gradient. This process is also known as molecular diffusion. The diffusive flux, F_d [mol m^{-2} s^{-1}], for a 1D system under steady state conditions is described by Fick's first law:

$$F_d = -D_e\frac{dC}{dx} \qquad (5)$$

D_e [m^2 s^{-1}] is the effective diffusion coefficient, C [mol m^{-3}] is the solute concentration and $\frac{dC}{dx}$ [mol m^{-4}] is the concentration gradient. D_e can be defined as a product of a pore diffusion coefficient D_0, the diffusion coefficient in a pore, with the porosity (w). If concentrations of solute changes with time t, Fick's second law is applied:

$$\frac{\partial wC}{\partial t} = \frac{\partial}{\partial x}\left(D_e \frac{\partial C}{\partial x}\right) \qquad (6)$$

Hydrodynamic Dispersion: The longitudinal hydrodynamic dispersion, D_L, in direction of flow of linear velocity magnitude, $|v|$, is given as:

$$D_L = \alpha_L |v| + D_e \qquad (7)$$

where α_L is the longitudinal dispersion length.

Similarly, transverse hydrodynamic, D_T, in direction of flow writes as:

$$D_T = \alpha_T |v| + D_e \qquad (8)$$

where α_T is the transverse dispersion length.

It should be noted that the dispersion term acts as an additional diffusion term in our numerical model. In field and laboratory scale tracer experiments, the dispersion length is used to fit the width of tracer breakthrough curves and is usually set to about one-tenth of the transport length. For reactive transport models, the dispersion length is usually based on the averaging unit (REV) which is the effective size of the mesh.

The total mass of solute per unit cross-sectional area transported in the x direction per unit, F_x, is the sum of the advective and dispersive transport and is given by:

$$F_x = v_x wC - wD_x \frac{\partial C}{\partial x} \qquad (9)$$

Advection-Dispersion-Diffusion-Reaction Equation

To conserve mass in the REV, the rate of mass change in the REV $w\frac{\partial C}{\partial t} dxdydz$ should be equal to the difference in the mass of solute entering and leaving the REV

$$w\frac{\partial C}{\partial t} dxdydz = \left[F_x dzdy + F_y dzdx + F_z dxdy\right] - \left[\left(F_x + \frac{\partial F_x}{\partial x} dx\right) dzdy + \left(F_y + \frac{\partial F_y}{\partial y} dy\right) dzdx + \left(F_z + \frac{\partial F_z}{\partial z} dz\right) dxdy\right] \qquad (10)$$

which simplifies to

$$-w\frac{\partial C}{\partial t} = \frac{\partial F_x}{\partial x} + \frac{\partial F_y}{\partial y} + \frac{\partial F_z}{\partial z} \qquad (11)$$

Substituting equation 9 in equation 11 gives the governing equation of a 3D mass transport for conservative solute

$$\frac{\partial C}{\partial t} = \left[\frac{\partial}{\partial x}\left(D_x \frac{\partial C}{\partial x}\right) + \frac{\partial}{\partial y}\left(D_y \frac{\partial C}{\partial y}\right) + \frac{\partial}{\partial z}\left(D_z \frac{\partial C}{\partial z}\right)\right] - \left[\frac{\partial}{\partial x}(v_x C) + \frac{\partial}{\partial y}(v_y C) + \frac{\partial}{\partial z}(v_z C)\right] \qquad (12)$$

If the Nabla operator $\nabla = \vec{e}_x \frac{\partial}{\partial x} + \vec{e}_y \frac{\partial}{\partial y} + \vec{e}_z \frac{\partial}{\partial z}$ is used to represent the partial derivatives in Cartesian coordinates, equation 12 rewrites in compact notation as:

$$\frac{\partial wC}{\partial t} = \nabla(D\nabla C) - \nabla(w\vec{v}C) \qquad (13)$$

where $\vec{v}$ is the velocity vector.

When chemical reactions are involved, the chemical sink/source of the different species involved in the reactions also needs to be included. The reactive mass transport equation is given (Bear and Bachmat, 1990) as:

$$\frac{\partial C_i}{\partial t} = \nabla(D\nabla C_i) - \nabla(\vec{v}C_i) + Q_i \qquad (14)$$

$$\frac{\partial C_i}{\partial t} = \Gamma_i(C_1 \ldots C_m),\ i = 1, 2, \ldots m \qquad (15)$$

where C_1 denotes the molar concentration of the *i*th species of a *m* multi-species system; Q_i is the source/sink term and $\Gamma_i(C_1 \ldots C_m)$is the source/sink term of species *i* due to equilibrium chemical reactions with other species.

3.4.2. Chemical solver

The geochemical modelling has been performed using the Gibbs energy minimization (GEM) approach implemented in the GEMS3K solver (http://gems.web.psi.ch/GEMS3K), based on an explicit consideration of independent components (elements e.g. Sr), dependent components (e.g. Sr^{2+}, $SrOH^-$, $SrSO_4$) and phases (solid components e.g. $SrSO_{4(s)}$) as described in detail in Kulik et al. (2013).

For a given set of indices of dependent components included into *α*-th phase, l_α, the mole amount of the *α*-th phase, is given as:

$$n_\alpha^{(\Phi)} = \sum_i n_i^{(x)},\ j \epsilon l_\alpha \qquad (16)$$

where $n_j^{(x)}$ is the mole amount of *j*-th dependent component (species).

The total Gibbs energy function of a chemical system is given as:

$$G(x) = \sum_j n_j^{(x)}\ \mu_j,\ j \epsilon L \qquad (17)$$

where μ_j is a primal approximation of a chemical potential of the *j*-th species defined via its concentration and activity coefficient, and *L* the set of indices of all dependent components.

The equilibrium speciation of the chemical system can be found by minimizing the total Gibbs energy of the system:

$$G(x) \rightarrow min \text{ subject to : } An^{(x)} = n^{(b)}, n^{(x)} \in \Re \qquad (18)$$

where $A = \{a_{ji}\}, j \in L, i \in N$; *A* is the stoichiometric matrix (a_{ji} is the number of mole of *i*-th independent component in one mole of *j*-th dependent component); $n^{(b)} = \left\{ n_i^{(b)} \right\}\ n_i^b,\ i \in N$ is an input vector of the total bulk chemical composition of the system; $n_i^{(b)}$ is the total amount of

i-th independent component in the system; and $\Re$ stands for the set of optional lower, upper or two sided kinetic (metastability) constraints to the $n_j^{(x)}$values. In this GEM setup, concentrations of dependent components are defined separately in their respective phases using $n_j^{(x)}$ and $n_\alpha^{(\Phi)}$ values. (N.B "α" used in this section refers to a phase, in other sections and in the rest of the thesis, "α" refers to the dispersion length.)

The chemical potential μ_j is formulated by the activities of dependent components. In this work, the activity coefficients for all dissolved species γ_j are calculated according to the extended Debye-Hückel equation (Helgeson et al., 1981). A detailed description is reported in Wagner et al. (2012). Equation 19 relates the activity coefficients of an aqueous ion to its charge Z_i and ionic strength I:

$$log_{10}\gamma_j = \frac{-A_\gamma Z_j^2\sqrt{I}}{1+\dot{a}B_\gamma\sqrt{I}} + b_\gamma\, I \qquad (19)$$

Where $\dot{a}$[in Å] is an average distance of approach of two ions of opposite charges, b_γ is a semi-empirical coefficient, either specific for a given electrolyte or common for all aqueous species. $\dot{a}$ and b_γ were set to 3.72 and 0.064 respectively for all the ionic species (Helgeson et al., 1981). These are values for the well calibrated sodium chloride electrolyte which will also be used for the concentrated barium chloride and strontium chloride solution. A_γ and B_γ are temperature dependent coefficients obtained internally from SUPCRT92 subroutines (Johnson et al., 1992) incorporated into the GEMS3K code. At a temperature of 25 ^{o}C and pressure of 1 bar the coefficients are $A_\gamma \approx 0.5114$ and $B_\gamma \approx 0.3288$. Activity coefficients, γ_j for neutral species (dissolved gases) and water were set to unity.

Kinetics of precipitation and dissolution reactions of minerals

The transformation from celestite to barite, and consequently also the porosity evolution, does not only depend on the transport of $BaCl_2$ and the chemical reactions, the rate of transformation is also influenced by reaction kinetics. The kinetic rates, dm/dt [mol s^{-1}] i.e. amount of mineral dissolving/precipitating per unit time, are calculated following Palandri and Kharaka (2004).

In our simulations, barite was assumed to precipitate instantaneously (very fast kinetics) and only the dissolution kinetics of celestite was taken into account. The dissolution rate of celestite at pH = 5.6 (pH of the experiment) is calculated based on the equation given in Palandri and Kharaka (2004) with parameters from Dove and Czank (1995).

$$\frac{dm}{dt} = -\mathrm{SA}\, k^{\circ}(1-\Omega) \qquad (20)$$

where SA [m^2] is the reactive surface area of the celestite mineral phase, $k^{\circ} = 10^{-5.66}$ mol m^{-2} s^{-1} is the dissolution rate constant at 298.15 K and Ω is the ratio of ion activity product of the mineral to the equilibrium constant.

In our simulations, a very simple reactive surface area SA [m^2] model was chosen

$$\mathrm{SA} = Va \qquad (21)$$

where V [m^3] is the volume of the mineral and a [$m^2\ m_{mineral}^{-3}$] is a mineral's specific surface area (i.e., surface area per volume of the mineral phase). The reactive surface area for each mineral phase is calculated using equation 21.

4. Outline of the thesis

In **chapter 2**, we give a description of our experimental setup and the numerous experiments carried out to test different couplings implemented in OpenGeoSys-GEM such as conservative mass transport, density driven flow and finally transport with a chemical reaction. Our experimental observations and preliminary post mortem analysis showed that clogging occurred in the system. Tests with non-reactive tracers performed prior to barium chloride injection as well as the density-driven flow were well reproduced by the numerical model. For the reactive transport experiment, chemical and structural changes occurring at the pore scale and interface had to be considered in the continuum scale approach to successfully reproduce mineral bulk transformation with time and measured pressure increased during the course of the experiment.

This chapter is published as "Poonoosamy, J., Kosakowski, G., Van Loon, L. R., Mäder, U., 2015. Dissolution-Precipitation Processes in Tank Experiments for Testing Numerical Models for Reactive Transport Calculations: Experiments and Modelling. Journal of Contaminant Hydrology, 177-178, 2015, 1-17."

In **chapter 3**, we concentrate on the refinement of post mortem analysis combining scanning electron microscopy and synchrotron X-ray microdiffraction/microfluorescence. Our aim was to understand the precipitation of barite in the pore space. Two distinct nucleation mechanisms for barite precipitation are pointed out: homogeneous nucleation (nucleation of barite in the pore space) and heterogeneous nucleation (nucleation on the surface of a solid substrate). Classical nucleation theory, using well-established and estimated parameters describing barite precipitation, was applied to explain the mineralogical changes occurring in our system.

This chapter is a manuscript submitted as "Poonoosamy, J., Curti E., Kosakowski, G., Grolimund, D., Van Loon, L. R., Mäder, U. Barite precipitation following celestite dissolution in a porous medium: a SEM/BSE and µ-XRD/XRF study" to Geochimica et Cosmochimica Acta" and has already been reviewed. The most important reviewers' remarks were implemented.

In **chapter 4** we present three numerical benchmark cases which are based on the experimental work. We considered three case studies with increasing complexity: case 1 considers a 2D system with density driven flow and conservative mass transport, case 2 in addition includes the dissolution and precipitation of mineral phases leading to porosity changes and case 3 extends the case 2 by considering the formation of solid solutions.

This chapter is presented in a book that will be published beginning of 2016 as He, W., Poonoosamy, J., Kosakowski, G., Van Loon, L.R., Mäder, U., 2016, Chapter 12, Reactive Transport, in: Kolditz O., Görke U.J., Wang W., Shao H., Bauer S. (eds), Thermo-Hydro-Mechanical-Chemical Processes in Fractured Porous Media: Modelling and Benchmarking-Benchmarking Initiatives, Springer International Publishing AG, Cham.

Chapter 5: We proposed a reactive transport benchmark based on our experiments with 4 levels of complexity within the SeS bench initiative. The processes included are advective-diffusive transport of solutes, effect of liquid phase density on liquid flow and advective transport, kinetically controlled dissolution/precipitation reactions causing porosity, permeability and diffusivity changes, and the formation of pure mineral phases vs. the formation of a solid solution. In this paper, we present and analyse the results of an inter-comparison of 4 reactive transport codes (i.e. TOUGHREACT, Pflotran, CORE2D and OpenGeoSys-GEM). The considered cases differ partly from the cases presented in chapter 4, due to the capabilities of the codes, and some process couplings (e.g. density driven flow) could not be considered in all benchmark cases.

This chapter is a manuscript that is currently in preparation as “Poonoosamy, J., Kosakowski, G., Wanner, C., Alt Epping, P, Águila, J. F., Samper, J., Mäder, U., Van Loon, L. R., Dissolution precipitation reactions in a 2D setup for testing concepts of reactive transport codes” for submission to Computer Geosciences.

Chapter 6: In this chapter, we summarize our experimental and modelling work. We also present additional information that was not included in the publications. We discuss and evaluate topics that were not covered by this thesis such as upscaling of kinetics and pore scale simulation that could be done.

Please note that the notations of the equation might be different in the 5 chapters but consistent within the chapter. The notations for unpublished chapters or work not yet submitted (chapters 1, 5 and 6) were kept the same. Also note that references for chapter 3 conform to the criteria of Geochimica et Cosmochimica Acta are different from the rest of the chapters.

References

Archie, G., 1942. The electrical resistivity log as an aid in determining some reservoir characteristics. Trans. AIME, 146, 54-62.

Alt-Epping, P., Diamond, L.W., Häring, M.O., Ladner, F., Meier, D.B., 2013a. Prediction of water-rock interaction and porosity evolution in a granitoid - hosted enhanced geothermal system, using constraints from the 5 km Basel-1 well. Appl. Geochem., 38, 121-133.

Alt-Epping, P., Waber, H.N., Diamond, L.W., Eichinger, L., 2013b. Reactive transport modeling of the geothermal system at Bad Blumau, Austria: Implications of the combined extraction of heat and CO_2. Geothermics, 45, 18-30.

Bear, J., 1972. Dynamics of Fluids in Porous Media. Dover Publications, Inc., New York.

Bear, J., Bachmat, Y., 1990. Introduction to modelling of transport phenomena in porous media. Springer, Berlin.

Boving, T.B., Grathwohl, P., 2001. Tracer diffusion coefficients in sedimentary rocks: correlation to porosity and hydraulic conductivity. J. Contam. Hydrol., 53(1-2), 85-100.

Berner, U., Kulik, D.A., Kosakowski, G., 2013. Geochemical impact of a low-pH cement liner on the near field of a repository for spent fuel and high-Level radioactive waste. Phys. Chem. Earth, 64, 46-56.

Bildstein, O., Kervévan, C., Lagneau, V., Delaplace, P., Crédoz A., Audigane, P., Perfetti, E., Jacquemet, N., Jullien, M., 2010. Integrative modeling of caprock integrity in the context of CO_2 storage: Evolution of transport and geochemical properties and impact on performance and safety assessment. Oil Gas Sci. Technol. IFP, 65(3), 485-502.

Cailly, B., Le Thiez, P., Egermann, P, Audibert, A., Vidal-Gilbert S., Longaygue, X., 2005. Geological storage of CO_2: A state-of-the-art of injection processes and technologies. Oil Gas Sci. Technol. IFP, 60(3), 517-525.

Campbell, J.R., Nancollas, G.H, 1969, The crystallization and dissolution of strontium sulfate in aqueous solution. J. Phys. Chem., 73(6), 1735-1740.

Carman, P.C., 1937. Fluid through granular beds. Trans. Inst. Chem. Eng., 15, 150-166.

Carrayou, J., Hoffmann, J., Knabner, P., Kräutle, S., De Dieuleveult, C., Erhel, J., van der Lee, J., Lagneau, V., Mayer, K.U., MacQuarrie, K.T.B., 2010. Comparison of numerical methods for simulating strongly nonlinear and heterogeneous reactive transport problems - the MoMas benchmark case. Computat. Geosci., 14(3), 483-502.

Class, H., Ebigbo, A., Helmig, R., Dahle, H.K., Nordbotten, J.M., Celia, M.A., Aubigane, P., Darcis, M., Ennis-King, J., Fan, Y., Flemisch, B., Gasda, S.E., Jin, M., Krug, S., Labregere, D., Beni, A.N., Pawar, R.J., Sbai, A., Thomas, S.G., Trenty, L., Wei, L., 2009. A benchmark study problems related to CO_2 storage in geologic formations. Computat. Geosci., 13(4), 409-432.

Cochepin, B., Trotignon, L., Bildstein, O., Steefel, C.I., Lagneau, V., van der Lee, J., 2008. Approaches to modelling coupled flow and reaction in a 2D cementation experiment. Adv. Water Resour., 31(12), 1540-1551.

Darcy, H.P.G. (1856) Détermination des lois d'écoulement de l'eau à travers le sable. Les fontaines publiques de la Ville de Dijon, Victor Dalmont, Paris.

Dauzeres, A., Le Bescop, P., Sardini, P., Cau Dit Coumes, C., 2010. Physicochemical investigation of clayey/cement-based materials interaction in the context of geological waste disposal: experimental approach and results. Cem. Concr. Res., 40(8), 1327-1340.

De Windt, L., Pellegrini, D., van der Lee, J., 2004. Coupled modeling of cement/claystone interactions and radionuclide migration. J. Contam. Hydrol., 68(3-4), 165-182.

De Windt, L., Badredinne, R., Lagneau, V., 2007. Long-term reactive transport modelling of stabilized/solidified waste: from dynamic leaching tests to disposal scenarios. J. Hazard. Mater., 139(3), 529-536.

Diamond, L.W., Alt-Epping, P., 2014. Predictive modelling of mineral scaling, corrosion and the performance of solute geothermometers in a granitoid-hosted, enhanced geothermal system. Appl. Geochem., 51, 216-228.

Dove, P.M., Czank, C.A., 1995. Crystal chemical controls on the dissolution kinetics of the isostructural sulfates: Celestite, anglesite, and barite. Geochim. Cosmochim. Acta, 56(10), 4147-4156.

Gaboreau, S., Lerouge, C., Dewonck, S., Linard, Y., Bourbon, X., Fialips, C.I., Mazurier, A., Prêt, D., Borschneck, D., Montouillout, V., Gaucher, E. C., Claret, F., 2012. In-situ interaction of cement paste and shotcrete with claystones in a deep disposal context. Am. J. Sci., 312(3), 314-356.

Gaucher, E.C., Blanc, P., 2006. Cement/clay interaction - a review: Experiments, natural analogues, and modelling. Waste Manage., 26(7), 776-788.

Hayek, M., Kosakowski, G., Churakov, S., 2011. Exact analytical solutions for a diffusion problem coupled with a precipitation-dissolution reaction and feedback of porosity change. Water Resour. Res., 47,W07545.

Hayek, M., Kosakowski, G., Jakob, A., Churakov, S.V., 2012. A class of analytical solutions for multidimensional multispecies diffusive transport coupled with precipitation-dissolution reactions and porosity changes. Water Resour. Res., 48, W03525.

Helgeson, H.C., Kirkham, D.H., Flowers, G.C., 1981. Theoretical prediction of the thermodynamic behavior of aqueous electrolytes at high pressures and temperatures: IV. Calculation of activity coefficients, osmotic coefficients, and apparent molal and standard and relative partial molal properties to 600°C and 5 KB. Am. J. Sci., 281, 1249-1516.

Jamieson-Hanes, J.H., Amos, R.T., Blowes, D.W., 2012. Reactive transport modeling of Chromium Isotope Fractionation during Cr(IV) Reduction. Environ. Sci. Technol., 46(24), 13311-13316.

Johnson, J.W., Oelkers, E.H., Helgeson, H.C., 1992. SUPCRT92: A software package for calculating the standard molal thermodynamic properties of minerals, gases, aqueous species, and reactions from 1 to 5000 bar and 0 to 1000 °C. Computat. Geosci., 18(7), 899-947.

Jenni, A., Mäder, U., Lerouge, C., Gaboreau, S., Schwyn, B., 2014. In situ interaction between different concretes and Opalinus Clay. Phys. Chem. Earth, A/B/C 70-71, 71-83.

Katz, G.E., Berkowitz, B., Guadagnini, A., Saaltink M.W., 2011. Experimental and modeling investigation of multicomponent reactive transport in porous media. J. Contam. Hydrol., 120-121, 27-44.

Kosakowski, G., Berner, U., 2013. The evolution of clay rock/cement interfaces in a cementitious repository for low and intermediate level radioactive waste. Phys. Chem. Earth, A/B/C, 64, 65-86.

Kosakowski, G., Watanabe, N., 2014. OpenGeoSys-Gem: A numerical tool for calculating geochemical and porosity changes in saturated and partially saturated media. Phys. Chem. Earth, A/B/C, 70-71, 138-149.

Kulik, D.A., Wagner, T., Dmytrieva, S.V., Kosakowski, G., Hingerl, F.F., Chudnenko, K.V., Berner, U., 2013. GEM-Selektor geochemical modeling package: revised algorithm and GEMS3K numerical kernel for coupled simulation codes. Comput. Geosci, 17(1), 1-24.

Lagneau, V., 2000. Influence des processus géochimiques sur le transport en milieu poreux; application au colmatage de barrières de confinement potentielles dans un stockage en formation géologique. PhD Thesis, Ecole des Mines de Paris.

Lagneau, V., van der Lee, J., 2010a. Operator-splitting-based reactive transport models in strong feedback of porosity change: The contribution of analytical solutions for accuracy validation and estimator improvement. J. Contam. Hydrol., 112(1-4), 118-129.

Lagneau, V. van der Lee, J., 2010b. HYTEC results of the MoMas reactive transport benchmark. Computat. Geosci. 14(3), 435-449.

Larson, A., 1992. The International Projects INTRACOIN, HYDRAOCOIN, and INTRAVAL. Adv. Water Resour., 15, 85-87.

Liu, J., Pereira, G.G., Regenauer-Lieb, K., 2014. From characterisation of pore-structures to simulations of pore-scale fluid flow and the upscaling of permeability using microtomography: a case study of heterogeneous carbonates. J. Geochem. Explor., A, 144, 84-96.

Liu, S.T., Nancollas, G.H., Gasiecki, E.A 1976. Scanning electron microscopic and kinetic studies of the crystallization and dissolution of barium sulfate crystals. J. Cryst. Growth, 33(1), 11-20.

Mackenzie, P.D., Horney, D.P., Sivavec, T.M., 1999. Mineral precipitation and porosity losses in granular iron columns. J. Hazard. Mater., 68(1-2), 1-17.

Marica, F., Jofré, S.A.B, Mayer, K.U., Balcom, B.J., Al, T.A., 2011. Determination of spatially-resolved porosity, tracer distributions and diffusion coefficients in porous media using MRI measurements and numerical simulations. J. Contam. Hydrol., 125(1-4), 47-56.

Molin, S., Trebotich, D., Steefel, C. I., Shen, C., 2012. An investigation of the effect of pore scale flow on average geochemical reaction rates using direct numerical simulation, Water Resour. Res., 48, W03527.

Palandri, J.L., Kharaka, Y.K., 2004. A compilation of rate parameters of water mineral interaction kinetics for application to geochemical modelling. U.S. Geological Survey, Menlo Park, California.

Perko, J., Mayer U.K., Kosakowski, G., De Windt, L., Govaerts, J.,·Jacques, D.,·Danyang, S., Meeussen, J.C.L., 2015. Decalcification of cracked cement structures. Computat. Geosci., 19(3), 673-693.

Prieto, M., Putnis, A., Fernández-Díaz, L., 1990. Factors controlling the kinetics of crystallization: supersaturation evolution in porous medium. Application to barite crystallization. Geol. Mag., 127(6), 485-495.

Prieto, M., Putnis, A. Fernández-Díaz, L. 1993. Crystallization of solid solutions from aqueous solutions in a porous medium: zoning in (Ba, Sr)SO_4. Geol. Mag., 130(3), 289-299.

Prieto, M., Fernández-González, A., Putnis, A., Fernández-Díaz, L. 1997. Nucleation, growth and zoning phenomena in crystallization (Ba, Sr)CO_3, Ba(SO_4, CrO_4), (Ba, Sr)SO_4 and (Cd, Ca)CO_3 solid solutions from aqeous solutions. Geochim. Cosmochim. Acta, 61(16), 3383-3397.

Putnis, A., Prieto, M. Fernández-Díaz, L., 1995. Fluid supersaturation and crystallization in porous media. Geol. Mag., 132(1), 1-13.

Refsgaard, J.C., Henriksen, H.J., 2004. Modelling guidelines-terminology and guiding principles. Adv. Water Resour., 27(1), 71-82.

Sánchez-Pastor, N., Pina, C.M., Astilleros, J.M., Fernández-Díaz, L., Putnis, A., 2005. Epitaxial growth of celestite on barite (001) face at a molecular scale. Surf. Sci., 581(2-3), 225-235.

Sánchez-Pastor, N., Pina, C.M., Fernández-Díaz, L., 2006. Relationship between crystal morphology and composition in the (Ba,Sr)SO_4-H_2O solid solution - aqueous system. Chem. Geol., 225(3-4), 266-277.

Samper, J., Xu, T., Yang, C., 2009. A sequential partly iterative approach for multicomponent reactive transport with CORE2D. Computat. Geosci., 13, 301-316.

Saripalli, K.P., Meyer P. D., Bacon, D.H., Feedman, V. L., 2001. Changes in hydrologic properties of aquifer media due chemical reaction: review. Crit. Rev. Env. Sci. Technol., 31(4), 311-349.

Seifert, D., Engesgaard, P., 2012. Sand box experiments with bioclogging of porous media: hydraulic conductivity reductions. J. Contam. Hydrol., 136-137, 1-9.

Scheibe, T.D., Schuchardt, K., Agarwal, K, Chase, J., Yang, X., Palmer, B.J., Tartakovsky, A.M, Elsethagen, T., Redden, G., 2015. Hybrid multiscale simulation of a mixing-controlled reaction. Adv. Water Resour., 83, 228-239.

Shao, H., Dmytrieva, S.V., Kolditz, O., Kulik, D.A., Pfingsten, W., Kosakowski, G., 2009. Modeling reactive transport in non-ideal aqueous-solid solution system. Appl. Geochem., 24(7), 1287-1300.

Steefel, C.I., De Paolo, D.J., Lichtner, P.C., 2005. Reactive transport modeling: an essential tool and a new research approach for earth sciences. Earth Planet. Sci. Lett., 240(3-4), 539-558.

Steefel, C.I., Appelo, C.A.J., Arora, B., Jacques, D., Kalbacher, T., Kolditz, O., Lagneau, V., Lichtner, P.C., Mayer, K.U., Meeussen, J.C.L., Molins, S., Moulton, D., Shao, H., Šimůnek, J., Spycher, N.F., Yabusaki, S.B., Yeh, G.T., 2015. Reactive transport codes for subsurface environmental simulation. Computat. Geosci., 19(3), 445-478.

Tartakovsky, A.M., Redden, G., Lichtner, P.C., Scheibe, T.D., Meakin, P., 2008. Mixing-induced precipitation: experimental study and multiscale numerical analysis. Water Resour. Res., 44, W06S04.

Thullner, M., Mauclaire, L., Schroth, M.H., Kinzelbach, W., Zeyer, J., 2002. Interaction between water flow and spatial distribution of microbial growth in a two-dimensional flow field in saturated porous media. J. Contam. Hydrol., 58(3-4), 169-189.

Tsang, C. F., Jing, L., Stephansson, O., Kautsky, F., 2005. The DECOVALEX III project: a summary of activities and lessons learned. Int. J. Rock Mech. Min. Sci., 42(5-6), 593-610.

Tyagi, M., Gimmi, T., Churakov, S.V., 2013. Multi-scale micro-structure generation strategy for upscaling transport in clays. Adv.Water Resour. 59, 181-195.

van der Lee, J., De windt, L., Lagneau V., Goblet, P., 2003. Module oriented modeling of reactive transport with HYTEC. Comput. Geosci., 29(3), 265-275.

Van Loon, L.R., Glaus, M.A., Müller, W., 2007. Anion exclusion effects in compacted bentonites: towards a better understanding of anion diffusion. Appl. Geochem. 22(11), 2536-2552.

Wagner, T., Kulik, D.A., Hingerl, F.F., Dmytrieva, S.V., 2012. GEM-Selektor geochemical modeling package: TSolMod C++ class library and data interface for multicomponent phase models. Can. Mineral., 50, 1173-1195.

Wanner, C., Eggenberger, U., Mäder, U., 2012. A chromate-contaminated site in southern Switzerland –part 2: Reactive transport modeling to optimize remediation options. Appl. Geochem., 27(3), 655-662.

Wanner, C., Sonnenthal, E.L., 2013. Assessing the control on the effective kinetic Cr isotope fractionation factor: A reactive transport modeling approach. Chem. Geol., 337-338, 88-98.

Wanner, C., Peiffer, L., Sonnenthal, E.L., Spycher, N., Iovenitti, J., Kennedy, B.M., 2014. Reactive transport modeling of the Dixie Valley geothermal area: Insights on flow and geothermometry. Geothermics, 51, 130-141.

Xie, M., Mayer, K.U., Claret, F., Alt-Epping, P., Jacques, D., Steefel, C., Chiaberge, C., Šimůnek, J., 2015. Implementation and evaluation of permeability-porosity and tortuosity-porosity relationships linked to mineral dissolution-precipitation. Computat. Geosci., 19(3), 655-671.

Chapter 2: Dissolution-precipitation processes in tank experiments for testing numerical models for reactive transport calculations: Experiments and modelling

Journal of Contaminant Hydrology 177–178 (2015) 1–17

Contents lists available at ScienceDirect

Journal of Contaminant Hydrology

journal homepage: www.elsevier.com/locate/jconhyd

Dissolution–precipitation processes in tank experiments for testing numerical models for reactive transport calculations: Experiments and modelling

Jenna Poonoosamy [a,*], Georg Kosakowski [a], Luc R. Van Loon [a], Urs Mäder [b]

[a] *Laboratory for Waste Management, Paul Scherrer Institut, CH-5232 Villigen PSI, Switzerland*
[b] *Rock Water Interaction, Institute of Geological Sciences, University of Bern, Baltzerstrasse 3, CH-3012 Bern, Switzerland*

ARTICLE INFO

Article history:
Received 17 November 2014
Received in revised form 19 February 2015
Accepted 25 February 2015
Available online 14 March 2015

Keywords:
Porosity clogging
Reactive transport
Dissolution/precipitation experiments
Experimental benchmarks

ABSTRACT

In the context of testing reactive transport codes and their underlying conceptual models, a simple 2D reactive transport experiment was developed. The aim was to use simple chemistry and design a reproducible and fast to conduct experiment, which is flexible enough to include several process couplings: advective–diffusive transport of solutes, effect of liquid phase density on advective transport, and kinetically controlled dissolution/precipitation reactions causing porosity changes. A small tank was filled with a reactive layer of strontium sulfate ($SrSO_4$) of two different grain sizes, sandwiched between two layers of essentially non-reacting quartz sand (SiO_2). A highly concentrated solution of barium chloride was injected to create an asymmetric flow field. Once the barium chloride reached the reactive layer, it forced the transformation of strontium sulfate into barium sulfate ($BaSO_4$). Due to the higher molar volume of barium sulfate, its precipitation caused a decrease of porosity and lowered the permeability. Changes in the flow field were observed with help of dye tracer tests. The experiments were modelled using the reactive transport code OpenGeosys-GEM. Tests with non-reactive tracers performed prior to barium chloride injection, as well as the density-driven flow (due to the high concentration of barium chloride solution), could be well reproduced by the numerical model. To reproduce the mineral bulk transformation with time, two populations of strontium sulfate grains with different kinetic rates of dissolution were applied. However, a default porosity permeability relationship was unable to account for measured pressure changes. Post mortem analysis of the strontium sulfate reactive medium provided useful information on the chemical and structural changes occurring at the pore scale at the interface that were considered in our model to reproduce the pressure evolution with time.

1. Introduction

The changes of the porosity in a porous medium due to mineral alteration processes, and the associated change of transport parameters, are important processes which influence the evolution of natural geological environments or engineered underground (disposal) systems. Such material changes are of major interest in many geo-scientific disciplines and specifically in (ground) water science.

Porosity changes in a porous medium are typically caused by the complex interactions between physical and (bio) chemical processes. During bioremediation, clogging of porous media due to mineral precipitation, and gas production by microbial activity, can lead to a reduction of the effective porosity and hydraulic conductivity (Seifert and Engesgaard, 2012; Thullner et al., 2002). This decreases the efficiency of bioremediation of the polluted groundwater. During injection of CO_2 into geological formations, the CO_2 mixes with ground

---

[*] Corresponding author. Tel.: +41 563 10 2079.
E-mail address: jenna.poonoosamy@psi.ch (J. Poonoosamy).

http://dx.doi.org/10.1016/j.jconhyd.2015.02.007
0169-7722/© 2015 Elsevier B.V. All rights reserved.

waters (or brines) and interacts with rock minerals. It is expected that the binding of CO_2 in newly formed mineral phases causes significant changes in porosity and permeability (Xu et al., 2005). Porosity changes due to mineral precipitation/dissolution are also being actively investigated in connection with the deep geological disposal of nuclear waste where chemically very different materials such as clays and concretes come into contact with one another (Gaucher and Blanc, 2006). The mixing of pore waters from cement based materials with waters from the surrounding clay host rock will lead to the dissolution and precipitation of mineral phases at the clay–cement interface and might result in pore clogging after long times (Dauzeres et al., 2010; Gaboreau et al., 2012; Jenni et al., 2014).

Very often, reactive transport codes are used to predict the evolution of systems that are not experimentally accessible in space and time, for example the behaviour of CO_2 in saline aquifers (Chasset et al., 2011; Lagneau et al., 2005) and the mineral transformations and associated porosity changes at clay/concrete interfaces (De Windt et al., 2004, 2007; Gaucher and Blanc, 2006; Kosakowski and Berner, 2013).

The numerical models used to calculate these systems are typically based on a continuum approach utilising a representative elementary volume (REV) (Kanit et al., 2003; Lichtner, 1992). The REV concept assumes that chemical compositions, as well as material and transport parameters, can be homogenised on the scale of the spatial discretization. To properly resolve steep concentration gradients at the continuum scale it is often necessary to choose a spatial discretization which is smaller than the REV. In reality, chemical reactions and associated changes of pore space geometry due to the precipitation or dissolution of mineral grains take place at the micro (pore)-scale. The simulated results for porosity change using a continuum approach depend on the assumed rate laws for reaction kinetics and on the applied numerical mesh refinement (Marty et al., 2009). This effect is related to the kinetic control of chemical reactions. When using a chemical equilibrium approach (instantaneous equilibration in a REV) in continuum based reactive transport models with strong porosity changes, grid convergence cannot be achieved (Hayek et al., 2011, 2012). For kinetic control of dissolution/precipitation reactions, grid convergence can be reached, although this might result in grid volumes that are well below the REV.

Porosity changes due to precipitation/dissolution reactions, and their feedback on transport properties, are accounted in numerical models by considering empirical formulae: Kozeny–Carman for porosity/permeability (Carman, 1937), and Archie's law for porosity/diffusivity (Archie, 1942). These empirical laws need to be parameterised, either experimentally (e.g., Boving and Grathwohl, 2001; Van Loon et al., 2007; Marica et al., 2011), or by up-scaling from micro-scale models (e.g., Liu et al., 2014; Tyagi et al., 2013).

Several numerical codes are able to handle the feedback of chemistry on flow and mass transport. However, only a few laboratory experiments have been carried out to test the validity of existing and new concepts for reactive numerical models which couple chemical and transport processes via strong porosity changes. Such experiments involve clogging experiments due to mixing induced precipitation in simple media in 2D set ups or primary mineral dissolution followed by secondary mineral precipitation in 1D set ups.

Emmanuel and Berkowitz (2005) conducted numerical experiments to explore the effect of mineral precipitation and porosity reduction induced by mixing of fluids of different compositions. The calculations showed that porosity was reduced primarily in those regions in which significant changes in mixing occurred. The authors emphasised that surface area, expressed as function of porosity, had a strong influence on the predicted porosity patterns by influencing both the kinetics of precipitation and the permeability of the porous media.

The experiments conducted by Tartakowsky et al. (2008) involved the injection of two reacting solutions into cells filled with quartz grains from opposite inlets. They observed the formation of a narrow calcite precipitate with a uniform width of less than 5 mm in the middle of the cell. The pore scale modelling of the system revealed large pore scale concentration gradients. Continuum (Darcy) simulations based on the commonly used advection–dispersion equation (ADE) showed that only a model with grid sizes in the mixing zone smaller than the size of the quartz grains could reproduce the main features of the experiment. As an alternative to high resolution simulation, the ADE was modified to include transport and mixing indices in the reaction terms. These parameters account for highly non-uniform pore scale concentration gradients and localised precipitation at the sub-grid scale.

Katz et al. (2011) proposed an experiment similar to that of Tartakowsky et al. (2008). The authors triggered the precipitation of calcite in homogeneous and heterogeneous media by the injection of sodium bicarbonate and calcium chloride (matched to the same density) through parallel inlets into the flow cell. They successfully reproduced the conservative transport of solutes with an ADE based model, but the ADE based reactive transport model failed to reproduce porosity clogging and measured concentrations at the sampling ports. These results — in agreement with those from Tartakowsky et al. (2008) — suggested the inappropriateness of using the ADE in the continuum models to predict pore scale reactions.

Lagneau (2000) conducted two series of column experiments in advective and diffusive transport regimes to investigate the feedback of porosity changes on transport parameters. In both sets of experiments, porosity change was forced by the injection of a reactive solution which triggered the replacement of a primary mineral phase by a secondary mineral phase with different molar volumes. These experiments were used to validate the feedback between chemistry and transport in the reactive transport code Hytec.

Based on the work of Lagneau (2000), Trotignon et al. (2005) proposed a numerical benchmark which involved the replacement of a primary mineral phase (portlandite) by a secondary mineral phase with a larger molar volume (calcium oxalate) that could lead to porosity clogging. The reactive layer of portlandite was sandwiched between two layers of sand assumed to be unreactive during the simulation. An asymmetric injection of a reactive fluid caused a spatially heterogeneous porosity change with subsequent changes to the flow field. Cochepin et al. (2008) made a comparative study of this numerical benchmark using Crunch (Steefel et al., 2005) and Hytec (Van der Lee, 2003). The results given by the two codes were in fairly good agreement. Differences were explained by the different models for reactive surface area used to describe dissolution and precipitation of mineral phases. These models were never verified experimentally. Such an experiment is difficult to conduct in practice because the highly alkaline leaching solution from portlandite will dissolve the sand.

There is a lack of carefully designed porosity clogging experiments in a 2D heterogeneous transport setup in which the dissolution of a primary mineral phase is followed by the precipitation of a secondary mineral phase. Therefore, based on the design of Trotignon et al. (2005) and Cochepin et al. (2008), we performed a revised 2D reactive transport experiment in which a porosity change was caused by the replacement of strontium sulfate by barium sulfate. The experimental analysis included the micro-scale investigation of porosity changes which is indispensable for gaining insight into the nature and spatial distribution of the newly formed phases and their effect on porosity reduction.

In this paper we will thus present the experiments, compare them to the numerical simulations and describe how we considered micro-scale changes in continuum scale models.

2. Materials and methods

2.1. Experimental setup

The experiments were conducted in a Plexiglas tank. The tank and the setup of the packing are illustrated in Fig. 1. The inner dimensions of the tank were 0.1 m × 0.1 m × 0.01 m in the x, z and y directions respectively. The tank had several outlets along its boundaries and at the back. During the experiment, 4 ports (a, b, c, d) at the back of the tank were used. Tubes with inner and outer diameters of 0.5 mm and 1.5 mm, respectively, were inserted through the ports at the back of the tank and fixed with silicon glue to the front face of the tank. The tube sections in the tank were perforated to allow tracer injection, fluid sampling and pressure measurements. Two tubes (a and b) were connected to pressure sensors (PX26-001DV from Omega Engineering Inc.) which allowed pressure differences from 0 mbar (0 Pa or 0 mm hydraulic head) to 70 mbar (700 Pa or 71 mm hydraulic head) to be measured. The outlet ports (c and d) were used for sampling.

The granular porous medium used in the experiment was commercial silicon dioxide (quartz sand) with a purity of 99.9% (with iron contamination) having a grain size of 0.1–0.3 mm with a coefficient of variation of 0.96 (Sigma Aldrich). We tried to homogenise the sand packing as much as possible while filling the tank. The porosity, *w*, of the Q1 and Q3 regions was calculated to be 0.34 ± 0.02 and 0.40 ± 0.02 respectively using the following formula:

$$w = 1 - \frac{\rho_{bulk}}{\rho_{grain}} \tag{1}$$

where ρ_{grain} [kg m^{-3}] and ρ_{bulk} [kg m^{-3}] are the grain and bulk densities of the solid respectively. The difference in porosity is due to a different compaction in the two regions which we were not able to avoid without disturbing the geometry of the reactive layer. The hydraulic conductivity of quartz sand packed to a porosity of 0.35 was measured to be (1.8 ± 0.2) × 10^{-11} m^2 in separate 1D experiments using a falling head test (Kresic, 2006). The permeability of a porous medium is influenced by the size of pores and their interconnectivity which is influenced by the shape and arrangement of grains.

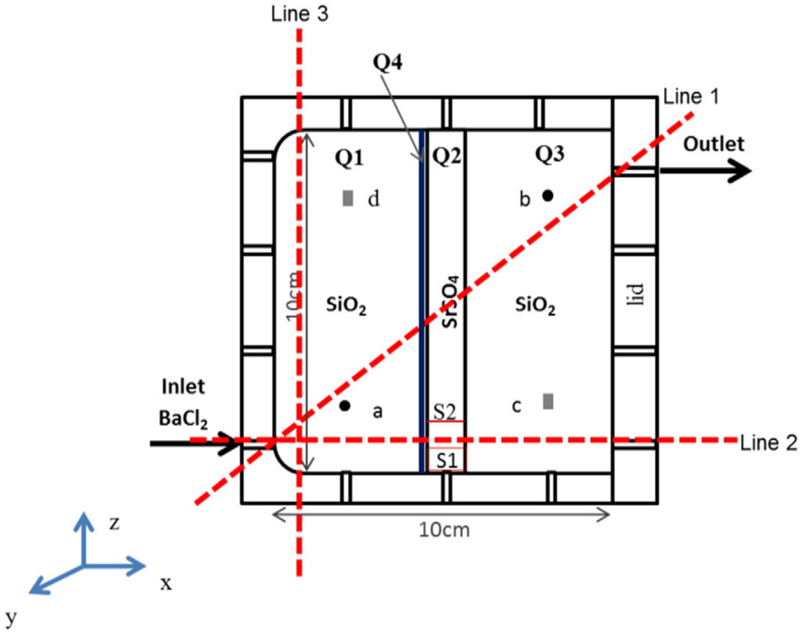

Fig. 1. Sketch of the experimental setup (modified model proposed by Cochepin et al., 2008). The 10 cm square tank has a strontium sulfate ($SrSO_4$) region Q2 sandwiched between two regions of quartz grains, Q1 and Q3. "a" and "b" are ports to which pressure sensors are connected, "c" and "d" are sampling ports with the respective coordinates (x; z) in mm (20.65; 20.35), (80.65; 77.85), (80.65; 20.35) (20.65; 77.85). The line labelled 1 that connects the inlet (0.00; 9.65) to the outlet (100.00; 90.20), line labelled 2 (z = 1 cm), line labelled 3 (x = 1 cm) are test lines on which simulated and experimental velocity profiles will be compared. The inlet and outlet have a diameter of 3.3 mm. S1 and S2 are samples of the reactive medium analysed by X-ray diffraction and X-ray fluorescence respectively. Q4 is a 1 mm wide interface region between Q1 and Q2 used to describe a zone with strong porosity reduction in some experiments.

The larger the pore space, the more permeable is the porous medium. The measured permeability is in good agreement with the permeability calculated by the Kozeny–Carman equation applied to spherical grains (Bear, 1972; Carman, 1937) given below:

$$k = \left[\frac{w^3}{(1-w)^2}\right]\frac{d_m^2}{180} \tag{2}$$

where k [m^2] is the permeability, d_m [m] is the representative particle diameter of the mixture (in our calculation $d = 0.1$ mm and $d = 0.3$ mm were tested), ρ [kg m^{-3}] is the fluid density, g [m^2 s^{-1}] is the gravitational acceleration, and μ is the dynamic viscosity [Pa s]

The strontium sulfate used in our experiment was a natural strontium sulfate from Madagascar consisting of tumble polished stones with very low porosity. The stones were washed with ethanol, crushed and sieved giving batches of different grain sizes. Unlike sand grains, strontium sulfate grains are not spherical, but more brick-shaped due to the orthorhombic crystal symmetry of the strontium sulfate. The natural strontium sulfate was analysed by X-ray diffraction which revealed a purity of 99.7% and 0.3% of anhydrous calcium sulfate. In order to further decrease the initial porosity of the reactive medium, particles of different grain sizes were mixed: ~ 30 wt.% with a size less than 63 μm and ~70 wt.% with a size of 125–400 μm. The strontium sulfate was compacted to a porosity of 0.32 ± 0.02. The Brunauer–Emmett–Teller (BET) surface area of the large and small strontium sulfate grains were 0.523 and 0.927 m^2 g^{-1}, respectively. The permeability of strontium sulfate with the same granulometry as in the tanks experiments and compacted to the same porosity was measured to be between 1×10^{-14} m^2 and 6×10^{-14} m^2 using a falling head method in separate experiments. The range of values for the permeability of strontium sulfate is sensitive to the arrangement of the strontium sulfate grains during the filling. The strontium sulfate layer is three orders of magnitude less permeable than the sand layer, both having however quite similar porosities. According to section 8.4 in Rock Physics Handbook (Mavko et al., 2006), it is often possible for mixed particle sizes to use the Kozeny–Carman equation with an effective or averaged particle size d_m according to the harmonic mean

$$d_m = \sum\nolimits_i \frac{f_i}{d_i} \tag{3}$$

where f_i is the mass or volume fraction of the corresponding particle population i with diameter d_i, and all particles have the same mineral density. We did not experimentally measure the exact particle size distribution in the strontium sulfate layer, but from Eq. (2) we estimated an effective particle diameter of 6 μm for a permeability of 1×10^{-14} m^2 and for a porosity of 0.33. This diameter is well below the lower limit of the assumed overall particle size distribution, which indicates that the average pore width is much smaller than expected for a medium with circular shaped pores. It seems quite possible that during mixing and compaction of the strontium layer in the tanks some of the mechanically unstable grains are segmented into smaller particles which would shift an averaged grain size to smaller values. In addition, the orthorhombic shape of strontium sulfate particles will induce more slit shaped pores which further reduce the permeability (Ozgumus et al., 2014).

The Plexiglas tank was placed on its side and filled through the lid: to a depth of 4.5 cm with quartz sand, followed by 1 cm of strontium sulfate, and then again 4.5 cm of quartz sand. The lid was closed and the tank turned to the position shown in Fig. 1. The tank was then flushed with carbon dioxide (CO_2) to remove the air from the pores. The high solubility of CO_2 enabled the whole porous medium to be completely saturated with a saturated solution of strontium sulfate. A saturated solution of strontium sulfate was used instead of pure water to avoid dissolution of the reactive medium. The solution was injected into the tank at a flow rate of 100 μL min^{-1} (1.67×10^{-9} m^3 s^{-1}) using a syringe pump which delivered a continuous constant flow rate without any pressure variation (unlike a peristaltic pump). All the experiments were performed at 25 ± 1 °C.

2.1.1. Transport experiments without chemical reaction

Before conducting reactive transport experiments, we conducted transport experiments with conservative dye tracers in order to investigate the homogeneity of porous media, the steady state flow field and the system response to the injection of a dense solution.

Prior to making the tracer test, a saturated solution of strontium sulfate was injected in the tank for at least 24 h to establish a steady state flow field. In order to make visible the steady state flow field, and to detect any inhomogeneity in media packing or preferred flow paths along the Plexiglas walls, we injected a pulse (0.5 mL at rate of ~20 μL min^{-1}) of dye tracer (eosin 3 g L^{-1}) at the inlet followed by a continuous inflow of a saturated solution of strontium sulfate at a flow rate of ~20 μL min^{-1} (3.33×10^{-9} m^3 s^{-1}). The flow path of the tracer in the tank was monitored by taking pictures at intervals of 3 min for about 20 h (experiment 1).

In a second experiment (experiment 2), the effect of injecting a liquid with a different density was investigated. This was necessary because in the reactive transport experiments, it was planned to use a highly concentrated barium chloride solution which has a much higher density than the strontium sulfate saturated solution initially present in the tank. In this test a non-reactive sodium chloride solution — saturated w.r.t. strontium sulfate — and matched to the density of the barium chloride solution to be used later, was injected into the tank at a flow rate of ~20 μL min^{-1}. The flow field was again made visible by injecting a pulse (0.5 mL at rate of ~20 μL min^{-1}) of the dye tracer eosin (3 g L^{-1}) matched to the density of that of the sodium chloride solution. The flow path of the tracer in the tank was monitored by again taking pictures at intervals of 3 min for about 20 h.

2.1.2. Reactive transport experiment

The actual reactive experiment is named experiment 3. A 0.3 mol L^{-1} solution of $BaCl_2$ was injected at a flow rate of ~20 μL min^{-1}. Before the injection of barium chloride, 10 mL of milliQ water followed by a tracer pulse (0.5 mL at rate of ~ 20 μL min^{-1}) were injected in the sand compartment. The injection of water avoided a precipitation front between the saturated solution of strontium sulfate and the barium chloride solution injected.

correction for equation (3) $d_m = \left[\sum_i \frac{f_i}{d_i}\right]^{-1}$

The injection of barium chloride into the tank enhances the dissolution of strontium sulfate and barium sulfate precipitates:

$$BaCl_{2(aq)} + SrSO_{4(s)} \rightarrow BaSO_{4(s)} + SrCl_{2(aq)}. \tag{4}$$

The dissolution of 1 mol of strontium sulfate followed by the precipitation of 1 mol of barium sulfate results in a volume increment of 5.85 mL and thus in a decrease in the porosity from 0.33 to 0.25 within the reactive medium (strontium sulfate region).

During the course of the experiment, the effluent and samples at port “c” and “d” were collected at different times. The amount of effluent collected per unit time was used to calculate the flow rates given in Table 2. Samples were analysed by ion chromatography (DIONEX, DX500). Sampling from the ports disturbs the flow field and also the spatial/temporal distribution of concentrations throughout the tank since liquid is removed from the system. To minimise this interference, the sampling volumes were kept as small as possible (100 μL) and time gaps of 24 h were set between samplings. The differential pressure between ports “a” and “b” was also monitored.

Conservative tracer tests during barium chloride injection were performed by injecting 0.5 mL of eosin at 20 μL min^{-1} at the inlet every 24 h and taking pictures of the tank every 3 min. The density of the eosin solution was identical to the density of the barium chloride solution. The effluent was collected at different time intervals and analysed.

At the end of the barium chloride injection, the tank was flushed with gaseous carbon dioxide from the outlet to remove the pore water which was then analysed. This measurement gave an estimate of the amount of unreacted barium chloride in the tank. The system was re-saturated by injection of a solution equilibrated w.r.t. both strontium and barium sulfate, to avoid dissolution of the reactive medium. On the long term for contact times of weeks, this solution can react with the reactive medium and form solid solutions, but the reactive medium can be considered unreactive during the relatively short time scale of the tracer test. A tracer test similar to the one described in experiment 1 was performed during the injection of the solution. The tracer profile was monitored over 20 h. This last tracer test was named ‘final tracer test’. The test allowed changes in the flow field to be evaluated and helped to identify where porosity changes and consequently permeability changes in the tank had occurred.

Finally, the tank was flooded with isopropanol to stop any further chemical reactions.

2.1.3. Post mortem analysis

Once the experiments were completed, the tank was opened and it was observed that the reactive medium had hardened into a rectangular block. After removing and drying, the reactive medium was cut into 1 cm thick segments. Elemental mappings of the reactive medium were performed by X-ray fluorescence. Some samples from the reactive layer were crushed to a grain size of ~10 μm to determine the mineralogy by X-ray diffraction (XRD). The micro-structure of the reacted medium was investigated by optical and scanning electron microscopy. Micro-XRD techniques were also used to determine the chemical composition/nature of a newly formed phase.

2.2. Numerical models

The flow and transport equations are solved by OpenGeoSys (Kolditz and Bauer, 2004; Xie et al., 2007) and the chemical processes by GEM-Selektor V3 (Kulik et al., 2013; Wagner et al., 2012). The coupling between both codes as well as the capabilities of the coupled codes, are described in Shao et al. (2009) and Kosakowski and Wanatabe (2013).

The experiments were modelled in a 2D geometry discretised in a triangular Finite Element (FE) grid of 1 mm–500 μm (depending on the experiment). The initial conditions in the two tanks are given in Table 1 and the boundary conditions for the three experiments are summarised in Table 2. The permeability of the reactive medium depends on the arrangement of the strontium sulfate crystals during the filling of the tank. The permeability values given in Table 1 are values fitted to match the experimental results (lying within the range measured experimentally with the falling head method). The flow rate for each experiment is given in Table 2. Density driven flow, due to the high concentration of barium chloride injected, was also considered in our model. In OpenGeosys-GEM the liquid phase density is calculated by GEMS numerical kernel as the mass to volume ratio of the liquid phase, estimated from the composition of the liquid phase. The liquid phase density obtained after each chemical equilibrium calculation is passed to the flow solver for use during the next time step.

The Boussinesq approximation was implemented in the liquid flow module, i.e., the density variations are neglected in the mass balance equation of the fluid phase. Density driven flow is included by the buoyancy term of the Darcy equation only.

For variable-density flow in porous medium, the Darcy velocity, q (m s^{-1}), is given as:

$$q = -\frac{k}{\mu}(\nabla p - \rho g) \tag{5}$$

where k is the permeability (m^2), μ is the dynamic viscosity (Pa s) of fluid, ∇p (Pa) is the pressure gradient, ρ is density of fluid (kg m^{-3}) and g is the gravitational acceleration (m^2 s^{-2})

The reactive transport equations are given in Bear and Bachmat (1990):

$$\frac{dC_i}{dt} = -\nabla\left(\frac{q}{w}C_i\right) + \nabla(D_i \nabla C_i) + Q_i \tag{6}$$

$$\frac{dC_i}{dt} = \Gamma_i(C_i \ldots C_m) \tag{7}$$

where i = 1, 2, 3… m, C_i (mol m^{-3}) denotes the molar concentration of the ith species of an m multi-species system; q is the Darcy velocity (m s^{-1}) of liquid flow, D_i is the diffusion–dispersion coefficient of component i (assumed to have the same value for all components in our models); Q_i is the source/sink term and Γ_i $(C_i \ldots C_m)$ is the source/sink term of species i due to equilibrium chemical reactions with other species.

The thermodynamic data (standard Gibbs energy of formation [kJ mol^{-1}]) of aqueous, gaseous and solid species considered in the chemical system, and the molar volumes [m^3 mol^{-1}], are based on the PSI/NAGRA thermodynamic database (Hummel et al., 2002) and are given in Table 4 in the

Table 1
Properties of the different regions of porous media.

Characteristics	Q1	Q2	Q3	Q4
Width (x-axis) [m] (always unless specified)	0.045	0.0105	0.0445	NA[a]
Width (x-axis) [m] tank 1 experiment 3 scenario 2	0.045	0.0095	0.0445	0.001
Initial porosity (w_0) experiment 1	0.34	0.33	0.40	NA
Initial porosity (w_0) experiment 2	0.36	0.34	0.40	NA
Initial porosity (w_0) experiment 3 scenario 1	0.34	0.33	0.40	NA
Initial porosity (w_0) experiment 3 scenario 2	0.34	0.355	0.40	0.10
Initial permeability k_0 [m^2] experiment 1	1.82×10^{-11}	5.0×10^{-14}	1.82×10^{-11}	NA
Initial permeability k_0 [m^2] experiment 2	1.82×10^{-11}	5.0×10^{-14}	1.82×10^{-11}	NA
Initial permeability k_0 [m^2] experiment 3 scenario 1	1.82×10^{-11}	5.0×10^{-14}	1.82×10^{-11}	NA
Initial permeability k_0 [m^2] experiment 3 scenario 2	1.82×10^{-11}	6.0×10^{-14}	1.82×10^{-11}	2.0×10^{-14}
Dispersivity α [m]	10^{-4}	10^{-4}	10^{-4}	10^{-4}
Molecular diffusion coefficient D_0 [$m^2\ s^{-1}$]	10^{-9}	10^{-9}	10^{-9}	10^{-9}
Volume fraction of quartz experiment 1	0.66	0.00	0.60	NA
Volume fraction of quartz experiment 2	0.64	0.00	0.60	NA
Volume fraction of quartz experiment 3 scenario 1	0.66	0.00	0.60	NA
Volume fraction of quartz experiment 3 scenario 2	0.66	0.00	0.60	0.00
Volume fraction of $SrSO_4$ experiment 1	0	0.67	0	NA
Volume fraction of $SrSO_4$ experiment 2	0	0.66	0	NA
Volume fraction of $SrSO_4$ experiment 3 scenario 1	0	0.67	0	NA
Volume fraction of $SrSO_4$ experiment 3 scenario 2	0	0.645	0	0.90
Initial pH	5.5	5.5	5.5	5.5

[a] NA stands for non-applicable. Q4 is a 1 mm domain between Q1 and Q2.

appendix. Molar weights and densities for all components and mineral phases are calculated in the GEM-Kernel based on the molar weights of the elements given in the appendix (Table 5).

Two scenarios were used to describe the reactive transport experiments and are described in details in Section 3.3.2. In scenario 1 the experimental setup is represented by three domains Q1, Q2 and Q3 as shown in Fig. 1. For scenario 2, a 1 mm wide domain, Q4 where smaller strontium sulfate particles intermix with sand is introduced. Q4 embodies a region that could have resulted from a stratification of the reactive media during the filling of the tank.

As a result of dissolution/precipitation reactions, porosity changes occur. Transport properties such as effective diffusion coefficients D_e and the permeability k_s of the medium are parameterised as a function of porosity.

For the dependence of the effective diffusion coefficient, D_e, on porosity we used a simplified Archie's law (Archie, 1942):

$$D_e = D_o w^m \tag{8}$$

where D_o [$m^2\ s^{-1}$] is the diffusion coefficient in water, w [–] is the porosity and m [–] is an empirical coefficient set to 1.

Changes of permeability k_s [m^2] with porosity are given by a modified Kozeny–Carman equation:

$$k_s = k_0 \left(\frac{w}{w_0}\right)^3 \tag{9}$$

where k_0 [m^2] is the initial permeability, w [–] and w_0 [–] are the actual and initial porosities respectively. This expression is compatible with the Kozeny–Carman equation given in Eq. (2) provided that variation in d is negligible and that the weak variation in w causes $1 - w$ to be constant.

The temporal quantities of strontium sulfate and barium sulfate, and consequently also the porosity evolution, depend on the reaction kinetics. The kinetic rate dm/dt [mol s^{-1}] is calculated following Palandri and Kharaka (2004). In our simulations, the simplest reactive surface area SA [m^2] model of those implemented in OGS-GEM was chosen:

$$SA = V_i a_i \tag{10}$$

where V_i [m^3] is the volume of the mineral and a_i [$m^2\ m^{-3}$] is the relative surface area per volume unit.

In our simulations, barium sulfate was assumed to precipitate instantaneously (very fast kinetics) and only the kinetic dissolution of strontium sulfate was taken into account. The dissolution kinetic rate of strontium sulfate at pH = 5.5 (pH of the experiment) is calculated based on the equation given in Palandri and Kharaka (2004) with parameters from Dove and Czank (2005).

$$\frac{dm}{dt} = -SA\left(k^{298.15} \exp\left(\frac{-E}{R}\left(\frac{1}{T} - \frac{1}{289.15}\right)\right)(1-\Omega)\right) \tag{11}$$

where SA [m^2] is the reactive surface area of strontium sulfate mineral phase, $k = 10^{-5.66}$ mol $m^{-2}\ s^{-1}$ is the dissolution rate constant at 298.15 K, $E = 23.8$ kJ mol^{-1} is the activation energy for describing the temperature T [K] dependence, R [J $mol^{-1}\ K^{-1}$] is the gas constant, and Ω [–] is the saturation index calculated as the ratio of reaction activity quotient and

Table 2
Boundary conditions of the experiments and modelling time duration.

Boundary conditions	Experiment 1	Experiment 2	Experiment 3
Source term [μL min^{-1}]	18.52	19.00	19.75
NaCl concentration [mol L^{-1}]	NA	1.4	NA
$BaCl_2$ concentration [mol L^{-1}]	NA	NA	0.3
Pressure at outlet [Pa]	101,325	101,325	101,325
Modelling time duration (h)	24	24	200

the equilibrium constant. The GEMS3K software used in this study actually calculates the phase stability index, which can be shown to be equivalent to the above saturation index (Kulik et al., 2013).

The characteristic time scales for transport were evaluated and are summarised in Table 3. To avoid time and space discretisation producing physically unrealistic solutions (such as negative concentrations and numerical oscillations), the chosen time stepping should always respect the Courant number and Newmann criterion (Rausch et al., 2005; Zheng and Bennett, 1995) The two criteria can lead to extremely small time step sizes and as a result huge calculation times, especially when the mesh size is small. To save calculation time for experiment 3, the numerical mesh (Δx) was only refined to 5×10^{-4} m in regions with high concentration gradients: the inlet, the Q2 region and at the outlet. A self-adaptive time stepping scheme which ensures that the von Neumann criterion and Courant number are always respected, was chosen. During the course of our experiment, we always ensured that the mass transport time from one Finite Element node to a neighbouring node is larger than the time required for reaction (Damköhler number > 1).

3. Results and discussion

3.1. Experimental results

3.1.1. Advective transport experiments

The experimental results from experiments 1, 2 and 3 are presented below.

The conservative tracer test in experiment 1 is shown in Fig. 2. The tracer fronts in the quartz sand regions are smooth, with no apparent fingering, suggesting a homogeneous packing of the quartz regions. The tracer fronts in the strontium sulfate region are not smooth, suggesting some heterogeneity in the reactive medium. The tracer test was used to estimate the seepage velocities in the tank. The seepage velocity is presented in Fig. 6. It was evaluated from the movement of the concentration maxima along line 1, line 2 and line 3 on pictures taken at hourly intervals.

The conservative tracer test performed during sodium chloride injection (experiment 2) is presented in Fig. 3 (left column). Instead of a circular front as in Fig. 2 the fluid with high density fills the left compartment of the tank first and only crosses the reactive medium after a certain pressure difference between the left and right compartments is reached.

3.1.2. Reactive transport experiment

The injection of barium chloride shows initially the same effects of density driven flow to that of the sodium chloride injection. After 100 h of $BaCl_2$ injection, the tracer test pictures (not illustrated) showed changes in the flow path. The final tracer test showed significant changes in the flow field compared to the control test with a conservative tracer (Fig. 2), indicating local permeability (and porosity) changes due to the chemical reaction taking place in the tank. For the initial unreacted system the tracer front can relatively easily cross the reactive layer. The final tracer test shows a distinct tendency of the tracer to move parallel to the reactive layer and then cross the reactive layer near the top through a small crack. This is a typical behaviour observed in different repetitions of the experiment.

In addition, the eosin sticks to the reactive medium during the barium chloride injection, as indicated by the red colour. Such a behaviour was not observed during the injection with a sodium chloride solution.

Several experiments with the "same" initial and boundary conditions were repeated and stopped at different times (from 10 h to 300 h of barium chloride injection). The results were similar until strong permeability changes or clogging occurred. Indeed, after clogging, the tracer tests revealed cracks in the reactive medium or preferential flow paths along the upper side of the tank. The experiments can be considered as reproducible (deduced by the results presented in Fig. 14 in the appendix from two different tank experiments showing the mineral evolution with time). Differences are mainly related to the inability to exactly reproduce the initial packing of the sand and strontium sulfate regions. Estimated porosity values differ typically by 0.02 between different packing/compaction and permeability values for the

Table 3
Characteristic time scales for transport and chemical processes.

	Flow and mass transport Experiment 1 $U_{max} \sim 10^{-5}$ m s^{-1}	Density driven flow and mass transport Experiment 2 $U_{max} \sim 10^{-5}$ m s^{-1}	Reactive transport Experiment 3 $U_{max} \sim 10^{-5}$ m s^{-1}
Size discretisation cell, Δx [m]	1×10^{-3}	1×10^{-3}	5×10^{-4} 1×10^{-3}
Dispersivity α [m]	10^{-4}	10^{-4}	10^{-4}
Advective time [s]	100	100	50
$\Delta t_1 = \frac{\Delta x}{U}$			100
Courant number			
$\Delta t \times \frac{U}{\Delta x} < 1$			
Diffusive–dispersive time [s]	500	500	125
$\Delta t_2 = \frac{\Delta x^2}{(\alpha U + D_0)}$			500
Peclet number	5	5	2.5
$\frac{\Delta t_2}{\Delta t_1}$			5
von Neumann criterion [s]	500	500	125
$\Delta t < \frac{1}{2} \times \frac{\Delta x^2}{D_0}$			500
Damköhler number	NA	NA	$Da > 1$
$Da = \frac{\Delta x}{U} \times SA \times k$			

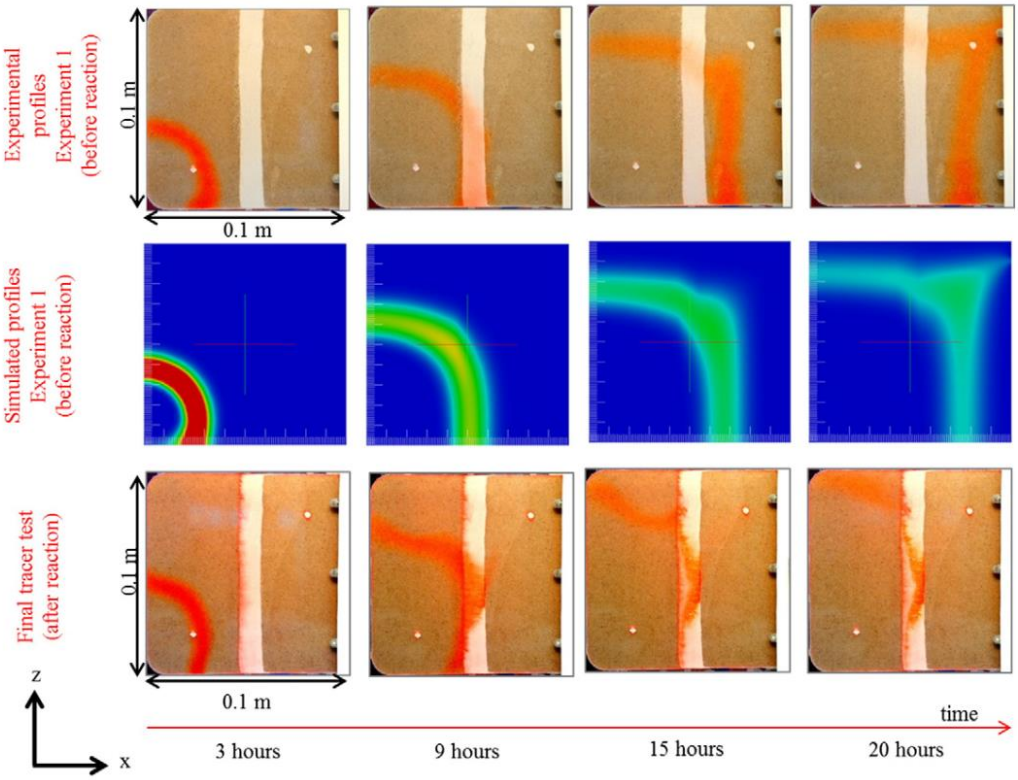

Fig. 2. The experimental and simulated tracer profiles of experiment 1 (1st and 2nd row) before reaction, and the final tracer test (3rd row) after reaction. The observed differences between experiment 1 and final tracer test are due to permeability changes of the strontium sulfate layer.

strontium sulfate were found to be between 1×10^{-14} m^2 and 6×10^{-14} m^2.

A net pressure increase of up to 8 mbar was recorded in one of our experiments. The relative pressure increase with time is given in Fig. 11. A net pressure increase with time was observed with some scattered points. The scattered points can be due to samplings at ports which are likely to affect the pressure measurement.

3.1.3. Mineral evolution in the tank

The effluents from the tank, as well as samples at ports “c” and “d”, were collected at different times and analysed. The amounts of barium chloride injected and the ionic concentrations of the effluents were used to calculate the amount of reacted mineral in the tank. The temporal evolution of the quantities of barium sulfate and strontium sulfate is shown in Fig. 9. The slope of the curves corresponds to average reaction rates in the tank. For the various experiments carried out, the rate of barium sulfate precipitation was ~5.6×10^{-8} mol s^{-1} (2.0×10^{-4} mol h^{-1}). This rate is lower than the injection rate of barium chloride of 1×10^{-7} mol s^{-1} (3.6×10^{-4} mol h^{-1}) which indicates that not all barium chloride reacted. After 180 h, 0.114 ± 0.002 mol of strontium sulfate remained undissolved and 0.038 ± 0.02 mol of barium sulfate precipitated. The amount of strontium sulfate dissolved is equal to the amount of barium sulfate which precipitated. The mineral changes which occurred corresponded to an average decrease in porosity of 6.8%. The mineralogy of the reactive medium was analysed by XRD. Sample S2 collected in the Q2 (between $z = 0.00$ m and $z = 0.01$ m) revealed the presence of up to 34 wt.% of barium sulfate, up to 64 wt.% strontium sulfate, 1.3 wt.% weight of a strontium rich solid solution with the rest being quartz contaminants. XRF results of the reactive medium revealed a barium enrichment zone at the interface as shown in Fig. 4. At the quartz–strontium sulfate interface, an ~50 μm (resolution of XRF probe) barium and sulfur enrichment zone could be distinguished. The silicon (Si) detected at the interface is originally not part of the reactive medium. We believe that some quartz grains are cemented with the reactive medium after reaction. This is discussed more in details in Section 3.3.2. The elemental mapping of barium and silicon are complementary. Strontium appears depleted in the barium enrichment zone region. It is also worth noting that no distinct precipitation front of barium sulfate was seen after 300 h of $BaCl_2$ injection.

Fig. 5 shows a microscopic view of the interface. Undissolved large strontium sulfate crystals covered with a thin brownish layer can be distinguished. This layer was identified as barium sulfate by Micro-XRD. This rim around the strontium sulfate can be more easily distinguished in the back-scattered mode in the SEM microscope. In addition, a brownish phase (which looks amorphous under polarised light) can be seen to precipitate in between the big strontium sulfate crystals in the optical thin section image. Micro-XRD analysis showed the brownish phase to be nano-crystalline barium sulfate which precipitates all over the reactive medium although it looks to be slightly more concentrated where the

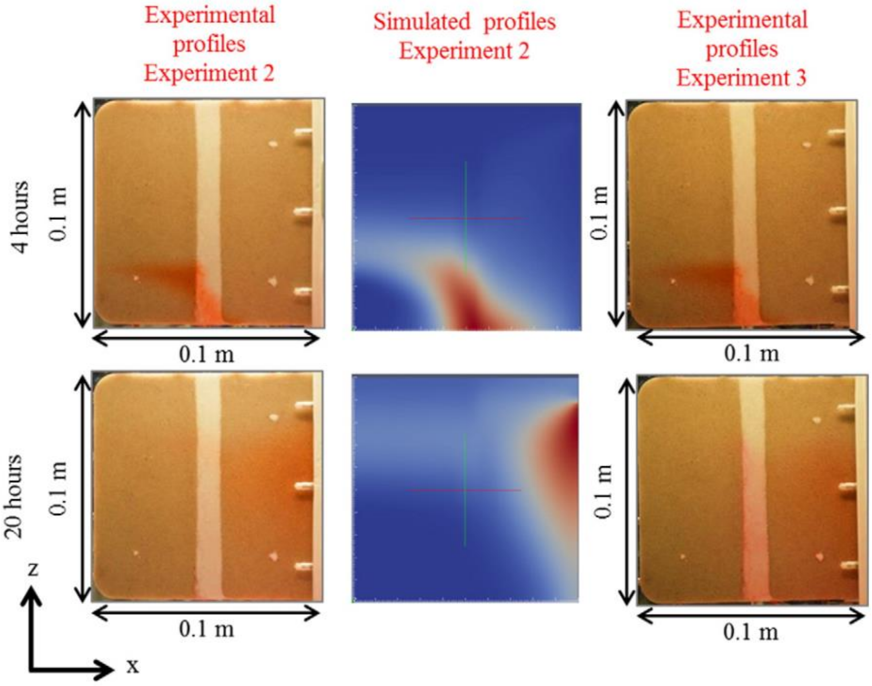

Fig. 3. Experimental tracer profiles of density driven flow during sodium chloride injection, experiment 2 (left column), simulated tracer profiles (middle column) and the density driven flow due to barium chloride injection, experiment 3 (right column) at 4 h and 20 h.

barium enrichment zone was found. This nano-crystalline phase cements all the thinner and larger strontium sulfate particles together, creating bottlenecks (unconnected porosities) in some cases.

3.2. Summary of experimental results and their interpretation

Tracer tests prior to barium chloride injection revealed a homogeneous packing of the quartz sand and some heterogeneities in the strontium sulfate reactive medium.

The injection of barium chloride in the quartz sand porous medium induced a density driven flow. Tracer tests made during the barium chloride injection showed that eosin dye sticks to the reactive medium. This might be caused by the entrapment of eosin in dead end pores or isolated pores during barium sulfate precipitation. In addition, sorption of the negatively charged eosin molecule on the reactive medium on the positively charged surface of the barium sulfate formed cannot be excluded. According to Bokern et al. (2003), barium sulfate becomes positively charged when it precipitates in a barium ion rich solution. The reddish colour of the reactive medium thus gives an indication of where barium sulfate has precipitated. The sorption coefficient of eosin onto $BaSO_4$ in batch experiments was not determined in the present study and will not be considered in our current modelling.

Changes in flow path were seen to occur between 100 and 125 h after injection of barium chloride. In some experiments, preferential flow paths along either cracks, or at the top of the tank, were created. The time at which changes in flow paths were observed corresponded to the time at which the concentration of strontium collected in the effluents fell to a zero value and the concentration of Ba^{2+} started to increase suggesting that reactions had stopped. During the first 100 h of barium chloride injection there was a linear increase in the

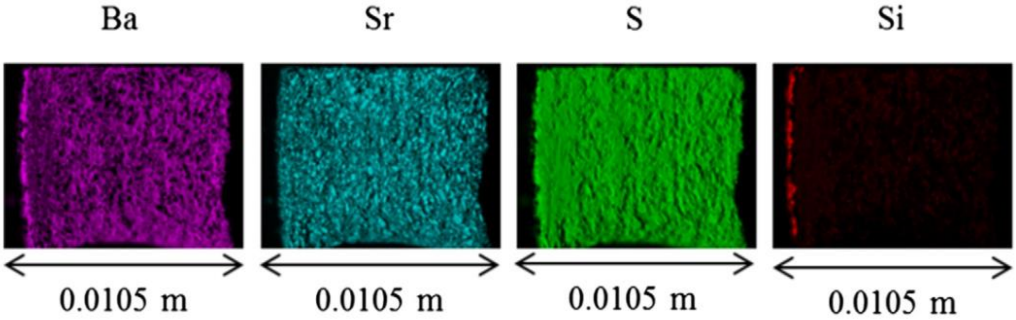

Fig. 4. Cross sectional view in the x–y plane of elemental profiles of sample S2 collected at z = 0.0216 m after 300 h of barium chloride injection.

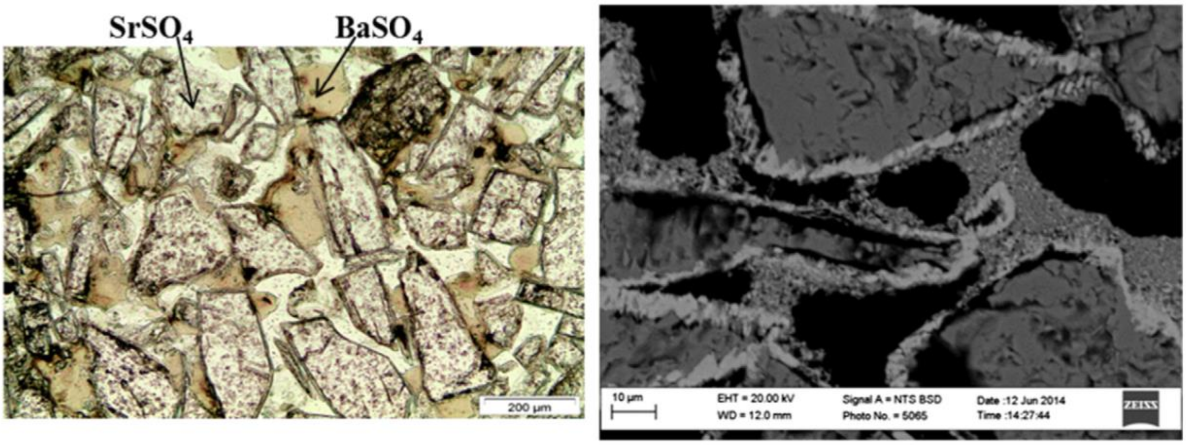

Fig. 5. Microscopic view of cross sectional area (x–y plane) of the strontium sulfate region (left optical microscope, right scanning electron microscope, BSE (Back Scattered Electron) image).

amount of barium sulfate formed, which indicates a constant average reaction rate in the tank. After 100 h, the rate was decreasing with time. The amount of barium sulfate precipitating per unit time (mol s^{-1}) was equal to the amount of strontium sulfate dissolving per unit time (slopes of the curves given in Fig. 9). The amount of barium sulfate precipitated per unit time was lower than the amount of barium chloride injected per unit time, which suggested that the dissolution of strontium sulfate controlled the global rate of reaction.

XRD results confirmed the precipitation of barium sulfate. Also, small amounts of a strontium rich solid solution were produced. As barium chloride was injected at a relatively high flow rate and at a relatively high concentration of 0.3 M, the formation of a solid solution which contains a significant fraction of $SrSO_4$ was not expected. Indeed, based on the ideal $(Ba,Sr)SO_4$ Lippmann diagram reported by Prieto et al. (1993), the precipitation of strontium-rich solid solutions occurs only when the aqueous phase is extremely poor in Ba^{2+}.

The samples collected and analysed by the XRD techniques showed that about 30% of the initial quantity of strontium sulfate had reacted. This is in agreement with the 25 wt.% of strontium sulfate evaluated to have reacted from mass balance considerations. A more rigorous comparison was however not

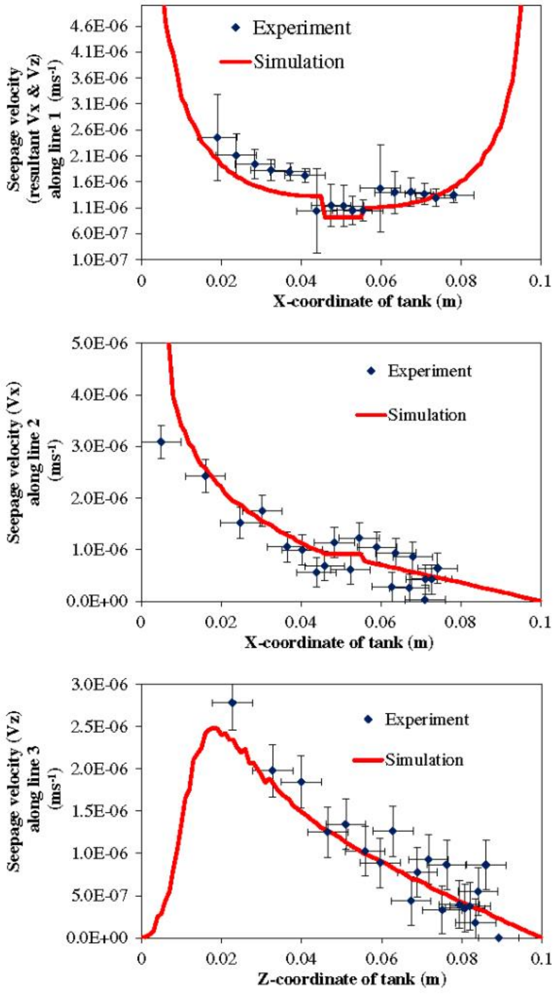

Fig. 6. The experimental seepage velocities and simulated seepage velocities across line l, line 2 and line 3 during experiment 1.

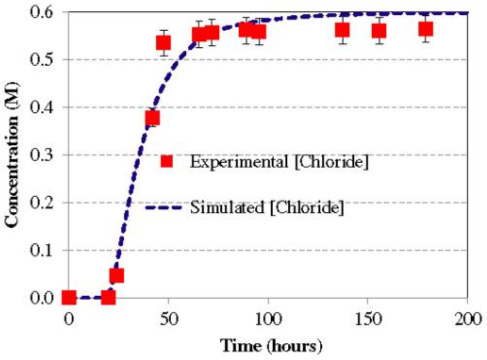

Fig. 7. Experimental and simulated chloride concentration at the outlet during barium chloride injection, experiment 3.

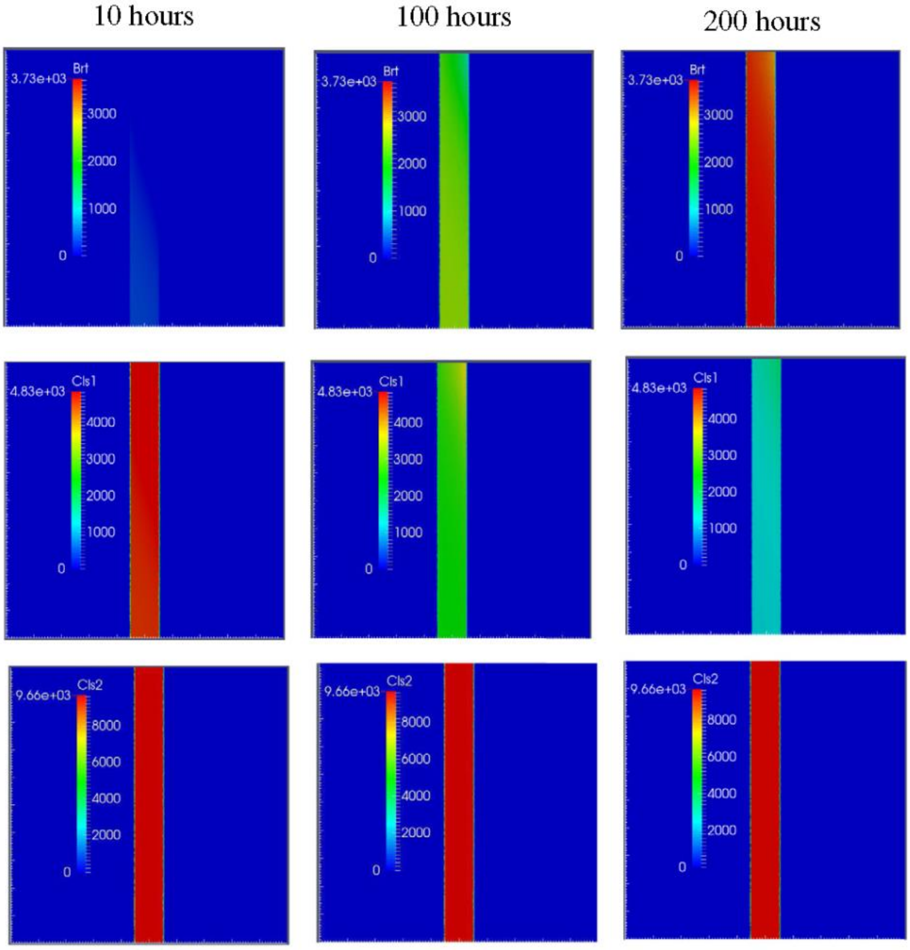

Fig. 8. Scenario 1 simulated mineral profiles at 10 h, 100 h and 200 h (from top to bottom) barium sulfate (Brt), small grains strontium sulfate phase (Cls 1) and large grains strontium sulfate phase (Cls 2).

possible because the whole of the strontium sulfate reactive medium was not crushed and analysed. Some samples were taken and impregnated for XRF analysis. Elemental mapping by XRF techniques of the strontium sulfate reactive medium revealed the transformation of part of the strontium sulfate into barium sulfate homogeneously throughout the reacted layer and the formation of a barium enrichment zone at the interface. SEM analysis of the cross section of the reacted medium showed that big strontium sulfate crystals were covered by a barium sulfate rim, and that a barium sulfate nano-crystalline phase precipitated in the pore space cementing together the big crystals of strontium sulfate. Barium sulfate precipitated as a nano-crystalline solid, because precipitation in strongly oversaturated conditions favours nucleation and agglomeration of many small crystals and suppresses growth of large crystals (Kashiev and Van Rosmalen, 2003).

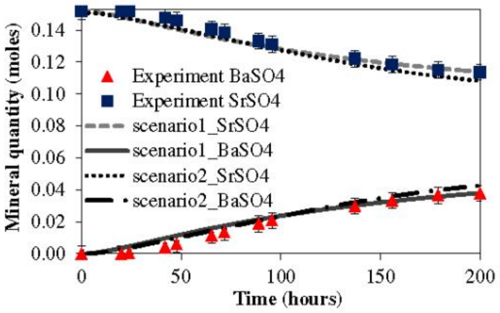

Fig. 9. Temporal evolution of the minerals present in the tank according to scenario 1 and scenario 2.

After 100 h of barium chloride injection, the measured concentrations of Sr^{2+} and Ba^{2+} at the outlet suggest that both strontium sulfate dissolution and barium sulfate precipitation had stopped. The slowdown of reaction rates might be caused by the development of preferential flow paths along the top of the tank or along small cracks in the strontium sulfate reactive medium. The bulk of the $BaCl_2$ solution probably no longer flowed through the reactive medium. In addition, the passivation of the strontium sulfate crystals due to barium sulfate overgrowth limited reaction rates.

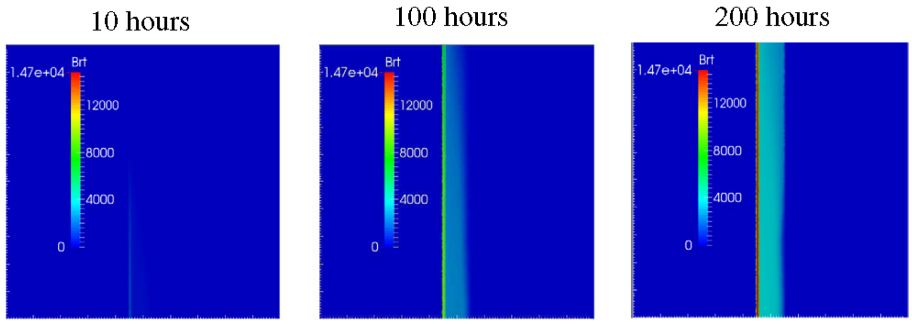

Fig. 10. Scenario 2 simulated barium sulfate (Brt) profile at 10 h, 100 h and 200 h.

The mineral changes which occurred corresponded to an average decrease in porosity of 6.8% (average porosity drops from 0.331 to 0.308). This small decrease in the average porosity of the reactive medium does not exclude a strong local porosity decrease over a few 100 μm at the interface. Indeed, mass balance considerations used to evaluate porosity changes do not give any information on where barium sulfate precipitates and how it affects pore geometry and pore connectivity. As noted before, under our experimental conditions, barium sulfate precipitates as nano-crystals (mainly nucleation processes) that are likely to agglomerate in the pore space. When such an agglomeration of particles occurs at bottlenecks between bigger crystals or sand grains, strong permeability decrease is observed.

However, how the smaller strontium sulfate particles dissolve, how barium sulfate nano crystals form and how they agglomerate in the pore throats is not fully understood. Questions still remain on whether the newly formed barium sulfate nanocrystals settle instantaneously in the pore space after precipitation, or if they are mobile and agglomerate later at narrow pore throats. Clogging by particle dragging was reported by Luquot et al. (2014). The authors, studying the porosity and permeability increase due to limestone dissolution triggered by CO_2 injection, also observed porosity and consequent permeability decrease close to the outlet. If particle dragging took place in the tank, barite should also be found in the Q3 (sand) region. CT scan of the tank after reaction and powder XRD analysis of the sand from the Q3 region after reaction indicated the absence of barium and strontium mineral phase. To completely exclude particle dragging in our experiment, μ-XRD powder measurement (more precise and more appropriate for our experimental problem) on sand samples collected in the Q3 region will have to be carried out.

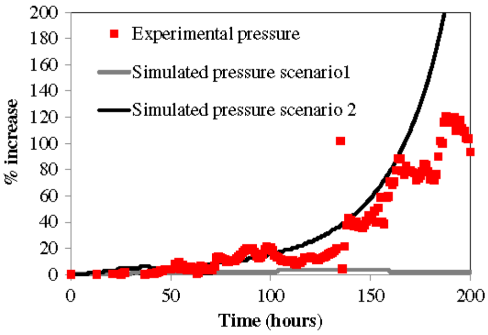

Fig. 11. Net pressure increase during 200 h of barium chloride injection.

XRF measurement on samples from an experiment which was aborted after 10 h of injection of barium chloride, showed non-uniform progress of barium sulfate reaction fronts across the width of the tank. Reaction fronts progressed about 1 mm further in flow direction along the walls of the tank than in the centre. This suggests preferential flow paths along the sides of the tank.

It is also important to note that we do not have any evidence of complete clogging. The porosity network of the reactive medium will be investigated at a later stage by micro-X-ray tomography techniques.

3.3. Modelling results

3.3.1. Modelling the transport experiment with no chemical reaction

The experimental flow field, characterised by the conservative dye tracer tests, was compared to calculations with the numerical model and a good agreement between experiment and model was achieved as can be seen in Fig. 2.

Fig. 6 compares the experimental seepage velocities across lines 1, 2 and 3 during experiment 1 with the simulated seepage velocities. The simulated velocities are in good agreement (simulated values lies within a range ±20% of experimental values). The velocities, Vz and Vy, from which the resultant velocity for line 1 is calculated, are also provided in the appendix (Fig. 12). The initial porosity of the reactive medium from mass balance consideration was 0.32. A sensitivity analysis on experiment 1 showed that a value of 0.33 reproduced more accurately the observed migration of the conservative tracer.

The permeability of sand compacted to a porosity of 0.35 was measured to be $(1.82 \pm 0.2) \times 10^{-11}$ m^2. This measured value was used for the sand in the Q1 and Q3 region compacted to a porosity of 0.34 and 0.40 respectively. Using the Kozeny Carman equation (Eq. (2)) the permeability is expected to be slightly higher (~3.15×10^{-11}) m^2. The calculated results are however not sensitive to changing the value permeability from 1.82×10^{-11} m^2 to 3.15×10^{-11} m^2, as the effective permeability of the tank in flow direction is dominated by the much lower permeability of the reactive media (~weighted harmonic mean of the three regions). The porosity in the Q3 region does not change during the reaction, and thus fixing the same measured permeability value for compartment Q1 and Q3 has no significant impact on the final results.

The sensitivity of conservative tracer transport on the choice of the dispersion length α was investigated. Values for α of 1×10^{-5} m, 1×10^{-4} m, 1×10^{-3} m and 1×10^{-2} m were tested. The calculated tracer profiles for the different dispersive length were qualitatively compared with the experimental tracer profile (Fig. 13 in appendix). It was found, that a value slightly higher than the grain size (1×10^{-4} m) is a reasonable choice for conservative transport.

The modelled density driven flow for the sodium chloride injection was reproduced by OGS-GEM. Fig. 3 compares the experimental and modelled density driven flow.

3.3.2. Modelling the reactive transport experiment

For the reactive transport modelling, grid convergence was first tested. It was found that for a grid size of smaller than 500 μm only negligible changes were observed for porosity and mineral transformations with time. We also run an additional 1D test problem on the diffusion of $BaCl_2$ in a 3 cm long column composed successively of 1 cm wide layers of SiO_2, $SrSO_4$ and again SiO_2. Different grid sizes (500 μm, 100 μm and 50 μm) were tested. No significant difference in porosity changes with time was observed. To save calculation time, a grid size of 500 μm for the reactive medium was thus used in the numerical models describing experiment 3.

In our modelling approach, we did not consider the sorption of the dye tracer onto barium sulfate, thus the modelled tracer profiles during barium chloride injection (not presented) are similar to the modelled tracer profiles during sodium chloride injection.

As chloride ions are unreactive during the transport, i.e., chloride ions stays in solution and no chlorine containing solid phases are formed; it can be used as a conservative tracer. The modelled and experimental breakthrough curves (shown in Fig. 7) of chloride ion are in good agreement.

Based on the information collected at the microscopic level, two different scenarios (denoted hereafter as scenarios 1 and 2) were modelled.

Scenario 1 The dissolution of strontium sulfate was constrained by the kinetic law given in Eq. (11). The strontium sulfate reactive medium used in the experiment consisted of large and smaller crystals, and therefore two different dissolution rates were applied in the model. Relative surface area per volume unit, $a_{(SrSO_4)}$, of 20,000 and 100 $m^2\ m^{-3}$ were attributed to the small and large crystals respectively. The reactive surface areas were not set at the measured BET surface areas since this gave dissolution rates which were too high. Instead, the reactive surface areas were set to values about one order of magnitude smaller than the BET surface area. BET surface areas are evaluated based on the adsorption of gas molecules on the surface of dried mineral grains. It might be that the accessibility to gas molecules in a BET measurement is much higher than the accessibility of aqueous species in a saturated porous media. The average specific surface area might be decreased, if pores exist that are not completely accessible to the solution due to inter-crystal grain boundaries (crystal grain contacts between each other). Strontium sulfate grains are normally non-spherical and therefore the crystal grain contact areas are enhanced. Furthermore, hydration of and sorption on minerals inhibits surfaces which also decreases the average reactive surface area. A similar difference between the measured BET surface areas and the ones needed to reproduce experimental observations of quartz dissolution was reported by Gautier et al. (2001). Under our experimental conditions it is assumed that barium sulfate precipitated at thermodynamic equilibrium as a nano-crystalline solid and no kinetic constrain on the precipitated phase was applied.

Scenario 2 Scenario 2 was based on a possible stratification of strontium sulfate particles which could occur during the filling of the tank. Finer strontium sulfate particles could settle in between the quartz sand particles at the interface and create a thin region of lower porosity at the interface between sand and the reactive medium. The original thickness and porosity of this ‘mixing zone’ referred as Q4 is unknown. If we consider a direct flow path along a pipe from port “a” to port “b”, and if we assume that observed pressure changes are only due to the changes in transport properties occurring over the Q4 region, the permeability change of the Q4 region can be estimated. For a given thickness of the Q4 region of 50 μm and 1 mm of the reactive medium, the permeability is estimated to decrease by 2 and 1 orders of magnitude respectively to double the pressure difference between port “a” and “b”. From experiments we know that after reaction, the Q4 shows up as a 50 μm wide layer. However inserting a layer of 50 μm thick Q4 layer in the model would imply a fine spatial discretisation and consequently small time stepping that is numerically costly to solve. Furthermore, a 50 μm wide layer is below the REV scale of the system. We thus approximated the zone by an additional 1 mm thick strontium sulfate layer between the Q1 and Q2 regions with a porosity of 0.1. To maintain the total amount of strontium sulfate in the tank constant, the additional amount of strontium sulfate in this layer was compensated by lowering the amount of strontium sulfate in region Q2 which induces small changes in porosity and associated transport parameters (Table 1). The permeability of the additional 1 mm layer is 2×10^{-14} m^2. This model also included the two strontium sulfate particle sizes (Cls 1 and Cls 2 previously described in scenario 1) for region Q2. However, the Q4 region was assumed to be composed only of the small grained strontium sulfate crystals (Cls 1).

Comparison of the two model results:

In scenario 1, Cls 2 (large strontium sulfate crystals) remained almost undissolved and barium sulfate, following Cls 1 (small strontium sulfate crystals) dissolution, precipitated all across the reactive medium. This model precipitates barium sulfate all across the reactive medium (Fig. 8) which is in agreement with the experimental observations. The experimentally determined bulk amounts of minerals transformed with time were also successfully reproduced as seen in Fig. 9.

However, in scenario 1 complete clogging of the pore space is not possible, because the replacement of the entire strontium sulfate with barium sulfate would decrease the porosity only from 0.33 to 0.25. This is, because the dissolution of strontium sulfate followed by the precipitation of barium sulfate induces only a relatively small volume increase in the mineral phase volume (5.85 mL per mole of strontium sulfate reacted). In addition, the experimentally observed barium enriched zone at the interface and also the observed net pressure increase were not reproduced.

Again, as in scenario 1, in scenario 2 the experimentally determined bulk amounts of minerals transformed with time were also successfully reproduced. In this scenario, the barium enrichment zone was also reproduced as shown in Fig. 10. The formation of the barium enrichment zone was triggered by the presence of an initially larger amount of fast dissolving strontium sulfate at the interface (Q4 region). In this layer a more pronounced relative change of porosity occurs, because the initial porosity is lower. The observed relative pressure increase could be reproduced and is shown in Fig. 11.

A discrepancy between the model and the experimental results exists at around 190 h. After 190 h, the experimental net pressure increase starts to fall. This can be explained by the formation of micro-cracks in the strontium sulfate reactive medium which is not included in our model. In this scenario, the barium enrichment layer and clogging were triggered by introducing a zone of low porosity initially at the interface.

4. Summary and conclusions

Simple 2D reactive transport experiments were designed and conducted to investigate the complex interaction between liquid flows, solute transport, precipitation/dissolution reactions causing porosity changes and associated changes in material transport properties. Porosity changes in a reactive layer are triggered by the replacement of strontium sulfate ($SrSO_4$) with barium sulfate ($BrSO_4$) due to the ingress of a barium chloride solution. Barium sulfate precipitated as a nanocrystalline phase filling partly the pore space and cementing larger strontium sulfate crystals. The experiments can be used to test reactive transport models. Tracer tests, with non-reactive tracers performed prior to barium chloride injection, as well as changes in the flow field due to injection of a non-reactive liquid with different (higher) liquid density, were well reproduced by simulations with the transport code OpenGeoSys-GEM.

As shown by Tartakowsky et al. (2008) the use of the ADE in the presented numerical model is not completely appropriate for describing very strong local concentration gradients and localised precipitation. However, in contrast to Tartakowsky et al. (2008) concentration gradients and mineral precipitation are not completely controlled by dispersive mixing of solutes, as concentration gradients are also heavily influenced by the kinetic control of the dissolving mineral phase. Slow mineral dissolution will suppress strong concentration gradients and localised precipitation.

A connected problem is the choice of dispersion length used in the numerical model. A fixed value for the dispersion length, slightly higher than the grain size of the porous medium, was used. Such an approach is controversially discussed in literature (e.g., Hadley and Newell, 2014). Newer experiments on the role of dispersion in reactive systems indicate that effective molecular diffusion and ionic interactions between charged species are important (Cirpka et al, 2006; Muniruzzaman et al., 2014). The experimental setup offers some potential to test newer concepts of reactive transport.

For the successful reproduction of reactive transport experiments additional experimental data on the microstructure of the reactive medium were necessary. Only a model that included two populations of strontium sulfate grains with different dissolution kinetics successfully reproduced the experimentally observed evolution of the bulk amounts of minerals with time. Still this model did not match the measured pressure evolution, without changing the default parameters in the porosity–permeability relationship to extreme values. In the experiments, we observed an additional cemented zone at the interface between the sand and the reactive layer. We were not able to measure the initial and final porosity and transport properties of this layer, as we were unable to extract undisturbed samples of the reactive medium. Therefore we inserted an additional 1 mm thick layer at the interface with the same porosity–permeability relation as the reactive layer and modified the initial porosity in order to get a reasonable match to the experimental pressure evolution. It is possible to use an additional layer of other thickness and get a similar match of pressure evolution, if the initial porosity is adjusted accordingly.

We would like to stress, that without detailed knowledge of micro-structural changes it is not possible to reproduce all aspects of the system. Already in this “simple” system setup, micro-features below the continuum scale exist and need to be approximated in the model, e.g., the existence of an additional thin reactive layer with different transport properties.

In our current experimental setup, the reactions are limited by dissolution kinetics of strontium sulfate. At lower concentrations of barium chloride and in a more diffusive transport regime, dissolution of strontium sulfate might be limited by the transport process. Even with lower barium chloride injection, the formation of solid solution cannot be excluded. It needs to be tested, if the presented models also work for such a system.

As part of a multi-scale investigation, these experiments should also be approached by pore scale modelling. Further investigations including μ-XRD and μ-X ray tomography could be carried out to gain more insight on the nature of the newly formed barite precipitates and its physical transport properties. Such detailed experimental investigation can be combined with numerical investigations of mineral precipitation and dissolution at pore scale.

Acknowledgments

We gratefully acknowledge Nagra for funding this research. We also thank Dr. E. Curti for useful discussion, S. Frick for ion chromatography measurements and Dr. M. Bradbury for English correction.

Appendix A

Table 4
Thermodynamic database of aqueous, gaseous and solid species present under standards conditions.

Phase	component	Standard Gibbs energy of formation $\Delta G^0{}_f$ [KJ mol^{-1}]	Molar volume [10^{-5} m^3 mol^{-1}] under standard conditions
Aqueous	$Ba(CO_3)$	−1104.251	−1.1798542
	$Ba(HCO_3)^+$	−1153.325	1.917225
	$Ba(SO_4)$	−1320.652	0.818138
	Ba^{+2}	−560.782	−1.2901389
	$BaOH^+$	−721.077	0.91585235
	$Sr(CO_3)$	−1107.830	−1.5228401
	$Sr(HCO_3)^+$	−1157.538	1.4082323
	$Sr(SO_4)$	−1321.366	0.50248447
	Sr^{+2}	−563.836	−1.7757955
	$SrOH^+$	−725.159	0.70988636
	CO_2	−386.015	3.2806681
	CO_3^{-2}	−527.982	−0.60577246
	HCO_3^-	−586.940	2.4210897
	Cl^-	−131.290	1.7340894
	H_2	17.729	2.5264358
	O_2	16.446	3.0500889
	HSO_4^-	−755.805	3.484117
	SO_4^{-2}	−744.459	1.2917656
	OH^-	−157.27	−0.470784
	H^+	0.00	0.00
	H_2O	−237.18138	1.807
Gaseous	CO_2	−394.393	2478.9712
	H_2	0.00	2478.9712
	O_2	0.00	2478.9712
Solid	$Ba(CO_3)$	−1137.634	5.03
	$BaCl_2$	−810.400	5.40
	$BaCl_2 \cdot 2H_2O$	−1296.320	8.186
	$BaCl_2 \cdot H_2O$	−1055.630	7.208
	$Ba(SO_4)$	−1362.152	5.21
	Quartz	−854.793	2.2688
	$Sr(CO_3)$	−1144.735	3.901
	$SrCl_2$	−781.10	5.194
	$SrCl_2 \cdot 2H_2O$	−1281.6798	7.283
	$SrCl_2 \cdot 6H_2O$	−2240.8033	13.814
	$Sr(SO_4)$	−1346.15	4.625

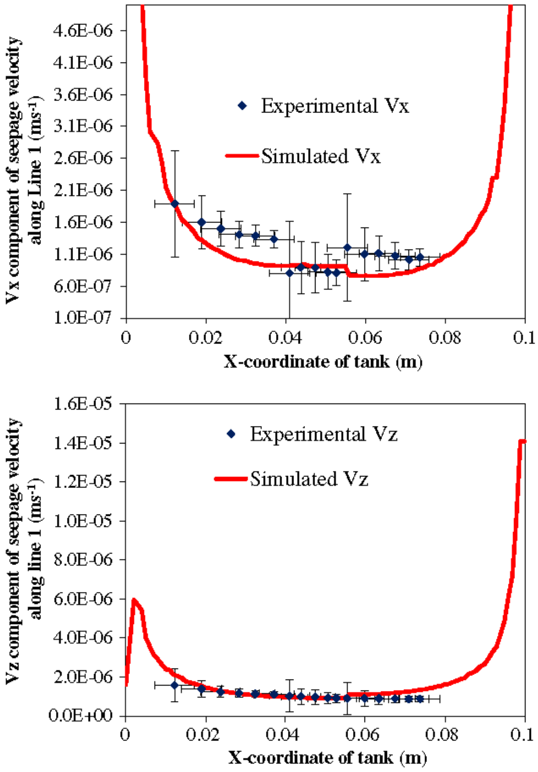

Fig. 12. Seepage velocity (m s^{-1}) components Vz and Vx along line 1.

Table 5
Elemental weight of the different elements present.

Element	Barium	Carbon	Chlorine	Hydrogen	Oxygen	Sulfur	Silicon	Strontium
Molar weight (g mol^{-1})	137.328	12.0108	35.453	1.00795	15.9994	32.067	28.0855	87.62

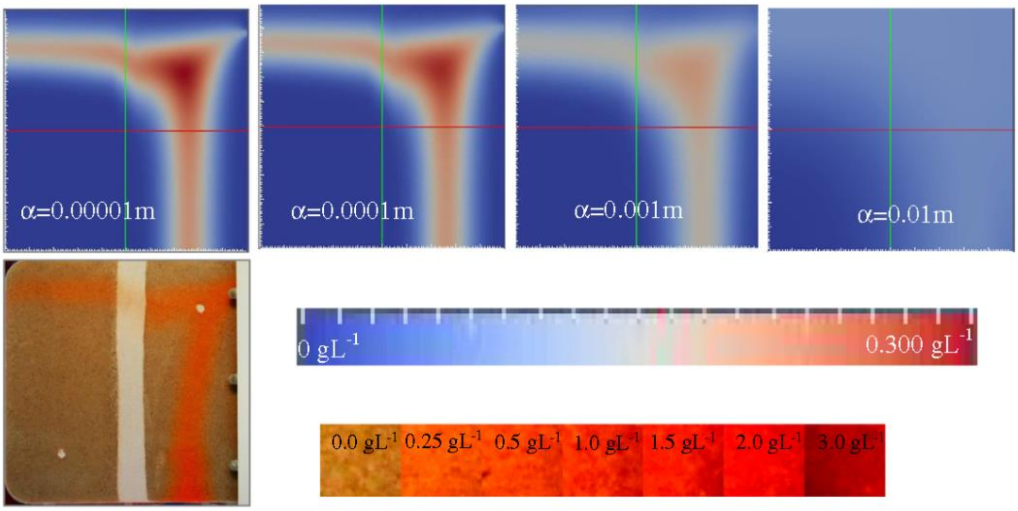

Fig. 13. Sensitivity analysis for testing different dispersive length for experiment 1. Qualitative comparison of simulation for different dispersive length (α = 0.01 m, α = 0.001 m, α = 0.0001 m, α = 0.00001 m).

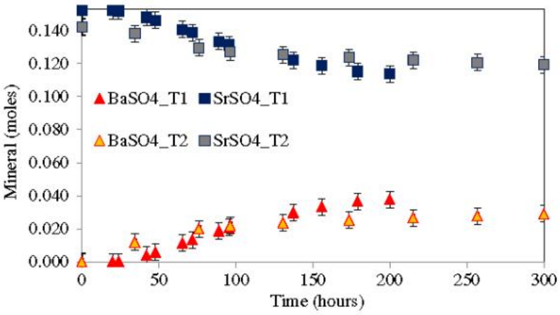

Fig. 14. Temporal mineral evolution of in two different tanks to test reproducibility of experiment 3. Also no further dissolution of strontium sulfate is seen after 150 h of barium chloride injection.

References

Archie, G., 1942. The electrical resistivity log as an aid in determining some reservoir characteristics. Pet. Trans. AIME 146, 54–62.

Bear, J., 1972. Dynamics of Fluids in Porous Media. Dover Publication Inc., New York.

Bear, J., Bachmat, Y., 1990. Introduction to modelling of transport phenomena in porous media. Springer, Berlin.

Bokern, D.G., Hunter, K.A., McGrath, K.M., 2003. Charged barite–aqueous solution interface: surface potential and atomically resolved visualization. Langmuir 19, 10019–10027.

Boving, T.B., Grathwohl, P., 2001. Tracer diffusion coefficients in sedimentary rocks: correlation to porosity and hydraulic conductivity. J. Contam. Hydrol. 53, 85–100.

Carman, P.C., 1937. Fluid through granular beds. Trans. Inst. Chem. Eng. 15, 150–166.

Chasset, C., Jarsjo, J., Erlstroem, M., Cvetkovic, V., Destouni, G., 2011. Scenario simulations of CO_2 injection feasibility, plume migration and storage in saline aquifer, Scania, Sweden. Int. J. Greenh. Gas Control 5, 1303–1318.

Cirpka, O.A., Olsson, A., Ju, Q., Rahman, M.A., Grathwohl, P., 2006. Determination of transverse dispersion coefficients from reactive plume lengths. Groundwater 44, 212–221.

Cochepin, B., Bildstein, O., Steefel, C., Lagneau, V., Van der Lee, J., 2008. Approaches to modelling coupled flow and reaction in a 2D cementation experiment. Adv. Water Resour. 31, 1540–1551.

Dauzeres, A., Le Bescop, P., Sardini, P., Cau Dit Coumes, C., 2010. Physico-chemical investigation of clayey/cement-based materials interaction in the context of geological waste disposal: experimental approach and results. Cem. Concr. Res. 40, 1327–1340.

De Windt, L., Pellegrini, D., Van der Lee, J., 2004. Coupled modeling of cement/claystone interactions and radionuclide migration. J. Contam. Hydrol. 68, 165–182.

De Windt, L., Badredinne, R., Lagneau, V., 2007. Long-term reactive transport modelling of stabilized/solidified waste: from dynamic leaching tests to disposal scenarios. J. Hazard. Mater. 207, 529–536.

Dove, P., Czank, C., 2005. Crystal chemical controls on the dissolution kinetics of the isosstuctural sulfates; celestite, anglesite and barite. Geochim. Cosmochim. Acta 56, 4147–4156.

Emmanuel, S., Berkowitz, B., 2005. Mixing-induced precipitation and porosity evolution in porous media. Adv. Water Resour. 28, 337–344.

Gaboreau, S., Lerouge, C., Dewonck, S., Linard, Y., Bourbon, X., Fialips, C., et al., 2012. In-situ interaction of cement paste and shocrete with claystones in deep disposal context. Am. J. Sci. 312, 314–356.

Gaucher, E.C., Blanc, P., 2006. Cement/clay interaction — a review: experiments, natural analogues, and modelling. Waste Manag. 26, 776–788.

Gautier, J., Oerlkers, E., Schott, E., 2001. Are quartz dissolution rates proportional to B.E.T. surface areas? Geochim. Cosmochim. Acta 65, 1059–1070.

Hadley, P.W., Newell, C., 2014. The new potential for understanding groundwater contaminant transport. Groundwater 52, 175–186.

Hayek, M., Kosakowski, G., Churakov, S., 2011. Exact analytical solutions for a diffusion problem coupled with precipitation–dissolution reaction and feedback of porosity change. Water Resour. 47, W07545. http://dx.doi.org/10.1029/2010WR010321.

Hayek, M., Kosakowski, G., Jakob, A., 2012. A class of analytical solutions for multidimensional species diffusive transport coupled with precipitation–dissolution reactions and porosity changes. Water Resour. 48, W03525. http://dx.doi.org/10.1029/2011WR011663.

Hummel, W., Berner, U., Curti, E., Pearson, F., Thoenen, T., 2002. Nagra/PSI Chemical Thermodynamic Data Base 01/01. Universal Publishers, Parkland/FLorida.

Jenni, A., Mäder, U., Lerouge, C., Gaboreau, S., Schwyn, B., 2014. In situ interaction between different concretes and opalinus clay. Phys. Chem. Earth Solid Earth A/B/C 70–71, 71–83.

Kanit, T., Forest, S., Galliet, I., Mounoury, V., Jeulin, D., 2003. Determination of the size of the representative volume element for random composites: statistical and numerical approach. Int. J. Solids Struct. 40 (36647-3679).

Kashiev, D., Van Rosmalen, G., 2003. Nucleation in solutions revisited. Cryst. Res. Technol. 38, 555–574.

Katz, G.E., Berkowitz, B., Guadagini, A., Marteen, W.S., 2011. Experimental and modeling investigation of multicomponent reactive transport in porous media. J. Contam. Hydrol. 27–44.

Kolditz, O., Bauer, S., 2004. A process-oriented approach to compute multi-field problems in porous media. J. Hydroinf. 6, 225–244.

Kosakowski, G., Berner, U., 2013. The evolution of clay rock/cement interfaces in a cementitious repository for low and intermediate level radioactive waste. Phys. Chem. Earth 64, 65–86.

Kosakowski, G., Wanatabe, N., 2013. OpenGeoSys-Gem: a numerical tool for calculating geochemical and porosity changes in saturated and partially saturated media. Phys. Chem. Earth 70–71. http://dx.doi.org/10.1016/j.pce.2013.11.008.

Kresic, N., 2006. Hydrology and Groundwater Modelling. Talor & Francis Group, CRC Press.

Kulik, D.A., Wagner, Y., Dmytrieva, S.V., Kosakowski, G., Hingerl, F.F., Chudnenko, K.V., et al., 2013. GEM-Selektor geochemical modeling package: revised algorithm and GEMS3K numerical kernel for coupled simulation codes. Comput. Geosci. 17, 1–24.

Lagneau, V., 2000. Influence des processus geochimiques sur le transport en milieu poreux. (PhD Thesis).

Lagneau, V., Pipart, A., Catalette, H., 2005. Reactive transport modelling of CO_2 sequestration in deep saline aquifers. Oil Gas Sci. Technol. Rev. IFP 60, 231–247.

Lichtner, P.C., 1992. Time–space continuum description of fluid–rock interaction in permeable media. Water Resour. Res. 28, 3135–3155.

Liu, J., Pereira, G.G., Regenauer-Lieb, K., 2014. From characterisation of pore-structures to simulations of pore-scale fluid flow and the upscaling of permeability using microtomography: a case study of heterogeneous carbonates. J. Geochem. Explor. 144, 86–96.

Luquot, L., Roetting, T.S., Carrera, J., 2014. Characterization of flow parameters and evidence of pore clogging during limestone dissolution experiments. Water Resour. Res. 6305–6321.

Marica, F., Jofre, S.A., Mayer, K.U., Balcom, B.J., Al, T.A., 2011. Determination of spatially-resolved porosity, tracer distributions and diffusion coefficients in poorous media using MRI measurements and numerical simulations. J. Contam. Hydrol. 125, 47–56.

Marty, N.C., Tournassat, C., Burmol, A., Giffaut, E., Gaucher, E., 2009. Influence of reaction kinetics and mesh refinement on the numerical modelling of concrete/clay interactions. J. Hydrol. 364, 58–72.

Mavko, G., Mukerji, T., Dvorkin, J., 2006. The Rock Physics Handbook. Cambridge University Press.

Muniruzzaman, M., Haberer, C.M., Grathwohl, P., Rolle, M., 2014. Multicomponent ionic dispersion during transport during of electrolystes in heterogeneous porous media. Experiments and model based interpretation. Geochim. Cosmochim. Acta 141, 659–669.

Ozgumus, T., Mobedi, M., Ozkol, U., 2014. Determination of Kozeny constant on porosity and pore to throat size ratio in porous medium with rectangular rods. Eng. Appl. Comput. Fluid Mech. 8, 308–318.

Palandri, J., Kharaka, Y., 2004. A Compilation of Rate Parameters of Water Mineral Interaction Kinetics for Application to Geochemical Modelling. U.S. Geological Survey, Menlo Park, California.

Prieto, M., Putnis, A., Fernandez-Diaz, L., 1993. Crystallization of solid solutions from aqueous solutions in a porous media: zoning in $(Ba,Sr)SO_4$. Geol. Mag. 289–299.

Rausch, R., Schaefer, W., Therrien, R., Wagner, C., 2005. Solute Transport Modelling. An Introduction to Models and Solution Strategies. Borntraeger Verlagsduchhandlung, Berlin Stuttgart.

Seifert, D., Engesgaard, P., 2012. Sand box experiments with bioclogging of porous media: hydraulic conductivity reductions. J. Contam. Hydrol. 136–137, 1–9.

Shao, H., Dmytrieva, S., Kolditz, O., Kulik, D., Pfingsten, D., Kosakowski, G., 2009. Modeling reactive transport in non-ideal aqueous–solid solution system. Appl. Geochem. 24 (7), 1287–1300.

Steefel, C.I., De Paolo, D.J., Lichtner, P.C., 2005. Reactive transport modeling: an essential tool and a new research approach for earth sciences. Earth Planet. Sci. Lett. 20, 539–558.

Tartakowsky, A.M., Redden, G., Lichtner, P.C., Scheibe, T.D., Meakin, P., 2008. Mixing-induced precipitation: experimental study and multiscale numerical analysis. Water Resour. Res. 44, 1–19.

Thullner, M., Mauclaire, L., Schroth, M., Kinzelbach, W., Zeyer, J., 2002. Interaction between water flow and spatial distribution of microbial growth in a two-dimensional flow field in saturated porous media. J. Contam. Hydrol. 58, 169–189.

Trotignon, L., Didot, A., Bildstein, O., Lagneau, V., Margerit, Y., 2005. Design of a 2D cementation experiment in porous medium using numerical simulation. Oil Gas Sci. Technol. Rev. IFP 60, 307–318.

Tyagi, M., Gimmi, T., Churakov, S., 2013. Multi-scale micro-structure generation strategy for upscaling transport in clays. Adv. Water Resour. 59, 181–195.

Van der Lee, J., 2003. Module oriented modeling of reactive transport with HYTEC. Comput. Geosci. 29, 265–275.

Van Loon, L.R., Müller, W., Glaus, M.A., 2007. Anion exclusion effects in compacted bentonites: towards a better understanding of anion diffusion. Appl. Geochem. 22, 2536–2552.

Wagner, T., Kulik, D.A., Hingerl, F.F., Dmytrieva, S.V., 2012. GEM-Selektor geochemical modeling package: TSolMod library and data interface for multicomponent phase models. Can. Mineral. 5, 1173–1195.

Xie, M., Wang, W., Jonge, J.D., Kolditz, O., 2007. Numerical modelling of swelling pressure in unsaturated expansive elasto-plastic porous media. Transp. Porous Media 66, 311–339.

Xu, T., Apps, J.A., Pruess, K., 2005. Mineral seqestration of carbondioxide in sandstone-schale system. Chem. Geol. 217, 295–318.

Zheng, C., Bennett, G.D., 1995. Applied Contaminant Transport Modeling: Theory and Practice. A division of International Thomson Publishing Inc., United States of America.

Chapter 3: Barite precipitation following celestite dissolution in a porous medium: a SEM/BSE and μ-XRD/XRF study

Abstract

A reaction cell experiment was designed to examine mineral dissolution/precipitation processes at the macroscopic and pore scale. A rectangular flow cell was filled with a reactive porous layer between two porous layers composed quartz of sand (SiO_2). The reactive layer consisted of celestite ($SrSO_4$) with a bimodal grain size distribution (< 63 µm and 125 - 400 µm). A barium chloride solution was then injected into the flow cell, leading to fast dissolution and replacement of celestite by barite ($BaSO_4$). Due to the larger molar volume of barite compared to celestite, the porosity decreased in the reactive layer. We concentrated on the refinement of post-mortem analysis and the investigation of the dissolution/precipitation mechanisms at the pore scale (10 - 100 μm). The sequential evolution of mineral transformations occurring in the reactive layer was determined. Our analytical techniques, combining scanning electron microscopy and synchrotron X-ray microdiffraction/microfluorescence, showed that the small celestite grain fraction dissolved rapidly to form nano-crystalline barite filling the pore space, while large celestite grains were covered with a thin rim of epitaxial micro-crystalline barite. Two distinct nucleation mechanisms for barite precipitation were involved: homogeneous nucleation (nucleation of barite in the pore space) and heterogeneous nucleation (nucleation on the surface of a solid substrate). Classical nucleation theory, using well-established and estimated (e.g. wetting angle) parameters describing barite precipitation, was applied to explain the mineralogical changes occurring in our system.

Keywords: nucleation mechanism, epitaxial barite.

Corresponding author: Jenna Poonoosamy
Paul Scherrer Institut
Tel: +41 563 10 2079
E-mail: jenna.poonoosamy@psi.ch

Highlights:

Celestite dissolution and barite precipitation in a porous medium were described in detail at the micrometre scale by combining advanced microscopic techniques.

Spatially resolved synchrotron micro-XRD data showed unequivocally epitaxial growth of barite on celestite and precipitation of nano-crystalline barite in the pores.

We successfully correlated our experimental observations with literature data on barite precipitation kinetics and classical nucleation theory.

Barite precipitation following celestite dissolution in a porous medium: a SEM/BSE and μ-XRD/XRF study

J. Poonoosamy[1], E. Curti[1], G. Kosakowski[1], D. Grolimund[2], L. R. Van Loon[1] and U. Mäder[3]

[1] Laboratory for Waste Management, Paul Scherrer Institut, CH-5232 Villigen PSI, Switzerland

[2] Swiss Light Source, Paul Scherrer Institut, CH-5232 Villigen PSI, Switzerland

[3] Rock Water Interaction, Institute of Geological Sciences, University of Bern, Baltzerstrasse 3, CH-3012 Bern, Switzerland

* Corresponding author: +41 563 10 2079
E-mail: jenna.poonoosamy@psi.ch

1. Introduction

Mineral precipitation and dissolution in porous media change pore space geometry and influences transport properties. These mineral-water interactions are important processes in mineral mining, geological sequestration of carbon dioxide, exploitation of geothermal heat, enhanced oil recovery and chemical weathering (Kang et al, 2003). Another example is the long term storage of nuclear waste in a deep geological repository where cementitious materials will be used for support structures, as cavern backfill or for waste conditioning. The diffusion of the cement pore water into the surrounding clay host rock and vice versa are expected to lead to the precipitation and dissolution of mineral phases near the clay-cement interface and might clog porosity (Dauzeres et al. 2010; Jenni et al., 2014) and thus reduce diffusive and advective transport across the interface.

The prediction of the evolution of the aforementioned systems by numerical tools requires comprehensive and robust kinetic data on mineral-water interaction (Schott et al. 2009). We designed a reactive transport experiment of sufficient complexity (Poonoosamy et al., 2015) to evaluate sulfate dissolution/precipitation processes in porous media at the pore scale and macro-scale and its impact on transport. To construct a pore scale model involving dissolution and precipitation reactions in porous media, it is important to understand fluid dynamics and solute transport at the micrometre scale, to identify the chemical nature of the newly formed phases (pure minerals or solid solutions) and their evolution as the reaction proceeds.

Sulfate minerals are of interest to many fields and have been widely studied in the past. Barite is one of the most common scale-forming minerals due to its low solubility product, $pK^0_{sp} = 9.97$ (Hummel et al., 2002). Barite scaling due to injection of seawater into oil reservoirs, done in order to enhance recovery and to extend field life, is among the most frequently encountered oil field problems (Fu et al., 2012; Oddo and Tomson, 1994). Similar scaling problems arise during exploitation of geothermal fluids for heat and electricity production. In geothermal reservoirs deposition of barite scales from ascending fluids is likely to occur in fractured zones due to a decrease of barite solubility on cooling (Mundhenk et al., 2013; Aquilina et al., 1997). Finally, in nuclear waste storage sites, barite is predicted to be the main scavenger of radium released from the waste due to formation of ($BaSO_4$-$RaSO_4$) solid solution (Curti et al., 2010; Brandt et al., 2015).

Barite and $BaSO_4$-$SrSO_4$ solid solution precipitation in porous media have been widely studied (Prieto et al., 1990; Prieto et al., 1993; Putnis et al., 1995; Sánchez-Pastor et al., 2005; Sánchez-Pastor et al., 2006). The formation of barite from supersaturation in heterogeneous porous media is a complex process that involves delayed nucleation and different growth mechanisms, e.g. direct precipitation from solution (homogeneous precipitation) and growth on a substrate (heterogeneous precipitation). The latter might cause the passivation of the substrate surface which will affect the reactivity of the substrate (Nicholson et al., 1990).

A major finding (Prieto, 2014) was that the threshold supersaturation, at which macroscopically visible barite precipitation starts, correlates with the pore size. Indeed, homogeneous nucleation of barite was found to require much higher supersaturation in media with small pores compared to media with larger pores. This phenomenon could be explained with the principles of classical nucleation theory (Kashchiev and van Rosmalen, 2003) and is in agreement with other studies (Putnis and Mauthe, 2001; Emmanuel and Berkowitz, 2007; Stack et al., 2014; Nindiyasari et al., 2014).

Our experiment involved the dissolution of a primary mineral, celestite ($SrSO_4$), induced by infiltration of a barium chloride solution followed by the precipitation of a secondary mineral, barite ($BaSO_4$). The replacement of celestite by barite was accompanied with changes in porosity and permeability that led to non-linear changes in the flow field. The experiment was modelled using a simple kinetic approach proposed by Poonoosamy et al. (2015) but was limited by not considering mechanisms at the pore scale.

Although celestite and barite are structurally isomorphous, they have different unit cell volumes of 305 $Å^3$ and 346 $Å^3$, respectively (Deer et al., 1992) differing by 12%. As a result, stoichiometric celestite replacement by barite reduces the average pore volume in the reactive zone, possibly leading to localized clogging and impervious pathways. Because a continuous series of solid solutions ($Ba_{1-x}Sr_xSO_4$) may be formed during the dissolution/precipitation process, the extent of porosity reduction will also depend on the mole fraction of Ba in the precipitated solid. Precipitation of pure barite will have a stronger effect on porosity and permeability than the formation of a solid solution. The chemical nature of the newly precipitated barite phase needs thus to be fully characterized in order to understand changes in fluid flow properties.

The general purpose of this analytical and interpretative work is i) to gain insight into the nature of the newly formed barite phase following celestite dissolution in our experiments, ii) to unravel mechanisms of fluid/solute transport and mineralogical changes on the microscopic scale as well as the temporal evolution of the system. We will use the equations and parameters described in Kashchiev and van Rosmalen (2003) and Prieto (2014) to explain and understand mineralogical changes occurring in our system in terms of classical nucleation theory.

2. Experimental Methods

2.1. Setup of reactive transport experiments (including fluid chemistry)

A detailed description of the experimental set up is given in Poonoosamy et al. (2015). A Plexiglas (tank) containment of internal dimension 10 cm × 10 cm × 1 cm was filled with granular solids consisting of a celestite layer sandwiched between two layers of quartz sand (Fig.

1). Polished celestite gemstones from Madagascar were washed with ethanol, crushed and sieved to batches of different grain sizes. The celestite was analysed by conventional X-ray diffraction (XRD) which revealed only a weak contamination with 0.3% of anhydrous calcium sulfate. The celestite layer in the tank consisted of a mixture of two different grain size fractions: 30 wt. % with a size of less than 63 µm and ~ 70 wt. % with a size of 125 - 400 µm.

The quartz-celestite mixture was initially permeated by injecting a solution saturated with respect to strontium sulfate (to prevent the dissolution of celestite). Prior to the injection of 0.3 M barium chloride at a constant rate of 20 µL min^{-1}, 10 mL of MilliQ® water were pumped through the inlet (the pore volume of the system being approximately 40 mL). This prevented a reaction between pore water in the quartz medium and the incoming barium chloride solution, by pushing all dissolved sulfate downstream towards the extraction hole. As the barium chloride front reached the celestite region, precipitation of barite was expected, driven by sulfate supplied via dissolution of celestite. Due to the higher molar volume of barite, its precipitation caused a porosity decrease in the reactive layer. Dyes tracer tests were performed before and after barium chloride injection to reveal changes in the flow field that can be ascribed to local porosity and permeability changes. Post mortem microscopic analysis of the reactive medium was carried out to identify the reaction products and pore space changes.

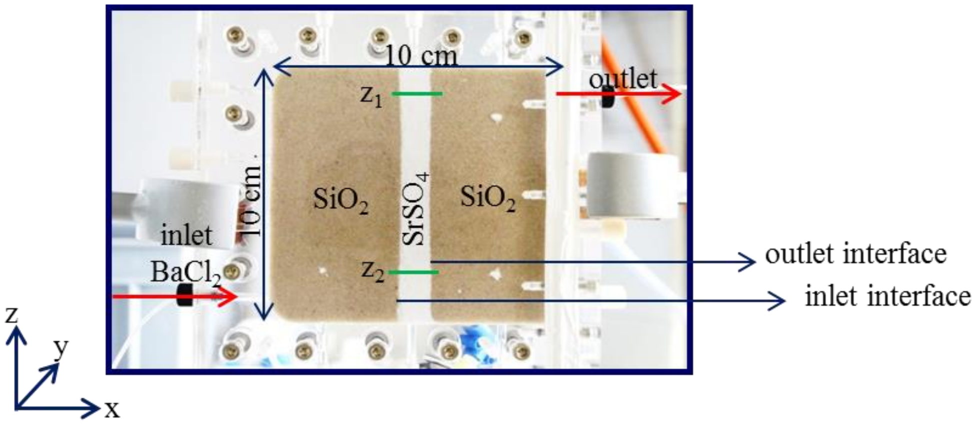

Fig. 1: Plexiglas tank with inner dimensions of 10 × 10 × 1 cm filled with a reactive medium of celestite ($SrSO_4$) in between two layers of inert porous media, quartz (SiO_2). z_1 and z_2 are locations where sampling of the reactive media.

To determine the structural changes of the pore space and how porosity clogging was triggered, the aforementioned experiment was repeated five times and interrupted at different barium chloride injection times of 9, 28, 156, 200 and 300 hours. The experiments were labelled 1 to 5 in order of increasing injection time. At the end of each experiment the pore solution in the tank was pumped out from the inlet and isopropanol was injected into the tank from the outlet in order to stop the chemical reaction.

The reacted celestite strips from experiments 1 and 2 (9 and 28 hours injection time, respectively) were still fragile and uncemented while those from experiments 3, 4 and 5 (156, 200 and 300 hours injection time respectively) seemed to be cemented and formed rectangular blocks. The Plexiglas tanks were carefully disassembled. Because the reacted celestite strips from experiments 1 and 2 were mechanically unstable, they were gently cut into 1 cm pieces (along the z-axis). All reacted celestite segments were dried in silicone moulds and those from experiment 1, 2, 3 and 4 were then impregnated with araldite XW396/XW397 resin under vacuum. The well-cemented solid from experiment 5 was not impregnated with resin in order to allow the identification of fine grained phases by using an optical microscope. Standard petrographic thin sections (~ 20 µm thick) of the reacted interface were prepared on a 1 mm thick glass support without cover glass after impregnation with resin.

2.2. Analytical techniques (optical microscope/SEM/BSE/EDX)

The microscopic structure of the reacted celestite was investigated by optical and scanning electron microscopy (SEM). Thin sections parallel to the x-y plane from regions of the reactive media between z = 2 cm and z = 3 cm were investigated for all the experiments (1 to 5) in order to get structural and mineralogical information on the temporal evolution of the newly formed phases. A thin section at z = 9 cm from experiment 1 was also made. As reported in Poonoosamy et al. (2015), dye tests showed that due to the higher density of the 0.3 M barium chloride solution compared to the initially injected Milli-Q® water, the solute initially accumulates at the bottom of the tank and is then slowly transported towards the top. After 9 hours of injection the reactive solution reached only half height of the tank while the upper part still remained unreacted. The thin section collected at z = 9 cm can thus be considered as a control sample close to the pristine celestite medium. The thin sections were first examined with an optical microscope to distinguish the different phases present. The uncoated thin section surface was then examined by SEM with a beam acceleration of 20 kV. Our SEM analyses were coupled with Energy Dispersive X-ray fluorescence analyses (EDX) to obtain semi-quantitative elemental analyses. Back-Scattered Electron (BSE) images were also taken, giving important information on the spatial distribution of the elements and phases present after reaction.

2.3 Micro XRF and micro XRD measurement and data analysis

Synchrotron-based Micro-X Ray Fluorescence (µ-XRF) and Micro-X Ray Diffraction (µ-XRD) techniques were used to identify crystalline phases and their spatial distribution at micrometric resolution. To this aim, selected areas of the investigated thin section (of the sample from experiment 5 at z = 3 cm) were scanned with an intense micro focused X-ray beam at a photon energy of 17.04 keV. This is appropriate to obtain maps of both Ba-L_α and Sr-K_α fluorescence signals, using a single element Si drift diode (SDD) detector (Ketek GmbH) to collect the fluorescence signal. Although beam sizes of less than 1 µm x 1 µm were achievable, a slightly defocused beam of 5 µm x 5 µm was preferred in consideration of the huge amount of data that would be produced to scan a sufficiently large area. Simultaneously, a diffraction pattern was recorded at each pixel of the scanned sample area with a PILATUS 100K area detector (DECTRIS, Ltd), allowing identification of crystalline phases complementary to µ-XRF at fast data collection rates and at spatial resolutions of few micrometres.

In our experiments, the main interest was to correlate the XRD data with the fully preserved spatial relationships in the reacted sample. In this way, a full diffraction pattern can be associated to each single pixel mapped by XRF. In this type of experiment, we see generally less reflections for a single diffraction image than in a powder sample due to the small volume probed by the beam and the lack of sample or detector rotation. Nevertheless, powder XRD-like data can be obtained by integrating the patterns over the entire or a partial sample region. All µ-XRD/ µ-XRF measurements presented here were performed at the microXAS beamline (Swiss Light Source, Villigen, Switzerland) using the XRDUA software (De Nolf et al., 2014) for data analysis.

3. Results

3.1. Microscopic analysis

3.1.1. Optical microscopy

Fig. 2 gives an overview of the celestite zone after reaction with the barium chloride solution (300 hours after injection). Two distinct phases can be distinguished: the original large celestite crystals and a brownish phase partially filling the pore space, which appears extinct under crossed polars, i.e. it is optically isotropic, as shown in Fig. 2. This phase might therefore be amorphous, nano-crystalline or cubic and will be referred as “fine grained precipitate” hereafter.

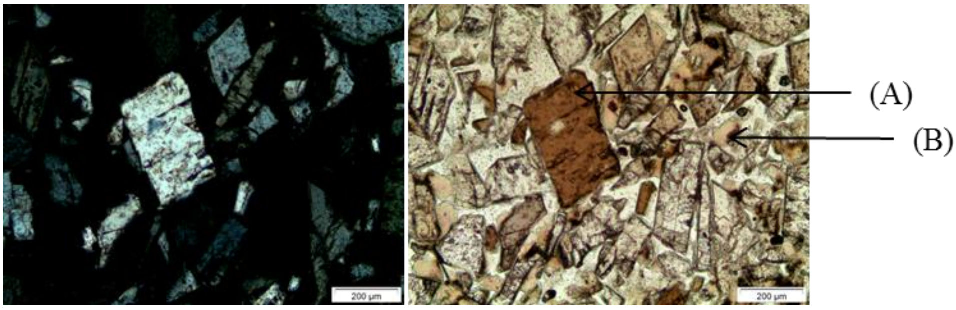

Fig. 2: Optical microscope images of the reacted celestite after 300 hours of barium chloride injection under polarized light (left image) and non-polarized light (right image). Larger celestite grains (A) can be distinguished. A newly formed phase (B), characterized by total extinction in polarized light, partially fills the pore space.

3.1.2. Scanning electron microscopy (SEM)

The samples collected from the different experiments show the sequential evolution of the newly formed barite phases.

As shown in Fig. 3a, initially (at time t = 0 hours) the reactive medium is composed of celestite grains with a bimodal size distribution. Black regions correspond to open spaces representing the original porosity of the sample, preserved by the resin impregnation procedure. However, we cannot rule out minor artefacts arising from the thin section preparation. Some crystals might have been ripped off during the polishing process. The large open spaces were probably the main channels for fluid transport.

After 9 hours of barium chloride injection, small amounts of a newly formed phase (indicated by the ellipses in Fig. 3b) appear in the interspaces between the smaller celestite crystals. This phase probably corresponds to the brownish fine-grained precipitate observed with the optical microscope. In some cases it forms half-circles delimiting empty spaces (black circular holes). These structures possibly correspond to locations of fast-flowing $BaCl_2$-rich solution, from which the fine-grained compound precipitated forming tunnel-like walls around the flowing solution. The elemental composition of the fine-grained phase was obtained by coupling the SEM measurement with EDX spot analyses.

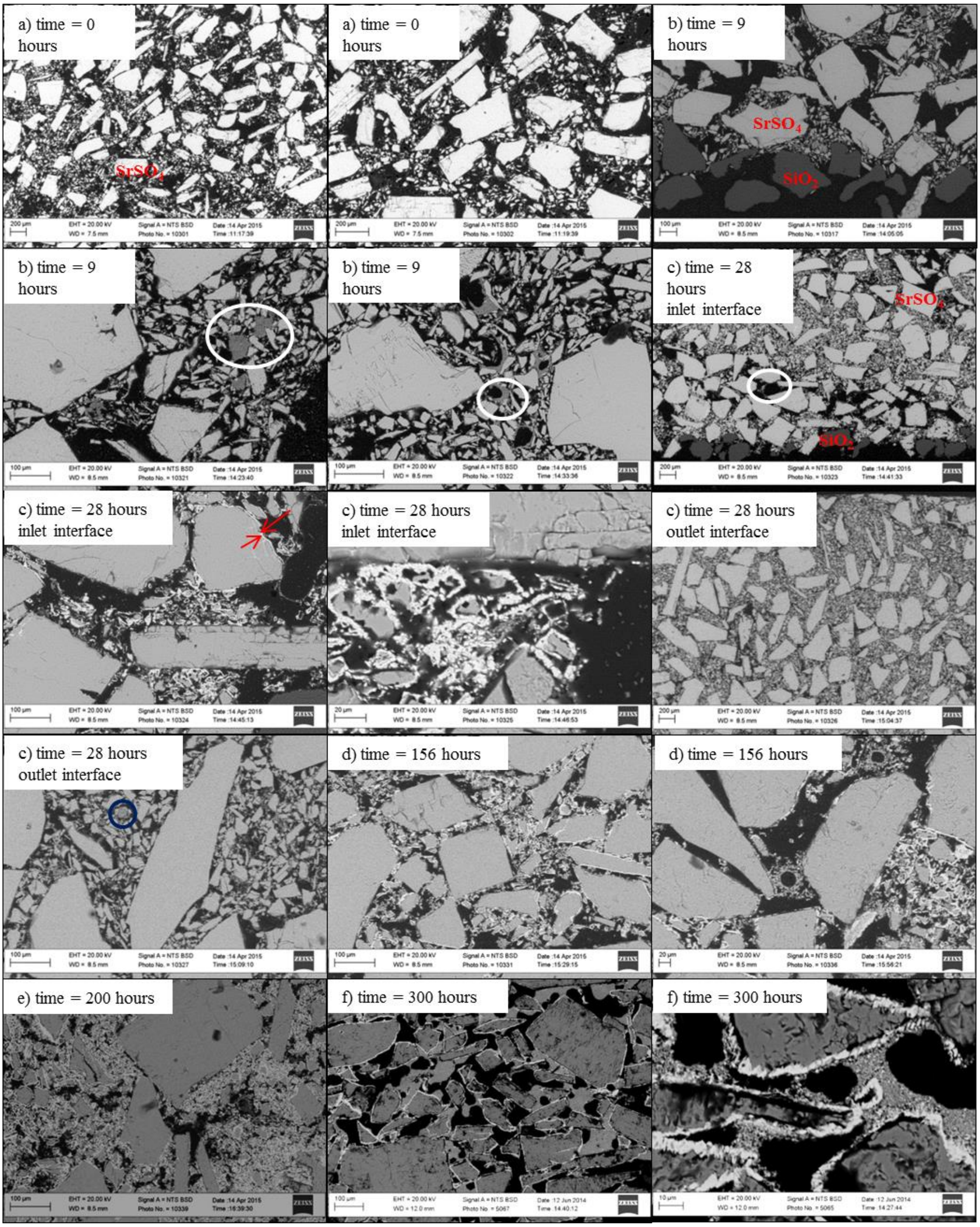

Fig. 3: SEM images showing microstructural relations in the celestite reactive layer: a) Bimodal celestite distribution of the pristine reactive layer. b) The reactive layer after 9 hours of $BaCl_2$ injection, showing incipient formation of nanometre-sized fine-grained precipitate preferentially around circular “holes”. Close to the upstream quartz-celestite interface the fine-grained precipitate fills the interstitial spaces. c) First appearance of a thin epitaxial rim (probably barite) growing on a large celestite crystal, as well as an infill of the same compound in a fractured

crystal in the reactive interface. The fine-grained precipitate actually consists of a mixture of bright and darker spots. The bright spots probably correspond to newly formed barite, whereas the dark spots are probably residues of the small dissolved celestite crystals. In the downstream quartz-celestite interface, only fine-grained precipitate can be observed. d) After 156 hours the epitaxial rim is ubiquitous. e) After 200 hours, fine-grained filling and epitaxial rim are pervasive. f) The reactive medium after 300 hours.

Fig. 4 gives two characteristic EDX spectra of the fine grained precipitate (after 28 hours of reaction) taken in the upstream and downstream celestite-quartz interfaces, indicating that it consists of Ba, Sr and S in variable proportions. At the inlet interface, the barium concentration was higher than at the outlet interface. Because the grain size of the precipitate is considerably smaller than the probed volume, the EDX analyses cannot be interpreted to represent single mineral compositions.

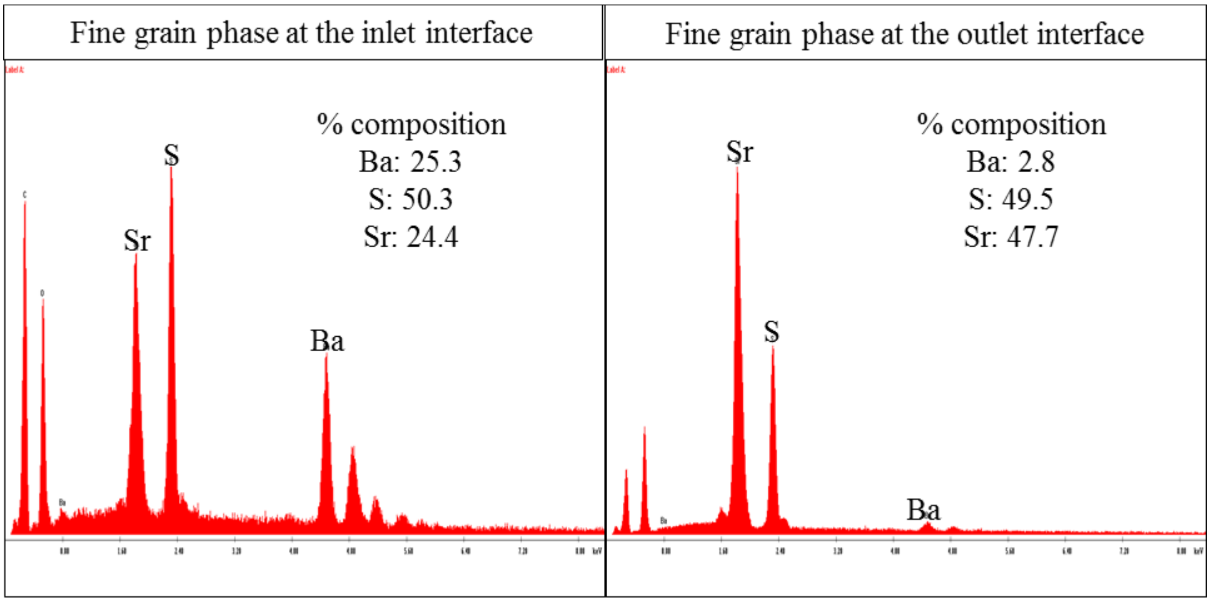

Fig. 4: The elemental composition of the fined grain phase formed at the upstream (inlet) and downstream (outlet) interface. (The percentage composition for each element is given in the picture).

After 28 hours of barium chloride injection (Fig. 3c), thin overgrowths formed around several celestite grains. They are most probably Ba-rich, as indicated by the bright colour in the BSE images, and appear at the celestite-quartz interface closer to the inlet. A bright overgrowth also occurs in some micro-fissures within large celestite grains. Further away from the inlet, no such rims can be seen at this injection time.

After 156 hours of barium chloride injection and onwards, all large celestite crystals are covered with brighter rims and the fine grained precipitate progressively fills the pore space (clogging). After 300 hours, the Ba-rich overgrowth on large celestite crystals is pervasive (Fig. 3f).

3.2. µ-XRF measurements

Fig. 5 shows elemental maps of Ba (left) and Sr (right) obtained by collecting the X-ray fluorescence signals over the same sample area, compared to the optical microscope image. The sample analysed in Fig. 5 was collected from experiment 5 (i.e. barium chloride injection was interrupted after 300 hours) at position z = 3 cm. The XRF data confirm the BSE images and show an accumulation of Ba in the interstitial spaces between the large primary celestite grains (indicated by the arrows in Fig. 5a and 5b). All the large celestite crystals show a barium-rich overgrowth.

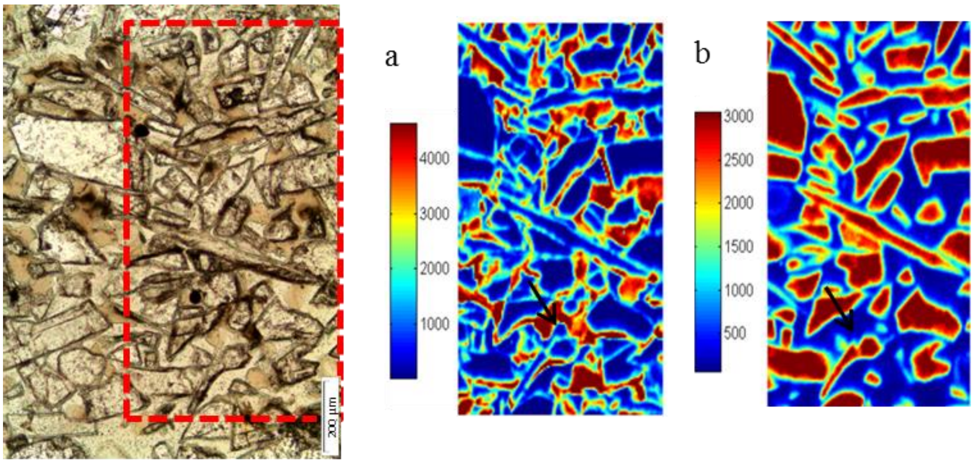

Fig. 5: The optical microscopic view (right) of the reactive media after 300 hours of barium chloride injection and the corresponding elemental mapping (right side) using µ-XRF techniques with (a) corresponding to barium signals and (b) to strontium signals.

3.3. µ-XRD measurements

Fig. 6 shows a map of X-ray diffraction intensities arising from reflections at a d-spacing of 3.1 Å. This corresponds to the most intense reflection (211) of pure barite at d = 3.11 Å and can be distinguished from the corresponding celestite reflection at d = 2.97 Å. The images on the right side of Fig. 6 are micro-diffraction patterns obtained from few pixels (superimposed images) at the locations in the map indicated by the origin of the arrows. They represent the 3 previously identified distinct phases, i.e. pristine celestite (a), a rim precipitate overgrown on celestite crystals (b) and fine-grained interstitial precipitate (c). The probed volume at each single pixel is about 5 µm x 5 µm x 30 µm. The pattern from the interior of a large celestite crystal (given in Fig. 6a) produces as expected spot-like reflections assigned to pure celestite (e.g. plane (211)). Spot-like reflections are characteristic of well-developed single crystals or crystal aggregates with a strong preferred orientation. Spot-like reflections are also visible in the XRD pattern collected at the barium-rich interfaces in contact with the large celestite crystals (Fig. 6b). However, they are typically "doubled" as pairs characterized by small differences in 2 theta angles (consistent with pure barite and pure celestite reflections) and by identical azimuthal angles. The identical azimuthal angles imply that the barite reflections arise from crystallographic planes with the same orientation as the celestite substrate, i.e. it is a signature for epitaxial growth of barite on celestite. In contrast to Fig. 6a and 6b, the fine-grained phase filling the interstices is dominated by continuous diffuse Debye rings corresponding to pure barite reflections (Fig. 6c). The appearance of Debye rings from XRD patterns integrated over a sample volume of few μm^3 is a clear proof that the "extinct phase" interstitial precipitate is in reality nano-crystalline, i.e. composed of randomly oriented nanometre barite particles.

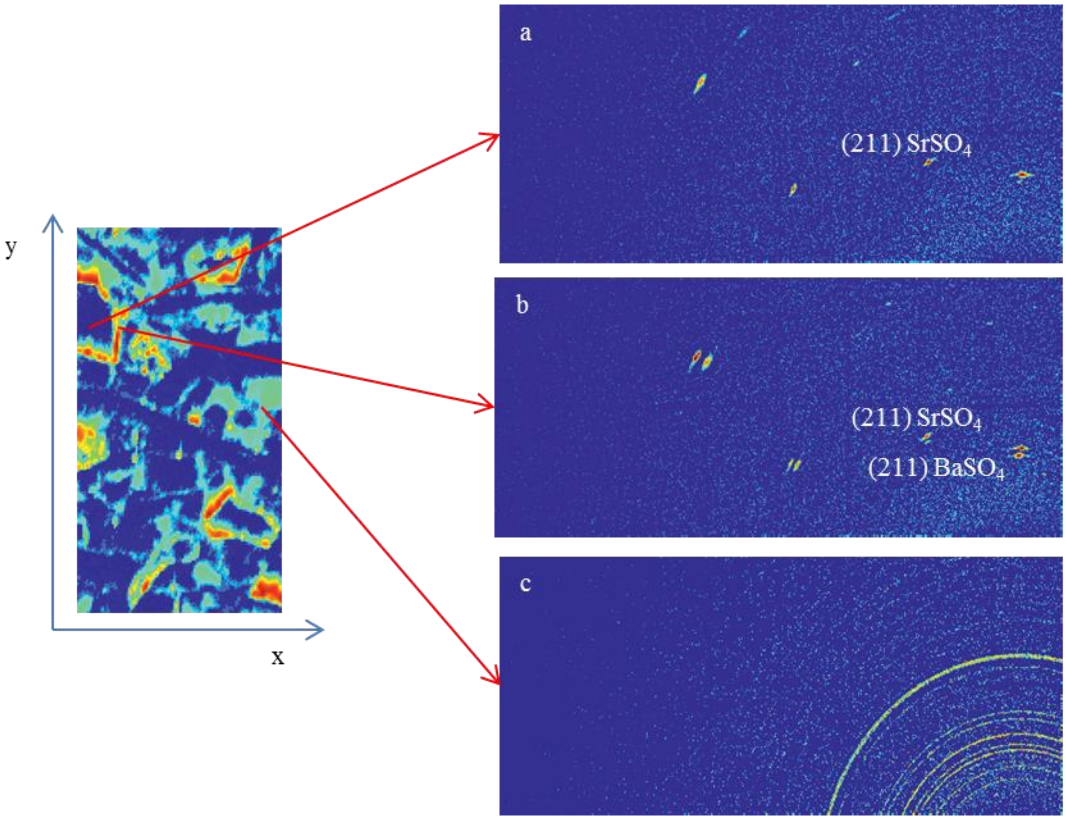

Fig. 6: XRD diffraction intensity map for d = 3.1Å, corresponding to the (211) barite reflection, correlated with 3 different XRD patterns from the indicated map locations (a) interior of a large celestite crystal, (b) micro-crystalline epitaxial barite at the surface of large celestite crystal and (c) nano crystalline phase filling the interstices). Intensities increase in the sequence blue < cyan < green < yellow < red.

In contrast to the patterns of Fig. 6, Fig. 7 gives XRD images integrated over the entire mapped area. Only diffraction patterns corresponding to selected ranges of Ba and Sr fluorescence intensities are integrated. Fig. 7a shows the area-integrated diffraction pattern arising from high Ba intensities and corresponds to the deep red regions in Fig. 5a. As in Fig. 6c, the averaged diffraction pattern is dominated by Debye rings corresponding to pure barite reflections (indexed in blue). In addition, several spots appear which correspond to celestite reflections (indexed in green). Probably, these reflections are due to residues of primary celestite which remained undissolved. Therefore, this diffraction pattern identifies nano-crystalline barite (rings) intermixed with relics of primary celestite (spots). We can rule out that the spot reflections originate from the large primary crystals because care was taken to select only locations far away from such crystals (through the definition of fluorescence intensity interval from which the diffraction patterns are picked up).

The averaged diffraction pattern corresponding to the integration of XRD patterns associated high Sr signals (red regions in Fig. 5b) is given in Fig. 7b. Except for a single weak spot assigned to barite (blue ring corresponding to the (211) reflection), as expected all other Debye rings match celestite reflections.

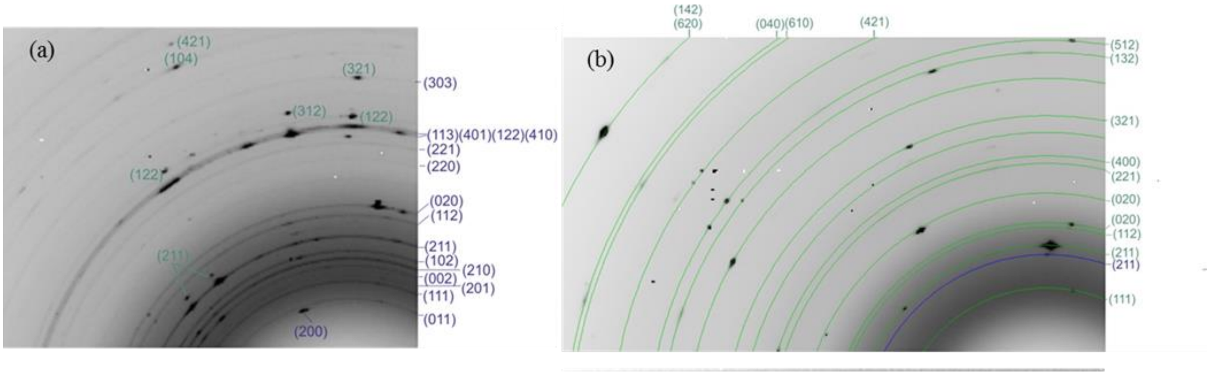

Fig. 7: (a) is the averaged pattern from all XRD patterns obtained from high Ba regions (pixels with intensities > 3800 counts in Fig. 5a). This corresponds to all red spots, surely with no interaction with the large primary celestite crystals. (b) Is the averaged image from all XRD patterns obtained from high Sr regions (pixels with intensities > 3800 counts in Fig. 5b). This integration selects only regions corresponding to the cores of primary celestite crystals.

In summary, all reflections in the XRD patterns of Fig. 6 and Fig. 7 are consistent with d-spacings assigned either to pure barite or to pure celestite. The fine-grained aggregate previously identified with the optical and SEM microscope can thus be identified as consisting of pure barite nanocrystals intermixed with residues of primary celestite. It is also worth noting that the formation of barite solid solutions with a significant mole fraction of Sr can be excluded, since no noticeable displacements of the pure barite (221) and (210) reflections can be found (Ceccarello et al., 2004).

4. Interpretation

4.1. Thermodynamic and kinetic considerations

The Lippmann diagram for the barite-celestite binary shown in Fig. 8a was constructed using the solubility products $K^0_{sp}(BaSO_4) = 10^{-9.97}$ and $K^0_{sp}(SrSO_4) = 10^{-6.63}$, taken from Hummel et al. (2002), and assuming a subregular mixing model with interaction coefficients $W_{12} = 3665$ J mol^{-1} and $W_{21} = 3787$ J mol^{-1} (Zhu, 2004). The large difference in the solubility products of the two end-members implies that the composition of a fully equilibrated solid solution will be strongly enriched in the less soluble component ($BaSO_4$), even in Sr-rich aqueous solutions. For example, an aqueous solution with a Sr/Ba ratio of 2.33 ($X_{Sr,aq} = 0.7$) would be in equilibrium with barite containing only a few tens of ppm Sr (Fig. 8b). In our experiments, a relatively high concentrated $BaCl_2$ solution is injected and transported advectively, implying very low Sr/Ba ratios in the reactive medium at any time and any location. Therefore, equilibrium thermodynamics would predict, in agreement with the observations, precipitation of pure barite during our experiments.

However, equilibrium thermodynamics is not always appropriate to describe the phenomenology of sulfate mineral precipitation in short-term experiments. There is ample evidence that non-equilibrium precipitation is common in highly supersaturated solutions (Prieto et al., 1993; Pina et al., 2000). In general, homogeneous precipitation of Sr-rich solid solutions is favoured over Ba-rich solid solutions because the critical supersaturation of $SrSO_4$ ($\Omega = 39$) is much lower than that of $BaSO_4$ ($\Omega = 1000$). These values, taken from droplet experiments reported in Walton (1969) and cited in Prieto et al. (1993), imply that in a mixed solution with e.g. $\Omega\ (SrSO_4) = 50$

and Ω ($BaSO_4$) = 900, precipitation of a celestite-rich solid solution would occur in spite of the much higher supersaturation with respect to barite. This aspect needs be considered in the interpretation of experimental data.

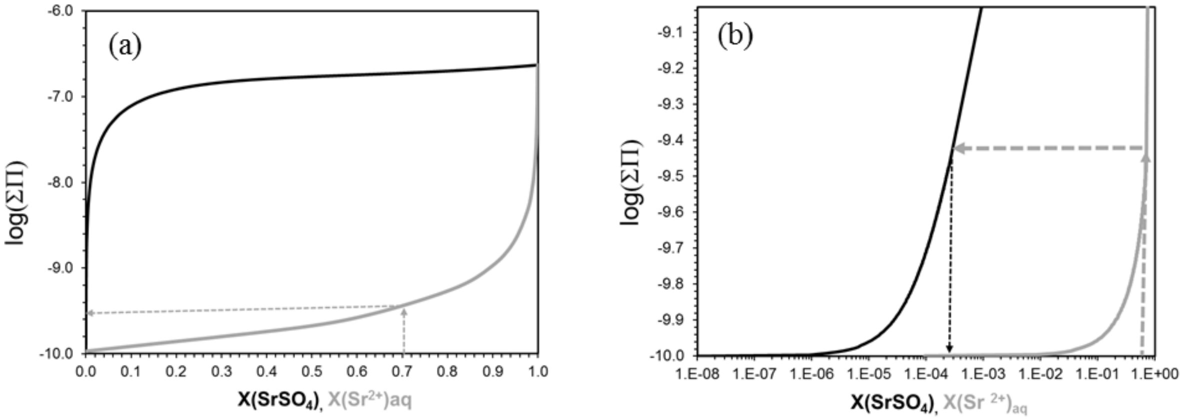

Fig. 8: Lippmann diagram for the barite-celestite binary: (a) complete diagram; (b) partial diagram with the x-axis in log-scale.

4.2. Application of classical nucleation theory

In the experiments presented, two distinct barite precipitates have been observed and identified: i) nano-crystalline barite filling the pore space and ii) a thin barite overgrowth on large and medium-sized celestite crystals ($SrSO_4$). Whereas Fig. 3b and 3c (9-28 hours from the start of $BaCl_2$ injection) show apparently that precipitation of the fine-grained compound preceded the formation of the rims, in Fig. 3f (300 hours) the opposite seems to be true. This apparent inconsistency suggests that conditions favourable to the formation of either phase may vary locally within the reactive celestite zone. At the longest injection time (Fig. 3f) the rim was shown to consist of tiny crystals with the same orientation as the celestite substrate, as expected for epitaxial growth (Fig. 6 and section 3.3). This suggests that two nucleation mechanisms were involved: homogeneous nucleation (nanoparticle aggregate) and heterogeneous nucleation (epitaxial rim). The nucleation mechanisms which lead to the precipitation of ionic solids and particularly of barite are discussed in detail in Kashchiev and van Rosmalen (2003) based on the Classical Nucleation Theory (CNT). We apply here the same principles, in spite of a current debate on the applicability of CNT (Gebauer et al., 2014). As pointed out by Prieto (2014), CNT is still a valid tool to explain precipitation phenomena specifically for sulfate minerals such as barite, which unlike carbonates does not form allotropic precursors.

For the interpretation of our data, we use the empirical findings and model of Prieto (2014), which are based on earlier counter diffusion experiments described in Prieto et al. (1990). In these experiments $BaCl_2$ and Na_2SO_4 solutions were introduced on opposite sides of a U-tube filled with porous silica hydrogel, leading to precipitation of barite. Dissolved sulfate and barium ion concentrations were determined analytically across the diffusion profile at different times. From these data, the degree of supersaturation was determined as a function of time and location in the column. Using microscopy, the time elapsed between the start of experiment and first appearance of crystals was determined, from which induction times for the start of precipitation in each experiment were derived. The application of plane CNT to precipitation in porous media leads to under prediction of induction times (the time of onset of homogeneous precipitation) by several orders of magnitude. Typically, homogeneous precipitation in porous media starts only after days or weeks, not after a few seconds as predicted by the theory. This inconsistency is mainly due to the pore size effect (Prieto, 2014). Unlike a free bulk solution, a porous medium divides the fluid in a large number of pores, which act as "microscopic separate chambers" with respect to nucleation. Because the nucleation probability is essentially proportional to the solution volume, homogeneous precipitation in small pores will be much more difficult than in a bulk solution. This point is illustrated by the basic equation for the induction time (Kashchiev and van Rosmalen, 2003):

$$t_i = \frac{1}{JV} \qquad (1)$$

where t_i is the theoretical induction time, J is the nucleation rate and V is the volume of fluid. The induction time is the time required to form a $BaSO_4$ molecular cluster just above the critical size, beyond which further growth becomes energetically favourable and precipitation should start. In porous media, it is not appropriate to set the total volume of fluid in the equation above; a characteristic pore volume size is more suitable. Prieto (2014) was indeed able to remove the aforementioned inconsistency between predicted and measured induction times by setting the characteristic pore sizes (0.1 - 1 µm) of the silica gel used in his experiments in equation 1. A major consequence of this pore-size effect is that precipitates formed via homogeneous precipitation should be concentrated in large pores.

The "theoretical" induction time to reach stationary nucleation rate using equation 1 for both homogeneous and heterogeneous nucleation for an averaged pore size of (100 µm)^3, as the highly concentrated solution of $BaCl_2$ reaches the reactive medium (critical supersaturation of 4), takes place within seconds (instantaneously).

For the interpretation of our data, it is not possible to apply, equation 1 which is suitable for analysis of t_i data only when they are obtained by experimental techniques allowing counting the number N of nuclei or detecting the appearance of a single nucleus in the solution (Kaschiev and van Rosmalen, 2003). However, in our experiments, it was not possible to monitor and count the appearance of nuclei. The SEM images taken at discrete time intervals only allowed us to detect newly formed barite at a resolution of about 1 µm. In such a case the expression to be used is equation 38 in Kashchiev and van Rosmalen (2003):

$$t_{exp} = \left(\frac{3\alpha_v}{\pi G^3 J}\right)^{\frac{1}{4}} \qquad (2)$$

where α_v is the detectable volume fraction of the new phase i.e. the ratio of detectable volume V_d of the nucleating phase to total volume V of the system (Kashchiev, 2000). In our case, V is equated to the total assumed volume of the single pore, V_p, yielding $\alpha_v = \frac{V_d}{V_p}$. V_d is assumed to be 1 µm^3 which corresponds approximately to the resolution of our SEM images. $G = \frac{dR}{dt}$ is the growth rate of the nucleating phase (R is the crystallite radius). It is important to note that G could only be roughly estimated assuming that the barite nanoparticles grew to a radius of 10 nm

(10^{-8} m) after 9 hours. This is the first time after start of the experiments for which microscopic images are available. Dividing 10 nm by 9 hours yields $G = 3.09 \times 10^{-13}$ ms^{-1}, set into equation 2. We used t_{exp} (instead of t_i as in the original publication) in equation 2 to emphasize the fact that the formula expresses the time of first appearance of an experimentally detectable precipitate.

The model developed by Prieto (2014) to calculate Supersaturation-Nucleation-Time (SNT) diagrams for homogeneous and heterogeneous nucleation has been implemented and adapted here to our experiments. Such diagrams provide curves of induction time vs. supersaturation, calculated from equations based on concepts and parameters used in CNT. Briefly, the model calculates the time needed to start homogeneous and heterogeneous nucleation from the production rate (J) of nuclei just exceeding the critical size. Beyond the critical size, the free energy of the nuclei decreases, leading to fast spontaneous growth. The nuclei are treated as spherical aggregates of dissolved “monomers”, i.e. the simplest molecules needed to build the solid (the aqueous $BaSO_4$ complex in the case of barite). J depends on a number of parameters, like the volume of the “monomer”, the surface area and size of the critical nucleus, the diffusion coefficient of the “monomers” and their concentration. Details on the assumptions, equations and parametrization of the model can be found in Prieto (2014) and references therein. The purpose here was to provide a theoretical framework to understand qualitatively our observations. Predictive calculations are indeed not possible, as some input parameters, such as interfacial tension of the precipitating solid and the pore volume, are difficult to measure or ill-defined.

The main model adaptation was the selection of a characteristic pore size (V_p), which we set for our calculations to $(100\ \mu m)^3$ and $(10\ \mu m)^3$ to represent typical pores in our porous medium (Fig. 3a). Further, we had to provide a value for N_1, the number of dissolved $BaSO_4$, aqueous monomers per unit volume of fluid. In principle, this is a space and time dependent quantity that may vary by several orders of magnitude through the reactive celestite region. In order to account for the variation of this parameter, we calculated two limiting values via GEMS-PSI speciation calculations (Kulik et al., 2013) using the data compiled in Hummel et al. (2002): a maximum value ($N_1 = 2.94 \times 10^{23}\ m^{-3}$) representing the pre-equilibrium $BaSO_4$, aqueous concentration resulting from mixing 0.3 M $BaCl_2$ with saturated celestite solution, and a minimum value ($N_1 = 3.23 \times 10^{19}\ m^{-3}$) after full equilibration. These limiting values were used as fixed parameters in alternative calculations. Finally, we chose a lower value than Prieto (2014) for the effective interfacial tension ($\sigma_{eff} = 0.045\ J\ m^{-2}$, corresponding to a wetting angle $\Theta = 40^o$) to describe epitaxial growth of barite on celestite, which is a more favourable substrate for epitaxial growth of barite compared to the silica hydrogel used by Prieto et al. (1990). The net effect of reducing σ_{eff} is to decrease the threshold supersaturation required to initiate heterogeneous nucleation.

The results of our calculations are illustrated in Fig. 9, which shows two pairs of SNT diagrams calculated assuming the two aforementioned monomer concentrations and for pores of 10 and 100 µm. Detailed equations used to reproduce the SNT diagram (Fig. 9) are given in the appendix.

As the 0.3 M $BaCl_2$ solution reaches the quartz-celestite interface, a very high supersaturation will be almost instantaneously established. Our speciation calculations, carried out with the

GEMS-PSI and using the extended Debye-Hückel equation, yield a saturation index (SI) close to 4.0 ($\Omega = 10^4$). For a given pore of (100 μm)^3 the induction times at SI = 4, homogeneous and heterogeneous nucleation start respectively 9 and 1 hours after the impact of the $BaCl_2$ solution with the celestite zone. While the (9 hours) coincides with our observations (Fig. 3b), the predicted appearance time of heterogeneously nucleated barite is much lower than observed in our SEM images (28 hours, see Fig. 3 c). This apparent inconsistency may be explained by the different nature of the considered nucleation processes. Homogeneous nucleation proceeds by volume growth at preferential locations (resulting in a few, but easily visible spots in the SEM images), heterogeneous nucleation proceeds via lateral spreading on a large amount of pre-existing celestite surface area. Moreover, whereas homogeneous nucleation, once started, is a chain-reaction like process (very fast), epitaxial growth of barite on the celestite crystals will proceed at considerably slower rates. Indeed, epitaxial growth occurs at lower growth rates as it involves the diffusion of solutes to the surface of the mineral. After 300 hours, an average of 3 μm rim of barite overgrowth on celestite crystals is seen, which gives an estimated growth rate of 10 nm hour^{-1} (0.09 um after 9 hours which is not detectable at the resolution of our SEM image, Fig. 3a and 3b). These explain why the nano-crystalline barite aggregate appears in our experiments before the epitaxial barite formation becomes visible. Following the sudden precipitation of nano-barite, the local SI will decrease abruptly, e.g. to SI ~ 0.5 (due to continuous supply of SO_4^{2-} from celestite dissolution and $BaCl_2$, SI = 0 will not be reached). Further supply of $BaCl_2$ solution and dissolution of celestite will then increase the SI until the appropriate heterogeneous curve is intersected. From this moment on, epitaxial growth will proceed with no concurrent homogeneous nucleation.

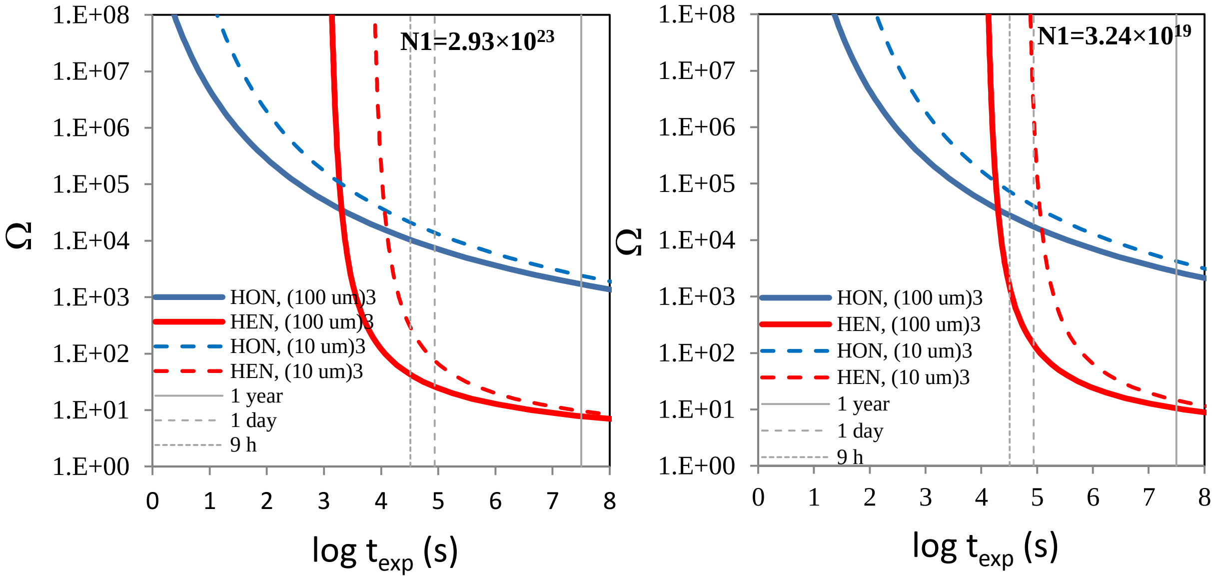

Fig. 9: SNT diagrams for homogeneous (HON) and heterogeneous (HEN) nucleation optimized for our reactive transport experiments, assuming two bounding concentrations of $BaSO_4$, aq monomers (“high N1” (a) and “low N1” (b)) and for pore sizes varying between 10 μm to 100 μm.

Roughly, the CNT model agrees with of our observations: at the first impact of $BaCl_2$ with celestite, both epitaxial barite and nano-barite can be formed. The amount of nano-barite formed will be limited by the supply of sulfate, which will be larger in the regions filled with small celestite crystals (larger surface area). Therefore, the nanophase will form dominantly at the expense of small celestite crystals, which will be rapidly consumed or isolated from solution. Micro-XRD analysis of the barium rich crystalline phase that fills the pore space showed spot-like celestite reflections corresponding to such residual celestite crystals.

Once the small celestite crystals are consumed or isolated from the solution, or the supply of $BaCl_2$ is locally interrupted, the SI of barite decreases rapidly. A low supersaturation with respect to barite will be nevertheless maintained via dissolution of large celestite crystals and supply of $BaCl_2$. The supply of sulfate is now slower since only larger celestite crystals (low specific surface area) are involved. Under such conditions, homogeneous nucleation is excluded and only epitaxial growth is possible. The rim of crystalline barite grows on the surface of the large celestite crystals.

The fact that after 300 hours the newly precipitated solid on celestite crystals is pervasive (Fig. 3f) might also be the consequence of a dissolution-crystallization process (recrystallization) which would be driven by the slightly higher solubility of fine-grained precipitates in comparison to larger-grained ones Schindler (1967). The difference in solubility between the fine-grained and the epitaxial precipitates would lead to an Ostwald ripening process which would proceed through the simultaneous dissolution of the fine-grained precipitate and the growth of the epitaxial precipitate (Baronnet, 1982; Morse and Casey, 1989). This process could explain the different features observed in Fig. 3e and 3f.

As can be seen in Fig. 3a, the initial pore size distribution is quite heterogeneous with pore sizes varying between 10 and 500 µm. Initially, the celestite porous medium consisted of non-cemented grains of celestite, in which pore connectivity is larger than in a porous rock (e.g. sandstone), where grains are cemented. Putnis and Mauthe (2001), Stack et al. (2014), Nindiyasari et al. (2014) and Prieto (2014) reported in detail the dependence of nucleation kinetics on the pore size in porous media. The effect of reducing the pore size is an inhibition of nucleation so that the curves in Fig. 9 would shift considerably to the right if the pore size is reduced from 10 µm to 1 µm. In contrast, the curves shift to the left at higher pore sizes. The curves of Fig. 9 are calculated for the minimum pore size $(10\ \mu m)^3$ and average pore size $(100\ \mu m)^3$. The induction time for $(10\ \mu m)^3$ pores is ~ 4 hours for heterogeneous nucleation and 319 hours for homogeneous nucleation. As mentioned above, the induction time for $(100\ \mu m)^3$ pores are 1 and 9 hours for homogeneous and heterogeneous nucleation respectively. For larger pores $(> 100\ \mu m)^3$, kinetic effect related to pore size would hardly be observable in our system, since the corresponding curves for larger pores would shift to the left and imply even shorter induction times for both homogeneous and heterogeneous nucleation at high supersaturation. In our experiments, nano-barite crystals appear first along the main flow pathways as shown in Fig. 3b, but also across the entire celestite medium afterwards. A preferential formation of nano-barite in the larger pores compared to smaller pores e.g. $(30\ \mu m)^3$ was not detectable with our measurements, probably because in our system pore connectivity is larger. For a better evaluation of the possible dependence of nano-crystalline formation in larger pores, tomography measurements will be performed.

Micro-XRD analysis also showed the absence of (Ba,Sr)SO_4 solid solutions. This result is easily understandable by considering the Lippmann diagram in Fig. 8. The continuous supply of relatively concentrated $BaCl_2$ solution and the fact that local Sr concentrations cannot exceed 0.6 mM (celestite equilibrium is approached from under saturation, so SI = 0 will never be exceeded) will ensure low values of the aqueous Sr mole fraction and thus favour precipitation of pure barite. Non-equilibrium precipitation of Sr-rich end-members as described by Prieto et al. (1993) is not possible simply because SI ($SrSO_4$) will never exceed zero. Under such conditions, the formation of $SrSO_4$ critical nuclei can be excluded. Only barite clusters will be formed, preventing the precipitation of (Ba, Sr)SO_4 solid solution.

5. Conclusions and outlook

With the current study, we identified the formation of two distinct crystalline pure barite phases following celestite dissolution in porous media, induced by injection of $BaCl_2$ solution. These phases include an epitaxial growth of barite micro-crystals on large celestite crystals and a nano-crystalline barite phase with residues of celestite crystals in the pore interstices. The observed temporal precipitation sequence showed that at least in the first stages of the reaction, the formation of a nano-crystalline barite phase resulting from homogeneous nucleation appears before the growth of epitaxial barite on celestite crystals. However, classical nucleation theory predicts that the induction time for homogeneous nucleation and heterogeneous nucleation is 1 hour and 9 hours respectively. This apparent inconsistency may be resolved by considering that heterogeneous growth on celestite substrates cannot be detected in early stages of the process. From SEM images, rim thickness of 3 µm in 300 hours is detected which correspond to a growth rate of 10 nm/hour.

The experimental observation also showed the limits of the reactive transport model used by Poonoosamy et al. (2015). Although kinetic effects were implemented by fixing two distinct rates for the dissolution of large and small celestite crystals, effects due to precipitation kinetics and metastability of supersaturated solutions were neglected (instantaneous precipitation of barite was assumed as soon as saturation was exceeded). The results of the present mineralogical-microscopic investigation clearly show that precipitation kinetics effects related to metastability of supersaturated solutions and distinct nucleation mechanisms are important and have certainly an impact on fluid flow properties. Therefore, these results prompt for future improvements of the reactive transport model. In the continuum scale model which considered average medium properties, the experimental data for total minerals ($BaSO_4$ and $SrSO_4$) were well reproduced by assuming barite precipitation at equilibrium. However for pore scale modelling which considers subgrid changes, the nucleation mechanisms should be taken into account. In addition, experiments of Prieto et al. (1990) showed that metastable conditions may exist at which nucleation cannot occur despite high supersaturation. Our future work will thus concentrate on the effect of supersaturation on epitaxial growth and homogeneous precipitation of barite in celestite porous media. This will be achieved by developing appropriate pore scale models and hopefully result in a better understanding of reactive transport in porous media.

Acknowledgments

We gratefully acknowledge Nagra for funding the research, Dr. D. Kulik for useful discussion, T. Aebi for the thin section preparation, Dr. J. Hadi for his assistance in resin impregnation and finally Dr. A. Jenni for his assistance in SEM operation. We also thank the Swiss Light Source for providing beam time to analyse our samples.

References

Aquilina L., Pauwels H., Genter A. and Fouillac C. (1997). Water-rock interaction processes in the Triassic sandstone and the granitic basement of the Rhine Graben: Geochemical investigation of a geothermal reservoir. *Geochim. Cosmochim. Acta*, **61**, 4281-4295.

Baronnet A. (1982). Ostwald ripening in solution. The case of calcite and mica. *Estudios Geologicos*, **38**, 185-198.

Brandt F., Curti E., Klinkenberg M., Rozov K. and Bosbach D. (2015). Replacement of barite by a (Ba,Ra)SO_4 solid solution at close-to-equilibrium conditions: A combined experimental and theoretical study. *Geochim. Cosmochim. Acta*, **155**, 1-15.

Ceccarello S., Black S., Read D. and Hodson M.E. (2004). Industrial radioactive barite scale: Suppression of radium uptake by introduction of competing ions. *Miner. Eng.*, **17**, 323-330.

Curti E., Fujiwara K., Iijima K., Tits J., Cuesta C., Kitamura A., Glaus M.A. and Müller W. (2010). Radium uptake during barite recrystallization at 23 ± 2 °C as a function of solution composition: An experimental ^{133}Ba and ^{226}Ra tracer study. *Geochim. Cosmochim. Acta*, **74**, 3553-3570.

Dauzeres A., Le Bescop P., Sardini P. and Cau Dit Coumes C. (2010). Physicochemical investigation of clayey/cement-based materials interaction in the context of geological waste disposal: Experimental approach and results. *Cem. Concr. Res.*, **40**, 1327-1340

Deer W.A., Howie R.A., and Zussman J. (1992). An introduction to the Rock-Forming Minerals. *Longman Scientific & Technical,* Essex.

De Nolf W., Vanmeert F. and Janssens K. (2014). XRDUA: crystalline phase distribution maps by two-dimensional scanning and tomographic (micro) X-ray powder diffraction. *J. Appl. Crystallogr.*, **47**, 1107-1117.

Emmanuel S. and Berkowitz B. (2007). Effects of pore-size controlled solubility on reactive transport in heterogeneous rock. *Geophys. Res. Lett.* , **34**, L06404.

Fu Y., van Berk W. and Schulz H.M. (2012). Hydrogeochemical modelling of fluid-rock interactions triggered by seawater injection into oil reservoirs: Case study Miller field (UK North Sea). *Appl. Geochem.*, **27**, 1266-1277.

Gebauer D., Kellermeier M., Gale J.D., Bergström L. and Cölfen, H. (2014). Pre-nucleation clusters as solute precursors in crystallization. *Chem. Soc. Rev.*, **43**, 2348-2371.

Hummel W., Berner U., Curti E., Pearson F.J. and Thoenen T. (2002). Nagra/PSI chemical thermodynamic data base 01/01. *Universal Publishers*, Parkland Florida.

Jenni A., Mäder U., Lerouge C., Gaboreau S. and Schwyn B. (2014). In situ interaction between different concretes and Opalinus Clay. *Phys. Chem. Earth*, A/B/C, **70-71**, 71-83

Kang Q., Zhang D., and Chen S. (2003). Simulation of dissolution and precipitation in porous media. *J. Geophys. Res.*, **108**, 2505.

Kashchiev D. (2000). Nucleation: Basic Theory with Applications. *Butterworth-Heinemann*, Oxford.

Kashchiev D. and van Rosmalen G.M. (2003). Review: Nucleation in solutions revisited. *Cryst. Res. Technol.*, **38**, 555-574.

Kulik D.A., Wagner T., Dmytrieva S.V., Kosakowski G., Hingerl F.F., Chudnenko K.V. and Berner U. (2013). GEM-Selektor geochemical modeling package: Revised algorithm and GEMS3K numerical kernel for coupled simulation codes. *Computat. Geosci.*, **17**, 1-24.

Morse J.W. and Casey W.H. (1989). Ostwald processes and mineral paragenesis in sediments. *Am. J. Sci.*, **288**, 537-560.

Mundhenk N., Huttenloch P., Sanjuan B., Kohl T., Steger H. and Zorn R. (2013). Corrosion and scaling as interrelated phenomena in an operating geothermal power plant. *Corros. Sci.*, **70**, 17-28.

Nicholson R.V., Gillham R.W. and Reardon E.J. (1990). Pyrite oxidation in carbonate-buffered solution: 2. Rate control by oxide coatings. *Geochim. Cosmochim. Acta*, **54**, 395-402.

Nindiyasari F., Fernández-Díaz L., Griesshaber E., Astilleros J.M, Sánchez-Pastor N. and Schmahl W.W. (2014). Influence of gelatin hydrogel porosity on the crystallization of CaCO3. *Cryst. Growth Des.*, **14**, 1531-1542.

Nielsen A.E. (1967). Nucleation in aqueous solution. *J. Phys. Chem. Solids*, **1**, 419-426.

Oddo J.E. and Tomson M.B. (1994). Why scale forms and how to predict it. *SPE Prod. Facil.*, **9**, 47-54.

Pina C.M., Enders M. and Putnis A. (2000). The composition of solid solutions crystallising from aqueous solutions: the influence of supersaturation and growth mechanisms. *Chem. Geol.*, **168**, 195-210.

Poonoosamy J., Kosakowski G., Van Loon L.R. and Mäder U. (2015). Dissolution-precipitation processes in tank experiments for testing numerical models for reactive transport calculations: Experiments and modelling. *J. Contam. Hydrol.*, **177-178**, 1-17.

Prieto M. (2014). Nucleation and supersaturation in porous media (revisited). *Mineral. Mag.*, **78**, 1437-1447.

Prieto M., Putnis A. and Fernández-Díaz L. (1990). Factors controlling the kinetics of crystallization: Supersaturation evolution in porous medium. Application to barite crystallization. *Geol. Mag.*, **127**, 485-495.

Prieto M., Putnis A. and Fernández-Díaz L. (1993). Crystallization of solid solutions from aqueous solutions in a porous medium: zoning in (Ba,Sr)SO_4. *Geol. Mag.*, **130**, 289-299.

Putnis A. and Mauthe G. (2001). The effect of pore size on cementation in porous rocks. *Geofluids*, **1**, 37-41.

Putnis A., Prieto M. and Fernández-Díaz L. (1995). Fluid supersaturation and crystallization in porous media. *Geol. Mag.*, **132**, 1-13.

Sánchez-Pastor N., Pina C.M., Astilleros J. M., Fernández-Díaz L. and Putnis A. (2005). Epitaxial growth of celestite on barite (001) face at a molecular scale. *Surf. Sci.*, **581**, 225-235.

Sánchez-Pastor N., Pina C.M. and Fernández-Díaz L. (2006). Relationship between crystal morphology and composition in the (Ba,Sr)SO_4-H_2O solid solution-aqueous solution system. *Chem. Geol.*, **225**, 266-277.

Schindler P.W. (1967). Heterogeneous equilibria involving oxides, hydroxides, carbonates and hydroxides carbonates. Equilibrium Concepts in Natural Water Systems. *Adv. Chem. Ser.*, **67**, 197-221.

Schott J., Pokrovsky O.S. and Oelkers E.H. (2009). The link between mineral dissolution/precipitation kinetics and solution chemistry. *Rev. Min. Geochem.*, **70**, 207-258.

Shao H., Dmytrieva S.V., Kolditz O., Kulik D.A., Pfingsten W. and Kosakowski G. (2009). Modeling reactive transport in non-ideal aqueous-solid solution system. *Appl. Geochem.*, **24**, 1287-1300.

Stack A.G., Fernandez-Martinez A., Allard L.F., Bañuelos J.L., Rother G., Anovitz L.M., Cole D.R. and Waychunas G.A. (2014). Pore-size-dependent calcium carbonate precipitation controlled by surface chemistry. *Environ. Sci. Technol.*, **48**, 6177-6183.

Walton A.G. (1969). Nucleation in liquids and solutions. Nucleation (ed. Zettlemoyer A.C.). *Marcel Dekker Inc.*, New York.

Zhu C. (2004). Coprecipitation in the Barite Isostructural Family: 1. Binary Mixing Properties. *Geochim. Cosmochim. Acta*, **68**, 3327-3337.

Appendix

The nucleation rate, J [m^{-3}s^{-1}] varies exponentially with the free energy change (ΔG_c) associated with the formation of a nucleus of critical size (Prieto, 2014):

$$J = \Gamma \exp(-\frac{\Delta G_c}{kT}) \qquad (3)$$

where k is the Boltzmann constant, T is the absolute temperature and Γ a pre-exponential factor. The nucleation barrier is highly dependent upon the interfacial tension σ and supersaturation index SI:

$$\Delta G_c = \frac{\beta v^2 \sigma^3}{(kT \ln(\mathrm{SI}))^2}, \qquad (4)$$

β is a geometry factor, set to 16.8 for a sphere, σ was set to 0.134 J m^{-2} according to Nielsen (1967), v is the volume of a single (spherical) $BaSO_4$ monomer, which was set to 8.60×10^{-29} m^3 (Prieto, 2014). For heterogeneous nucleation, the interfacial tension (σ_{HEN}), was calculated as a function of the contact angle Θ between substrate and growing mineral, according to Kashiev and van Rosmalen (2003):

$$\sigma_{HEN} = ((0.25(2 + \cos(\Theta))(1 - \cos(\Theta))^2)^{\frac{1}{3}}.\sigma, \qquad (5)$$

The pre-exponential factor in eq. (2), Γ, represents the rate of attachment of monomers controlled by diffusion and is given as:

$$\Gamma = 2\pi Z D N_1 N_0 d_c, \qquad (6)$$

where D is the diffusion coefficient of monomers set to 9.3×10^{-9} m^{2}s^{-1} and $d_c = \frac{4\sigma v}{kTln(SI)}$. N_1 and N_0 are concentrations that represent the number of monomers per unit volume of fluid and the number of nucleation sites respectively. N_0 (HON) was set to 3.33×10^{28} m^{-3} and N_0(HEN) was set to 2.50×10^{13} m^{-3}, the same values used by Prieto (2014). N_1 depends on the supersaturation and was evaluated using GEMs-PSI (see main article).

Z is the Zeldovich factor given as:

$$Z = \left(\frac{\Delta G_c}{3\pi kT (n_c)^2}\right)^{\frac{1}{2}}, \qquad (7)$$

The number of monomers in the critical nucleus, n_c, is given as:

$$n_c = \left(\frac{2\sigma a}{3kTln(SI)}\right)^3, \qquad (8)$$

where a is the surface area of a single nucleus.

Using the above formulas and equation 2 from the main text, the *SNT* diagrams shown in Fig. 9 for our system were evaluated.

Chapter 4: PSI - Reactive transport benchmark

10.2 PSI - Reactive transport benchmark

Jenna Poonoosamy, Georg Kosakowski, Luc R. Van Loon, Urs Mäder

In this chapter we briefly summarize the reactive transport experiments we conducted in a flow cell and which are described in Poonoosamy et al. (2015). Then we present our numerical simulations whose results were benchmarked against our experimental work. We considered three case studies with increasing complexity: case 1 considers a 2D system with density driven flow and conservative mass transport, case 2 in addition includes the dissolution and precipitation of mineral phases leading to porosity changes and case 3 extends the case 2 by considering the formation of solid solutions. We used the OpenGeoSys-GEM simulator, which uses finite element solvers for fluid flow and mass transport implemented in OpenGeoSys, coupled with GEMS for chemical equilibrium calculations (Kosakowski and Watanabe, 2014). The numerical calculation with OpenGeosys-GEM will be compared with other reactive transport codes within the framework of SeS benchmark projects.

10.2.1 Definition of the problem set-up

We designed a 2D reactive transport experimental benchmark which aims to be reproducible, fast to conduct and with a simple chemical set up. In what follows, we briefly summarize the experiment formulated to benchmark numerical simulations of flow of a fluid with variable density coupled with reactive transport (Poonoosamy et al., 2015). The experiment was conducted using the flow cell depicted in Fig. 10.2.1, which allowed us to visualize dye tracer tests. It consists of a reactive porous layer of strontium sulphate ($SrSO_4$) between two inert porous layers composed of silicon dioxide (SiO_2). The flow cell has dimensions of $0.1\times0.1\times0.01$ m, and it contains several ports for fluid injection and sampling. The inlet and outlet positions were chosen to create an asymmetric flow field. The chemical transformations in the flow cell were monitored by taking samples of the pore solution at ports 'c' and 'd', as well as by collecting the effluent at the outlet. The pressure difference between ports 'a' and 'b' was also measured. We performed post mortem analysis to determine the nature and location of the mineralogical transformations of the reactive media. Our numerical simulations will follow up this setup, and we will use our experimental measurements to quantitatively benchmark them. A qualitative benchmark will also be shown using images of the dye tracer distribution throughout the flow cell.

In Table 10.2.1, we list the properties of the different regions Q1, Q2, and Q3 shown in Fig. 10.2.1, as well as properties of the fluid and initial conditions used for the numerical calculations. The coordinates (x, z) of the ports 'a' and 'b', where pressure sensors were installed, are (0.02 m, 0.02 m)

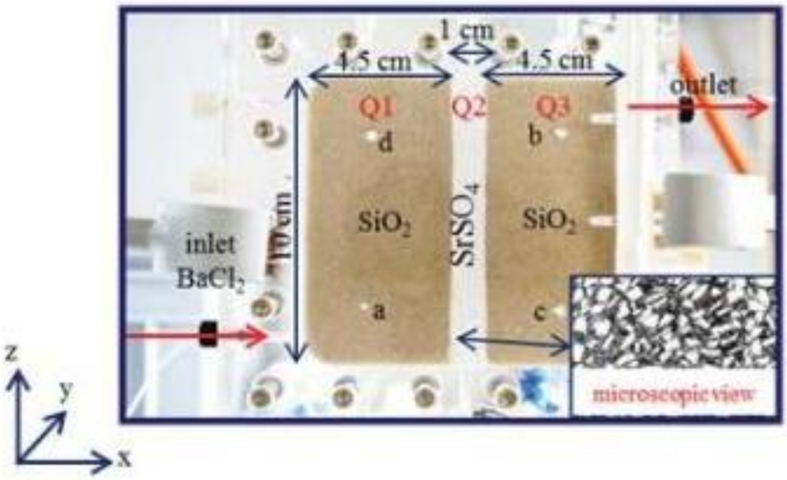

Fig. 10.2.1: Geometry of the numerical benchmark.

and (0.08 m, 0.08 m) respectively. The ports 'c' and 'd', where sampling was performed, are located at (0.08 m, 0.02 m) and (0.02 m, 0.08 m) respectively. These are the coordinates one should use to compare numerical results with the experimental measurements presented in Poonoosamy et al. (2015).

Table 10.2.1: Properties of the different regions of porous media

Characteristics	**Q1**	**Q2**	**Q3**
Length [m] case 1 & 2	0.045	0.01	0.045
Length [m] case 3	0.045	0.005	0.055
Initial porosity (w_0) [-] case 1 & 2	0.34	0.33	0.40
Initial porosity (w_0) [-] case 3	0.34	0.40	0.40
Initial permeability k_0 [m^2] case 1, 2	1.82×10^{-11}	1.8×10^{-14}	1.82×10^{-11}
Initial permeability k_0 [m^2] case 3	1.82×10^{-11}	3.0×10^{-14}	1.82×10^{-11}
Dispersivity α [m]	10^{-5}	10^{-5}	10^{-5}
Diffusion coefficient D_w[m^{2}s^{-1}]	10^{-9}	10^{-9}	10^{-9}
Volume fraction of silicon dioxide case 1, 2 & 3 [-]	0.66	0	0.60
Total volume fraction of SrSO$_4$ case 1 & 2 [-]		0.67	
Volume fraction small strontium sulphate grains case 2 [-]	0	0.223	0
Volume fraction large strontium sulphate grains case 2 [-]	0	0.447	0
Total volume fraction of SrSO$_4$ case 3 [-] (one strontium sulphate grain size only.)		0.60	
Initial pH (fixed by initial chemical set up.)	5.6	5.6	5.6

In case 2, the Q2 region is composed of bimodal grain size distribution of SrSO$_4$ crystals (mixture of large and small grains).

We define three different benchmark cases with increasing complexity. In Case 1, we study density driven flow with conservative mass transport. In Case 2, we in addition consider dissolution and precipitation of mineral phases leading to porosity changes. Finally, Case 3 extends the Case 2 by inclusion of the possible formation of solid solutions. Table 10.2.2 provides additional information on the inlet and outlet conditions for the three case studies. For all simulations, we considered a discretization of the squared geometry in Fig. 10.2.1 by triangular elements. For Cases 1 and 3, a node distance of 1 mm was chosen, while for Case 2 a more refined mesh was adopted, with a node distance of 0.5 mm.

Table 10.2.2: Characteristics of the inlet and outlet.

Characteristics	**Case 1**	**Case 2**	**Case 3**
Inlet (x=0 m; z from 0.008 to 0.0113 m) [m]	0.0033	0.0033	0.0033
Outlet (x=0.1 m; z from 0.08855 to 0.09185 m) [m]	0.0033	0.0033	0.0033
Source term [μL min^{-1}] at inlet	20.0	20.0	10.0
NaCl concentration [mol L^{-1}] at inlet	1.4	NA	NA
$BaCl_2$ concentration [mol L^{-1}] at inlet	NA	0.3	0.001
$SrCl_2$ concentration [mol L^{-1}] at inlet	NA	NA	0.099
Pressure at outlet [Pa]	101325	101325	101325
Amount [mL] of 3 g L^{-1}dye tracer injected	0.5	NA	NA
Modelling time duration [hours]	24	200	600

NA: not applicable

Case 1: *Conservative mass transport coupled with a density driven flow.*
Here we consider the injection of a highly concentrated solution of sodium chloride (NaCl of density 1.056 kg dm^{-3}) in a flow cell, initially saturated with water (density 1 kg dm^{-3}). An injection of 0.5 mL of a conservative tracer at the inlet is carried out at a rate of 20 μL min^{-1}, followed by the inflow of a NaCl solution for 24 hours. This NaCl solution was saturated with strontium sulphate ($SrSO_4$). The Q2 region, composed of $SrSO_4$, was assumed to be unreactive in this case study. The system was simulated for 24 hours.

Case 2: *Reactive transport with porosity changes.*
A highly concentrated solution of barium chloride ($BaCl_2$) is injected in a flow cell. The injection of $BaCl_2$ enhances the dissolution of $SrSO_4$ and causes barium sulphate ($BaSO_4$) to precipitate according to the reaction:

$$BaCl_{2(aq)} + SrSO_{4(s)} \rightarrow BaSO_{4(s)} + SrCl_{2(aq)} \tag{10.2.1}$$

Porosity changes are likely to occur given that $BaSO_4$has a larger molar volume than $SrSO_4$. As a result, material medium properties such as permeability and diffusivity will equally change. The reactive layer Q2 has an initial porosity of 33% and is composed of two grain size populations of $SrSO_4$ (i.e., celestite 1 and celestite 2). Celestite 1 corresponds to $SrSO_4$ with a grain size of 10-63 μm, while celestite 2 has a much higher grain size in the range 250-400 μm. Different kinetic rates of dissolution are used for these two grain populations (see section 10.2.2). The following reactive surface areas (per volume unit) were attributed to the small and large crystals respectively: 20000 $m^2\ m^{-3}$ and 100 $m^2\ m^{-3}$. We assumed no kinetic constraints on the precipitated barite ($BaSO_4(s)$) phase. The simulation time is set to 200 hours.

Case 3: *Reactive transport involving the formation of a solid solution.* Here the reactive media is composed of celestite with a single grain size population of 63-125 μm. The reactive surface area (per volume unit), $a_{(SrSO4)}$, is 10000 $m^2\ m^{-3}$. A solution composed of 0.099 mol L^{-1} $SrCl_2$ and 0.001 mol L^{-1} $BaCl_2$ is injected at the inlet at a flow rate of 10 μL min^{-1}. The simulation time is set to 600 hours.

The chemical configurations for Case 1, Case 2 and Case 3 are summarized in Table 10.2.4, Table 10.2.5 and Table 10.2.6 in the annex.

10.2.2 Description of the coupled code

The fluid flow and mass transport equations are solved by OpenGeoSys, and the chemical processes by the GEMS3K kernel code of GEM-Selektor V3 (Kulik et al., 2013). The coupling of these two codes is referred as OpenGeoSys-GEM, and its capabilities are described in Shao et al. (2009) and Kosakowski and Watanabe (2014). Mass transport and chemical reactions are solved in a sequential non-iterative approach (SNIA), i.e. the transport and reaction equations are solved separately in a sequential manner without iteration between them.

The GEM approach consists of calculating the equilibrium state of a chemical system via minimization of its Gibbs free energy. The minimization is constrained by mass balance equations where the given total amounts of chemical elements are conserved. An additional charge balance equation is also imposed to enforce the electrically neutral condition of the system. The calculated equilibrium state by GEMS3K not only provides the molar amounts of every species in the system, which indicates which phases are stable or unstable, but also important chemical quantities such as species activities that are needed for calculation of kinetic rates of mineral dissolution. The thermodynamic data (standard Gibbs energy of formation [kJ mol^{-1}]) of aqueous, gaseous and solid species considered in our chemical system and the molar volumes [$m^3\ mol^{-1}$] based on the PSI/NAGRA thermodynamic database (Hummel et al., 2002), are given in Table 10.2.3.

In OpenGeosys-GEM the density of the aqueous phase is calculated by GEM3K. This is done by calculating the partial molar volumes of each aqueous species at the temperature and pressure of interest, and summing the product of these partial molar volumes by the corresponding molar amounts of the aqueous species to obtain the volume of the aqueous phase. The total mass of the phase divided by this volume gives the density of the aqueous phase, which is dependent on its molar composition. This density is updated after each chemical equilibrium calculation and passed along to the fluid flow solver.

Density flow

During the numerical simulations, the velocity field is calculated by solving the flow equation (equation 14.16 in Kolditz (2002)). The concentrations of all chemical species are determined by solving the mass transport equation (equation 3.46 in Kolditz (2002)) for the components (i.e. chemical elements) followed by equilibrium calculations by the chemical solver at every node of the mesh using the result of the transported components. The equilibrated concentrations are retrieved for the next time step of mass transport calculation. In OpenGeoSys, the Boussinesq approximation is considered, i.e the density variation is neglected in the mass conservation equation of the fluid phase. Density variations are included by the buoyancy term of the Darcy equation only. For variable-density flow in porous medium the Darcy velocity $\mathbf{q}(\mathrm{m\ s^{-1}})$ is given as:

$$\mathbf{q} = -\frac{\mathbf{k}}{\mu}\left(\nabla p - \rho \mathbf{g}\right), \tag{10.2.2}$$

where $\mathbf{k}$ is the permeability tensor ($\mathrm{m^2}$), μ is the dynamic viscosity (Pa s) of fluid, ∇p (Pa) is the pressure gradient, ρ is density of fluid ($\mathrm{kg\ m^{-3}}$) and $\mathbf{g}$ is the gravity vector ($\mathrm{m\ s^{-2}}$).

Porosity, diffusivity and permeability

As a result of dissolution/precipitation reactions, porosity changes occur. Transport properties such as effective diffusion coefficients, D_e,and the permeability, k_s, of the medium are parameterized as a function of porosity.

For the dependence of the effective diffusion coefficient, D_e, on porosity we used a simplified Archie's law (Archie (1942)):

$$D_e = D_w n^m \tag{10.2.3}$$

where D_w $[\mathrm{m^2 s^{-1}}]$ is the diffusion coefficient in water, n [-] is the porosity and m [-] is an empirical coefficient. In our case m was set to 1.

Changes of permeability k_s $[\mathrm{m^2}]$ with porosity are given by a modified Kozeny – Carmen equation:

$$k_s = k_0 \left(\frac{n}{n_0}\right)^3 \tag{10.2.4}$$

where k_0 [m^2] is the initial permeability, and $w$and w_0 are the current and initial porosities, respectively.

Activity corrections

Activity coefficients for all dissolved species γ_i are calculated by the extended Debye-Hückel equation (Helgeson et al. (1981)). A detailed description is reported in Wagner et al. (2012). Equation (5) relates the activity coefficients of an aqueous ion to its charge (Z$_i$) and ionic strength (I):

$$log_{10}\gamma_i = \frac{-A_\gamma Z_i^2 \sqrt{I}}{1 + \dot{a}_i B_\gamma \sqrt{I}} + b_{\gamma_i}\ I \tag{10.2.5}$$

Where $\dot{a}_i$ (in 10^{-8} cm) is an average distance of approach of two ions of opposite charges, b_γ is a semi-empirical coefficient, either individual for a given electrolyte or common for all charged species. $\dot{a}_i$ and $b_{\gamma i}$ were set to 3.72 and 0.064 respectively for all the ionic species (Helgeson et al. (1981)). These are values for the well calibrated sodium chloride electrolyte. A_γ and B_γ are temperature dependent coefficients obtained internally from SUPCRT92 subroutines (Johnson et al. (1992)) incorporated into the GEMS code. At a temperature of 25 °C and pressure of 1 bar, $A_\gamma\ \approx 0.5114$ and $B_\gamma\ \approx 0.3288$. Activity coefficients, $\gamma_{(i)}$for neutral species (dissolved gasses) and water were set to unity.

Kinetics of precipitation and dissolution reactions of minerals

The temporal quantities of strontium and barium sulphate, and consequently also the porosity evolution, depend on the reaction kinetics. The kinetic rates dm/dt [mol s^{-1}] are calculated following Palandri and Kharaka (2004). In our simulations, the simplest reactive surface area SA [m^2] model of those implemented in OGS-GEM was chosen:

$$SA = V_i a_i \tag{10.2.6}$$

where V_i [m^3] is the volume of the mineral and a_i [m^2 m^{-3}] is the relative surface area per volume unit.

In our simulations, barium sulphate was assumed to precipitate instantaneously (very fast kinetics) and only the kinetic dissolution of strontium sulphate was taken into account. The dissolution rate of strontium sulphate at pH = 5.6 (pH of the experiment) is calculated based on the equation given in Palandri and Kharaka (2004) with parameters from Dove and Czank (1995).

$$\frac{dm}{dt} = -SA\, k^{\circ}(1 - \Omega) \tag{10.2.7}$$

where $SA[\mathrm{m}^2]$ is the reactive surface area of the strontium sulphate mineral phase, $k^{\circ} = 10^{-5.66}\mathrm{mol\ m^{-2}\ s^{-1}}$ is the dissolution rate constant at 298.15 K and Ω is the mineral saturation index.

Solid solution

A solid solution phase is defined as a mixture of solids forming a homogeneous crystalline structure. The thermodynamics of a solid solution has been described in details by Bruno et al. (2007). Briefly, the Gibbs energy of a solid solution (composed of n-components) that deviates from ideality ($\Delta G_{total}{}^{real}$), can be split into the Gibbs energy of pure end-members ($G_i{}^0 X_i$), the ideal Gibbs energy of mixing ($\Delta G_{mix}{}^{id}$), and the excess Gibbs energy of mixing (G^{ex}):

$$\Delta G^{real}_{total} = \sum_{i=1}^{n} G^0_i X_i + \Delta G^{id}_{mix} + G^{ex} \tag{10.2.8}$$

The $\Delta G_{mix}{}^{id}$ is given by the following formula:

$$\Delta G^{id}_{mix} = qRT \sum_{i=1}^{n} X_i ln X_i \tag{10.2.9}$$

where q is the site multiplicity factor and X_i the mole fraction of component i, R and T are the gas constant and temperature respectively.

The G^{ex} term depends on the mixing model of choice. In our approach, the subregular mixing model is considered (Bruno et al., 2007). The excess Gibbs energy of a binary subregular solution with component A and B mixing randomly is given by the Margules formula:

$$\Delta G^{ex} = X_A X_B (X_A w_{BA} + X_B w_{AB}) \tag{10.2.10}$$

where X_A and X_B are the molar fractions of the end-members and w_{AB} and w_{BA} are the Margules interaction parameters, $w_{AB} \neq w_{BA}$. Note that this model reduces to the regular model when $w_{AB} = w_{BA}$. The Margules parameters (in J mol^{-1}) are usually defined as linear functions of temperature, T, and pressure, P,

$$w_{AB} = w_{u,AB} - T w_{s,AB} + P w_{v,AB} \tag{10.2.11}$$

where w_u, w_s and w_v are empirical coefficients related to excess internal energy, entropy and volume of mixing, respectively. The Margules parameters w_{AB}, w_{BA} for barium and strontium sulphate solid solution at 298.15 K were set to 3787 J mol^{-1} and 3665 J mol^{-1} according to Zhu (2004). Corrections to pressure and temperature were neglected in our model.

Table 10.2.3: Thermodynamic database of aqueous, gaseous and solid species present under standards conditions.

Phase	**Component**	**Standard Gibbs energy of formation ΔG^0_f [kJ mol^{-1}]**	**Molar volume [$10^{-5} m^3 mol^{-1}$] under standard conditions**
Aqueous	$Ba(CO_3)$	-1104.251	-1.1798542
	$Ba(HCO_3)^+$	-1153.325	1.917225
	$Ba(SO_4)$	-1320.652	0.818138
	Ba^{+2}	-560.782	-1.2901389
	$BaOH^+$	-721.077	0.91585235
	$Sr(CO_3)$	-1107.830	-1.5228401
	$Sr(HCO_3)^+$	-1157.538	1.4082323
	$Sr(SO_4)$	-1321.366	0.50248447
	Sr^{+2}	-563.836	-1.7757955
	$SrOH^+$	-725.159	0.70988636
	CO_2	-386.015	3.2806681
	CO_3^{-2}	-527.982	-0.60577246
	HCO_3^-	-586.940	2.4210897
	Cl^-	-131.290	1.7340894
	H_2	17.729	2.5264358
	O_2	16.446	3.0500889
	HSO_4^-	-755.805	3.484117
	SO_4^{-2}	-744.459	1.2917656
	OH^-	-157.27	-0.470784
	H^+	0.00	0.00
	H_2O	-237.18138	1.807
Gaseous	CO_2	-394.393	2478.9712
	H_2	0.00	2478.9712
	O_2	0.00	2478.9712
Solid	$Ba(CO_3)$	-1137.634	5.03
	$BaCl_2$	-810.400	5.40
	$BaCl_2 \bullet 2H_2O$	-1296.320	8.186
	$BaCl_2 \bullet H_2O$	-1055.630	7.208
	$Ba(SO_4)$	-1362.152	5.21
	Quartz	-854.793	2.2688
	$Sr(CO_3)$	-1144.735	3.901
	$SrCl_2$	-781.10	5.194
	$SrCl_2 \bullet 2H_2O$	-1281.6798	7.283
	$SrCl_2 \bullet 6H_2O$	-2240.8033	13.814
	$Sr(SO_4)$	-1346.15	4.625

10.2.3 Results

In this part we present the reference solution for the different case studies.

Case 1

Case 1 considers the injection of a concentrated non-reacting sodium chloride solution into a porous medium initially saturated with a liquid of lower density (water). Fig. 10.2.2 compares, at different times, the experimentally observed dye tracer distribution in a highly concentrated NaCl solution (bottom figures) with results from our numerical simulations (top figures). The simulated tracer profile is in good qualitative agreement with the experimental observation. A quantitative tracer concentration comparison could not be performed because of large uncertainties on the experimental tracer concentration calibration. Fig. 10.2.3 gives the simulated breakthrough curve of the tracer at ports 'c' and 'd', and at the outlet for comparison with other transport codes.

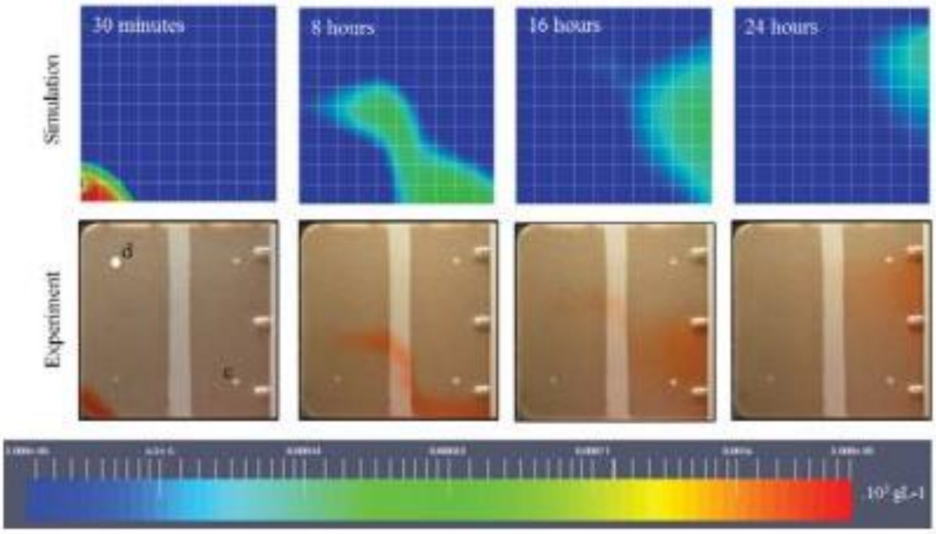

Fig. 10.2.2: The temporal evolution of the tracer profiles of the model (top) and the experiment (bottom).

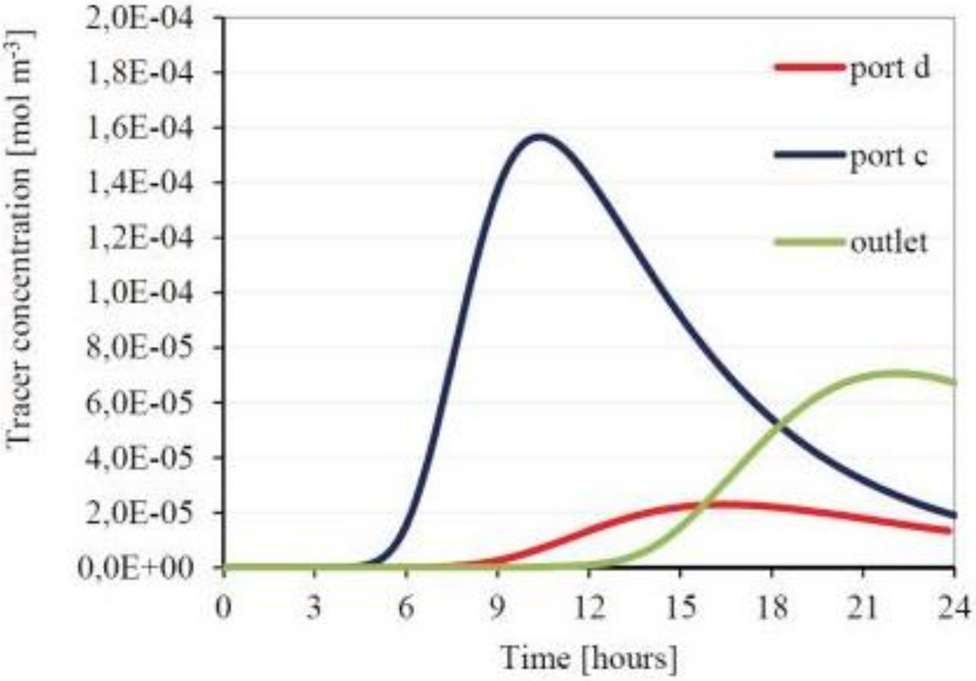

Fig. 10.2.3: The simulated tracer concentration at port 'd', 'c' and the outlet as a function of time.

Case 2

Case 2 extends Case 1 by considering dissolution and precipitation of minerals that change porosity and permeability in the flow cell. When a concentrated $BaCl_2$ solution reaches the reactive $SrSO_4$ layer Q2, the dissolution of $SrSO_4$ is triggered and barium sulphate ($BaSO_4$) precipitates. Fig. 10.2.4 shows the total amount of $BaSO_4$ and $SrSO_4$ in the flow cell with time, which changes due to either mineral dissolution or precipitation. During the first 150 hours, dissolution of $SrSO_4$ at a constant rate of 0.2 mmol per hour is observed. After 150 hours, this dissolution rate slows down. Similarly the total amount of precipitated barium sulphate increases for the first 150 hours and slowly builds up to 0.036 mol at 200 hours. The initial fast precipitation of barium sulphate for the first 150 hours results from the dissolution of the smaller strontium sulphate particles (celestite 1). As the smaller strontium sulphate grains are consumed, aqueous SO_4^{2-} is supplied by the dissolution of larger dissolution strontium sulphate (celestite 2) which is much slower due to its lower reactive surface area. The simulated results reproduced well the experimental data. In the experiments, small strontium sulphate crystals dissolved completely, while larger strontium sulphate grains were coated by a layer of barium sulphate, which prevented further dissolution. These observations

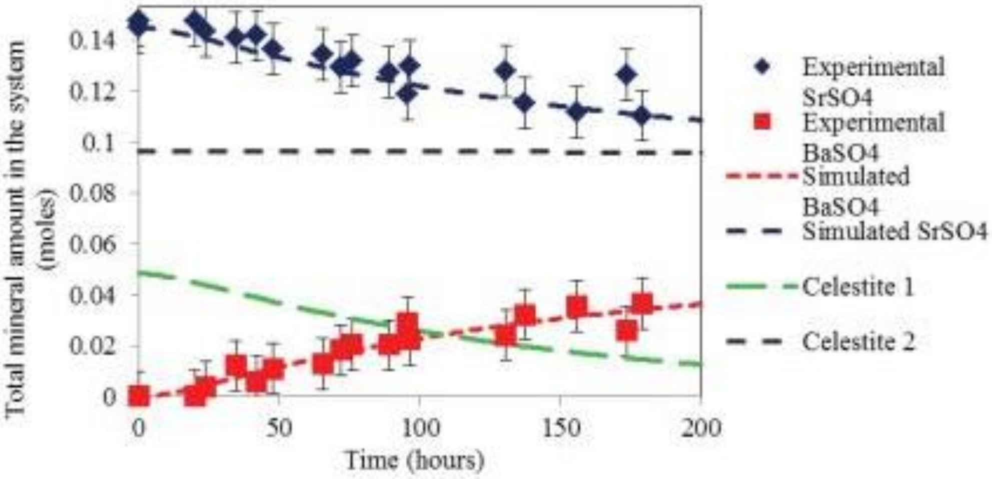

Fig. 10.2.4: Time evolution of the total bulk amount [mol] of barium sulphate and strontium sulphate in the flow cell.

were approximated in our model by applying a different reactive surface area for small and big strontium sulphate grains. The reactive surface areas attributed to celestite 1 and celestite 2 are fitted values, because the measured BET surface area overestimated strontium sulphate dissolution. The experimental observation also showed the absence of a precipitation front of barium sulphate at 200 hours. This was reproduced in our simulation as shown in Fig. 10.2.5.

The transformation of strontium sulphate to barium sulphate involves a volume increase of about 12%. The resulting porosity decrease and associated permeability changes are shown in Fig. 10.2.6. This model does not reproduce the experimentally observed 100% net pressure increase (between port

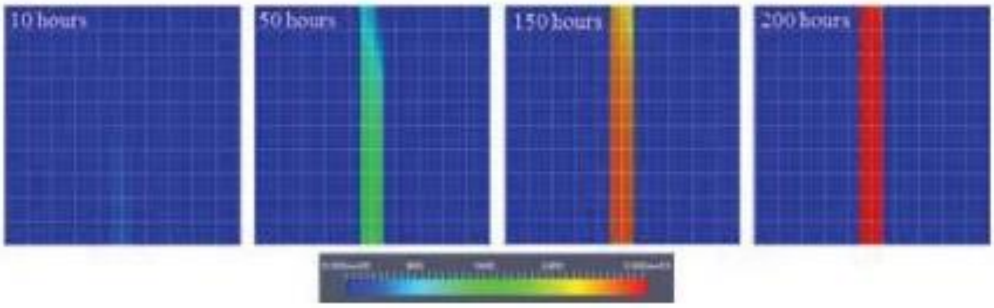

Fig. 10.2.5: Time evolution of barium sulphate profiles [mol m-3] in the flow cell.

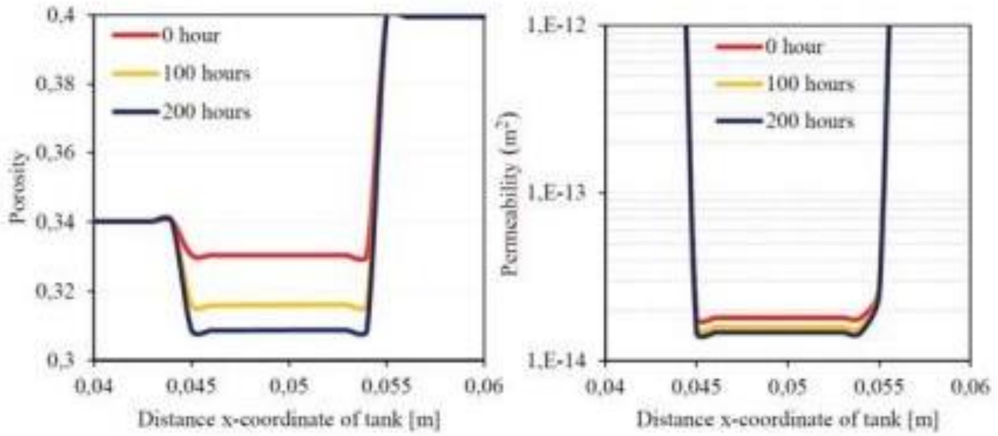

Fig. 10.2.6: Porosity (left) and associated permeability changes (right) across z = 0.01 m at 0, 100 and 200 hours.

'a' and port 'b') measured during the experiment (Poonoosamy et al., 2015), because the calculated porosity change is too small to significantly change the permeability as calculated by the Kozeny-Carman porosity – permeability relation (Equation 10.2.4). In Poonoosamy et al. (2015), a second scenario that involved the insertion of a 1mm thick zone at the quartz/ strontium sulphate interface (between the Q1 and Q2 region) with an initial lower porosity of 0.1 reproduced the experimental pressure changes. This scenario is not included here.

Fig. 10.2.7 shows the calculated and simulated ion concentrations at port 'c' and at the outlet as a function of time. Note that the uncertainties on the measured concentration at port 'c' are relatively high because it involved the sampling of small volumes of liquid (100μL) that were afterwards diluted for measurement by ion chromatography. The simulated breakthrough curves of Cl^-, Sr^{2+} and Ba^{2+} differ significantly from the experimental data. The chloride concentration of the liquid samples collected at port 'c' exceeds its injecting concentration (0.6 mol L^{-1}). This can be due to sampling artefacts at the ports. As such, the experimental ion concentrations at the port cannot be used for comparison. On the other hand, the calculated ion concentrations at the outlet are in good agreement qualitatively and quantitatively with experimental data.

Case 3

Case 3 is a hypothetical case study that considers the formation of a solid solution between barium sulphate and strontium sulphate. It still needs to be

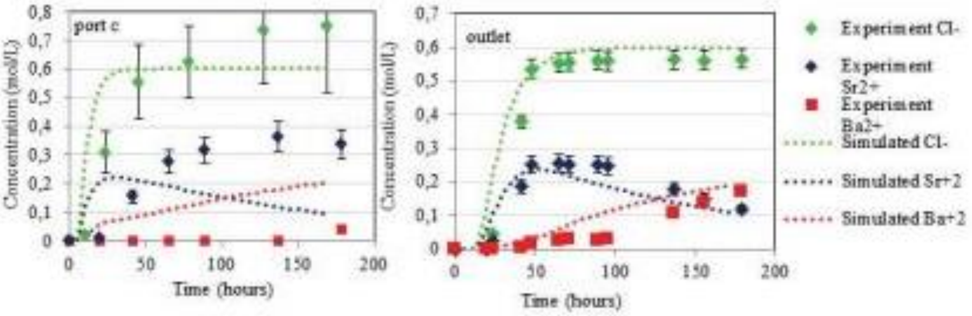

Fig. 10.2.7: Measured and calculated ion concentrations at port ‘c’ and at the outlet as a function of time.

tested experimentally. In this case, the pure mineral phase strontium sulphate is replaced by a solid solution. No pure barium sulphate phase is likely to precipitate. The injection of a solution composed of 1 mmol/L barium chloride and 99 mmol/L of strontium chloride, likely triggers a barium rich solid solution. Fig. 10.2.8 shows the total amount of mineral phases present in the flow cell with time. After 600 hours, 0.0330 mol of pure strontium sulphate phase has reacted to form 0.032 mol of a $(Sr_{1-x}Ba_x)SO_4$ solid solution. The composition of the formed solid solution changes with time. During the first 400 hours, the solid solution is enriched with barium (about 70%). Afterwards, the solid solution enriches itself in strontium (about 45% at 600 hours). This behavior is also reproduced in Fig. 10.2.8, where the total amount of the barium sulphate end member increases sharply for the first 400 hours and then only slightly increases afterwards.

Fig. 10.2.9 shows the porosity change between 0 and 600 hours and the associated permeability decrease across line $z = 0.01$m. The porosity decrease and the corresponding permeability change are negligible. It is also worth noting that for approximately the same amount of newly formed phase (0.032 mol of solid solution for Case 3 and 0.036 mol of pure barium sulphate for Case 2), the corresponding porosity decreases, and thus permeability is bigger for case 2 (1% in case 3 versus 6% in case 2). This is because the molar volume occupied by barium sulphate is higher than the molar volume of a solid solution composed of barium and strontium sulphate.

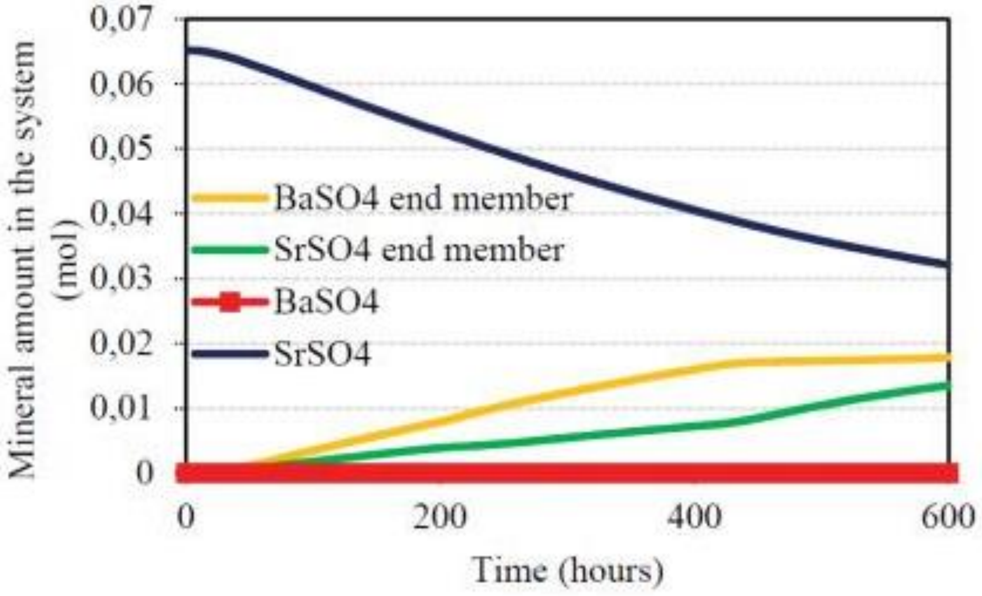

Fig. 10.2.8: The evolution of mineralogical changes in the flow cell.

10.2.4 Summary

We conducted 2D experiments to benchmark fluid flow and reactive transport calculations. Barium chloride was injected in a flow cell filled with a porous reactive layer of strontium sulphate sandwiched between two layers of inert

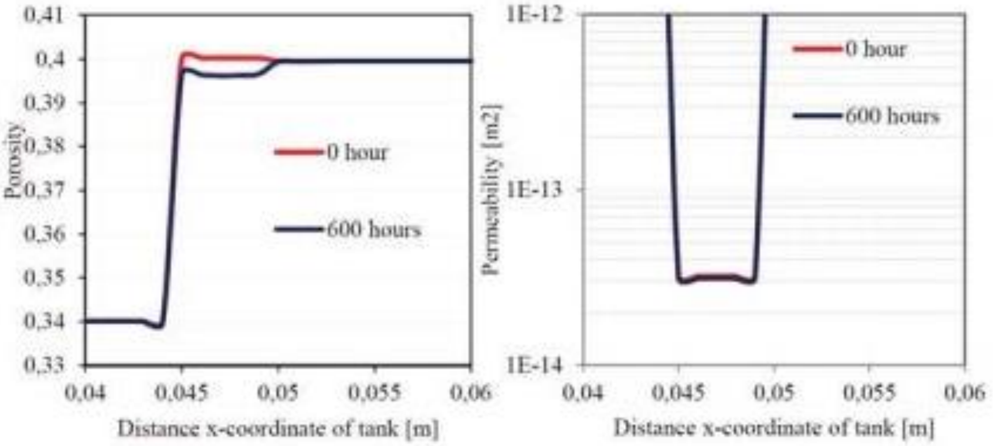

Fig. 10.2.9: Porosity (left) and associated permeability changes (right) across z = 0.01 m at 0 and 600 hours.

porous material, silicon dioxide. Our experiments are flexible enough to investigate several process couplings such as the effect of the liquid phase density on advective-diffusive transport of solutes, kinetically controlled dissolution/precipitation reactions causing porosity changes, and mineral changes involving formation of solid solution. We thus present 3 case studies with increasing level of complexity as a benchmark for reactive transport codes. In Case 1 tests with a non-reactive tracer and density-driven flow (due to the high concentration of a sodium chloride solution), were well reproduced by the numerical model. Case 2 involved the dissolution and precipitation of mineral phases that caused changes in porosity and permeability of the porous media. The presented model could reproduce well the temporal mineral bulk composition in the flow cell, but failed to reproduce the measured net pressure increase with the implemented Kozeny-Carman equation. However, by modifying the initial medium properties of the interface in the simulation, the experimental results could be fitted. This scenario described in Poonoosamy et al. (2015) is not presented here. Case 3 extends the problem of case 2 by considering the formation of a non-ideal solid solution and still needs to be verified experimentally. The presented cases are based on the benchmark study in the framework of the SeS benchmark initiative (Xie et al. (2014)).

Annex

Table 10.2.4: Equilibrium amount of solutes and phases (mol) for boundary (BC) and initial conditions (IC) for case 1.

Case 1	**Inlet_BC (mol)**	**Q1_IC (mol)**	**Q2_IC (mol)**	**Q3_IC (mol)**
$Na(CO_3)^-$	9.26E-010	8.72E-19	9.04E-19	8.72E-19
$Na(HCO_3)(aq)$	9.41E-007	1.38E-15	1.32E-15	1.38E-15
$Na(SO_4)^-$	4.74E-010	5.03E-18	2.42E-12	5.03E-18
Na^+	1.3999991	1.00E-09	9.98E-10	1.00E-09
NaOH(aq)	1.77E-009	2.69E-18	2.60E-18	2.69E-18
$Sr(CO_3)(aq)$	2.30E-018	2.99E-17	1.50E-11	2.99E-17
$Sr(HCO_3)^+$	5.82E-015	3.76E-14	1.94E-08	3.76E-14
$Sr(SO_4)(aq)$	1.33E-018	1.95E-16	4.54E-05	1.95E-16
Sr^{+2}	1.00E-009	1.00E-09	5.99E-04	1.00E-09
$SrOH^+$	3.13E-018	2.09E-17	1.09E-11	2.09E-17
$CO_2(aq)$	1.11E-005	1.36E-05	1.34E-05	1.36E-05
$CO_3{}^{-2}$	2.77E-010	4.67E-11	6.03E-11	4.67E-11
$HCO_3{}^-$	2.97E-006	2.45E-06	2.62E-06	2.45E-06
Cl-	1.4	1.00E-09	1.00E-09	1.00E-09
$H_2(aq)$	0	0.00E+00	0.00E+00	0.00E+00
tracer (aq)	0.003	1.00E-10	1.00E-10	1.00E-10
$O_2(aq)$	0.00019	2.30E-04	2.30E-04	2.30E-04
$HSO_4{}^-$	2.57E-014	2.39E-13	1.18E-07	2.39E-13
$SO_4{}^{-2}$	5.26E-010	1.00E-09	5.99E-04	1.00E-09
OH^-	4.75E-009	4.05E-09	4.39E-09	4.05E-09
H^+	3.92E-006	2.45E-06	2.52E-06	2.45E-06
$H_2O(aq)$	5.41 E+01	5.53E+01	5.53E+01	5.53E+01
CO_2	0	0.00E+00	0.00E+00	0.00E+00
O_2	0	0.00E+00	0.00E+00	0.00E+00
SiO_2	8.55E+01	8.55E+01	1.00E-09	6.47E+01
$SrCO_3$	0	0.00E+00	0.00E+00	0.00E+00
$SrCl_2$	0	0.00E+00	0.00E+00	0.00E+00
$SrCl_2.2H_2O$	0	0.00E+00	0.00E+00	0.00E+00
$SrCl_2.6H_2O$	0	0.00E+00	0.00E+00	0.00E+00
$SrSO_4$	0	0.00E+00	4.380E+01	0.00E+00

Table 10.2.5: Equilibrium amount of solutes and phases (mol) for boundary (BC) and initial conditions (IC) for case 2.

Case 2	**Inlet_BC (mol)**	**Q1_IC (mol)**	**Q2_IC (mol)**	**Q3_IC (mol)**
$Ba(CO_3)(aq)$	6.44E-10	2.42E-17	1.69E-17	2.42E-17
$Ba(HCO_3)^+$	1.24E-06	2.35E-14	1.69E-14	2.35E-14
$Ba(SO_4)(aq)$	7.33E-10	5.02E-16	1.63E-10	5.02E-16
Ba^{+2}	3.00E-01	1.00E-09	8.37E-10	1.00E-09
$BaOH^+$	7.31E-10	1.38E-17	1.01E-17	1.38E-17
$Sr(CO_3)(aq)$	2.65E-18	2.99E-17	1.50E-11	2.99E-17
$Sr(HCO_3)^+$	6.60E-15	3.76E-14	1.94E-08	3.76E-14
$Sr(SO_4)(aq)$	9.51E-19	1.95E-16	4.54E-05	1.95E-16
Sr^{+2}	1.00E-09	1.00E-09	5.99E-04	1.00E-09
$SrOH^+$	3.69E-18	2.09E-17	1.09E-11	2.09E-17
$CO_2(aq)$	1.17E-05	1.35E-05	1.34E-05	1.35E-05
$CO_3{}^{-2}$	2.28E-10	4.67E-11	6.04E-11	4.67E-11
$HCO_3{}^-$	2.97E-06	2.45E-06	2.62E-06	2.45E-06
Cl^-	6.00E-01	2.00E-09	2.00E-09	2.00E-09
$H_2(aq)$	0.00E+00	0.00E+00	0.00E+00	0.00E+00
$O_2(aq)$	2.00E-04	2.30E-04	2.30E-04	2.30E-04
$HSO_4{}^-$	1.59E-14	2.39E-13	1.18E-07	2.39E-13
$SO_4{}^{-2}$	2.67E-10	1.00E-09	5.99E-04	1.00E-09
OH^-	4.95E-09	4.06E-09	4.39E-09	4.06E-09
H^+	4.22E-06	2.45E-06	2.52E-06	2.45E-06
$H_2O(aq)$	5.50E+01	5.54E+01	5.53E+01	5.54E+01
CO_2	0.00E+00	0.00E+00	0.00E+00	0.00E+00
H_2	0.00E+00	0.00E+00	0.00E+00	0.00E+00
O_2	0.00E+00	0.00E+00	0.00E+00	0.00E+00
$BaCO_3$	0.00E+00	0.00E+00	0.00E+00	0.00E+00
$BaCl_2$	0.00E+00	0.00E+00	0.00E+00	0.00E+00
$BaCl_2.2H_2O$	0.00E+00	0.00E+00	0.00E+00	0.00E+00
$BaCl_2.H_2O$	0.00E+00	0.00E+00	0.00E+00	0.00E+00
$BaSO_4$	0.00E+00	0.00E+00	0.00E+00	0.00E+00
SiO_2	8.551E+01	8.551E+01	1.00E-09	6.657E+01
$SrCO_3$	0.00E+00	0.00E+00	0.00E+00	0.00E+00
$SrCl_2$	0.00E+00	0.00E+00	0.00E+00	0.00E+00
$SrCl_2.2H_2O$	0.00E+00	0.00E+00	0.00E+00	0.00E+00
$SrCl_2.6H_2O$	0.00E+00	0.00E+00	0.00E+00	0.00E+00
Celestite 1	0.00E+00	0.00E+00	1.466E+01	0.00E+00
Celestite 2	0.00E+00	0.00E+00	2.931E+01	0.00E+00

Table 10.2.6: Equilibrium amount of solutes and phases (mol) for boundary and initial conditions for case 3.

Case 3	**Inlet_BC (mol)**	**Q1_IC (mol)**	**Q2_IC (mol)**	**Q3_IC (mol)**
$Ba(CO_3)(aq)$	2.98E-12	1.62E-17	3.43E-18	1.63E-17
$Ba(HCO_3)^+$	5.52E-09	1.96E-14	4.20E-15	1.97E-14
$Ba(SO_4)(aq)$	1.23E-11	5.02E-16	4.78E-11	5.02E-16
Ba^{+2}	1.00E-03	1.00E-09	2.46E-10	1.00E-09
$BaOH^+$	3.33E-12	1.11E-17	2.41E-18	1.11E-17
$Sr(CO_3)(aq)$	3.65E-10	2.01E-17	1.03E-11	2.01E-17
$Sr(HCO_3)^+$	8.72E-07	3.13E-14	1.63E-08	3.15E-14
$Sr(SO_4)(aq)$	4.73E-10	1.95E-16	4.54E-05	1.95E-16
Sr^{+2}	9.90E-02	1.00E-09	5.99E-04	1.00E-09
$SrOH^+$	4.99E-10	1.68E-17	8.91E-12	1.67E-17
$CO_2(aq)$	1.25E-05	1.40E-05	1.38E-05	1.41E-05
CO_3^{-2}	1.21E-10	3.13E-11	4.17E-11	3.14E-11
HCO_3^-	2.57E-06	2.04E-06	2.21E-06	2.05E-06
Cl^-	2.00E-01	1.00E-06	1.00E-06	1.00E-06
$H_2(aq)$	0.00E+00	0.00E+00	0.00E+00	0.00E+00
$O_2(aq)$	2.52E-04	2.52E-04	2.50E-04	2.50E-04
HSO_4^-	5.00E-14	2.96E-13	1.45E-07	2.98E-13
SO_4^{-2}	5.15E-10	1.00E-09	5.99E-04	1.00E-09
OH^-	4.40E-09	3.27E-09	3.59E-09	3.25E-09
H^+	4.46E-06	3.04E-06	3.08E-06	3.06E-06
$H_2O(aq)$	5.53E+01	5.53E+01	5.53E+01	5.53E+01
CO_2	0.00E+00	0.00E+00	0.00E+00	0.00E+00
H_2	0.00E+00	0.00E+00	0.00E+00	0.00E+00
O_2	0.00E+00	0.00E+00	0.00E+00	0.00E+00
$BaSO_4$ end member	0.00E+00	0.00E+00	7.07E-10	0.00E+00
$SrSO_4$ end member	0.00E+00	0.00E+00	3.64E-06	0.00E+00
$BaCO_3$	0.00E+00	0.00E+00	0.00E+00	0.00E+00
$BaCl_2$	0.00E+00	0.00E+00	0.00E+00	0.00E+00
$BaCl_2.2H_2O$	0.00E+00	0.00E+00	0.00E+00	0.00E+00
$BaCl_2.H_2O$	0.00E+00	0.00E+00	0.00E+00	0.00E+00
$BaSO_4$	0.00E+00	0.00E+00	0.00E+00	0.00E+00
SiO_2	8.55E+01	8.55E+01	1.00E-09	6.62E+01
$SrCO_3$	0.00E+00	0.00E+00	0.00E+00	0.00E+00
$SrCl_2$	0.00E+00	0.00E+00	0.00E+00	0.00E+00
$SrCl_2.2H_2O$	0.00E+00	0.00E+00	0.00E+00	0.00E+00
$SrCl_2.6H_2O$	0.00E+00	0.00E+00	0.00E+00	0.00E+00
$SrSO_4$	0.00E+00	0.00E+00	3.24E+01	0.00E+00

Erratum

Due to an inaccuracy in GEM calculation (GEM convergence problem), errors accumulated in the mass balance conservation of case 4. This problem was solved. Fig. 10.2.8 and Fig.10.2.9 are updated below:

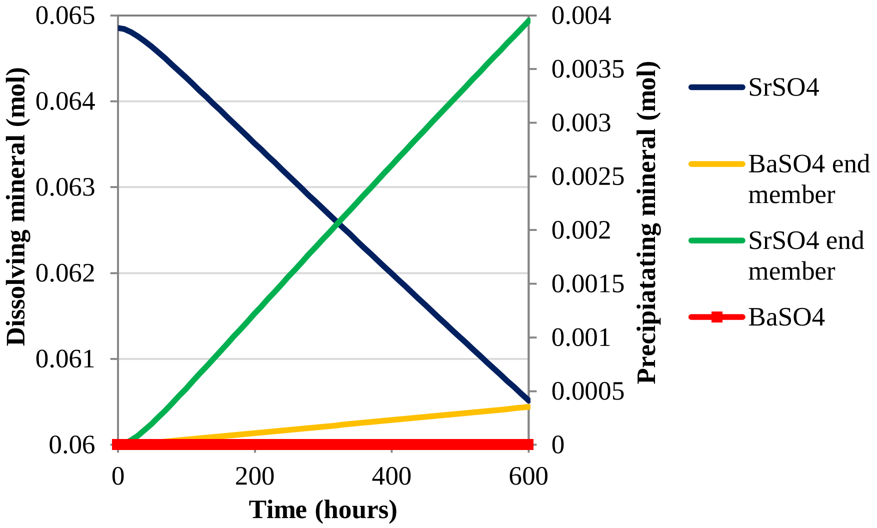

Fig. 10.2.8: Evolution of the bulk mineral composition in the flow cell with time. The left axis refers to dissolving pure celestite while the right axis refers to the precipitating phases (end members of the solid solution).

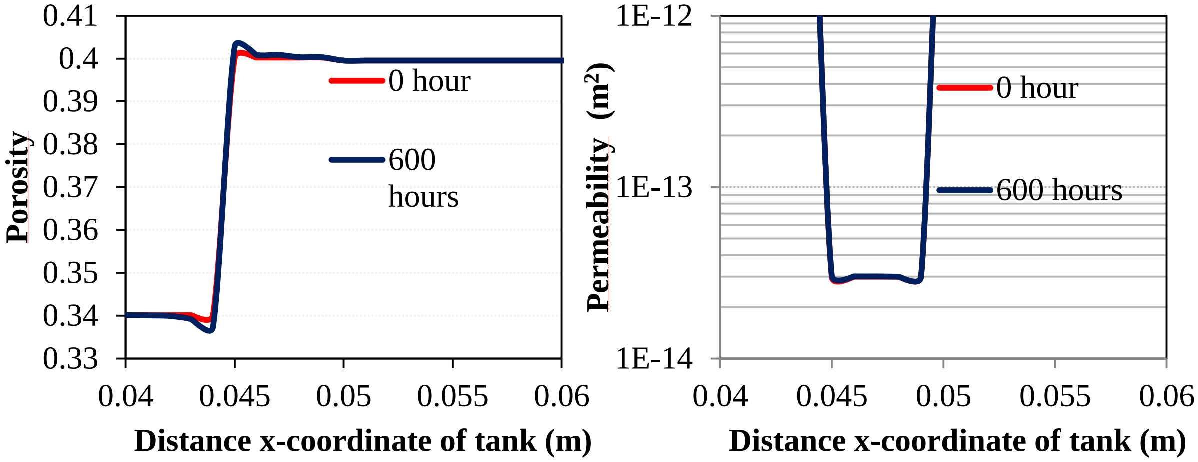

Fig. 10.2.9: Porosity (left) and associated permeability changes (right) across z = 0.01m at 0 and 600 hours.

N.B. Fig. 10.2.8 will be updated during the ‘proofreading’ before publication.

References

Archie, G., 1942. The electrical resistivity log as an aid in determining some reservoir characteristics. Trans. AIME, 146, 54-62.

Bruno, J., Bosbach, D., Kulik, D., Navrotsky, A., 2007. Chemical thermodynamics of solid solutions of interest in radioactive Waste Manage.: A state-of-the art report. Chemical Thermodynamics, 10. Eds. F.J. Mompean, M. Illemassene, J. Perrone, OECD, Issy-les-Moulineaux.

Dove, P.M., Czank, C.A., 1995. Crystal chemical controls on the dissolution kinetics of the isostructural sulfates: Celestite, anglesite, and barite. Geochim. Cosmochim. Acta, 56(10), 4147-4156.

Helgeson, H.C., Kirkham, D.H., Flowers, G.C., 1981. Theoretical prediction of the thermodynamic behaviour of aqueous electrolytes at high pressures and temperatures: Calculation of activity coefficients, osmotic coefficients, and apparent molal and standard and relative partial molal properties to 600°C and 5 KB. Am. J. Sci., 281, 1249-1516.

Hummel, W., Berner, U., Curti, E., Pearson, F.J., Thoenen, T., 2002. Nagra/PSI chemical thermodynamic data base 01/01. Universal Publishers, Parkland, Florida.

Johnson, J.W., Oelkers, E.H., Helgeson, H.C., 1992. SUPCRT92: A software package for calculating the standard molal thermodynamic properties of minerals, gases, aqueous species, and reactions from 1 to 5000 bar and 0 to 1000 °C. Computat. Geosci., 18(7), 899-947.

Kolditz, O., 2002. Computational methods in environmental fluid mechanics. Springer, Berlin.

Kosakowski, G., Watanabe, N., 2014. OpenGeoSys-Gem: A numerical tool for calculating geochemical and porosity changes in saturated and partially saturated media. Phys. Chem. Earth, 70-71, 138-149.

Kulik, D.A., Wagner, T., Dmytrieva, S.V., Kosakowski, G., Hingerl, F.F., Chudnenko, K.V., Berner, U., 2013. GEM-Selektor geochemical modeling package: revised algorithm and GEMS3K numerical kernel for coupled simulation codes. Computat. Geosci., 17(1), 1-24.

Palandri, J.L., Kharaka, Y.K., 2004. A compilation of rate parameters of water mineral interaction kinetics for application to geochemical modelling. US Geological Survey, Menlo Park, California.

Poonoosamy, J., Kosakowski, G., Van Loon L. R. and Mäder, U., 2015. Dissolution-precipitation processes in tank experiments for testing numerical models for reactive transport calculations: Experiment and modelling. J. Contam. Hydrol., 177-178, 1-17.

Shao, H., Dmytrieva, S.V., Kolditz, O., Kulik, D.A., Pfingsten, W., Kosakowski, G., 2009. Modeling reactive transport in non-ideal aqueous–solid solution system. App. Geochem., 24(7), 1287-1300.

Wagner, T., Kulik, D.A., Hingerl, F.F., Dmytrieva, S.V., 2012. GEM-Selektor geochemical modeling package: TSolMod C++ class library and data interface for multicomponent phase models. Can. Mineral., 50, 1173-1195.

Xie, M., Mayer, K.U., Claret, F., Alt-Epping, P., Jacques, D., Steefel, C., Chiaberge, C., Šimůnek, J., 2015. Implementation and evaluation of permeability-porosity and tortuosity-porosity relationships linked to mineral dissolution-precipitation. Computat. Geosci., 19, 655-671.

Zhu, C., 2004. Coprecipitation in the Barite Isostructural Family: 1. Binary Mixing Properties. Geochim. et Cosmochim. Acta, 68, 3327-3337.

Chapter 5: Dissolution precipitation reactions in a 2D setup for testing concepts of reactive transport codes

Dissolution precipitation reactions in a 2D setup for testing concepts of reactive transport codes.

Poonoosamy J.[1]., Kosakowski G.[1], Wanner C.[2], Alt Epping P.[2], Águila J. F.[3], Samper J.[3], Mäder U.[2] & Van Loon L. R.[1]

[1] Laboratory for Waste Management, Paul Scherrer Institut, CH-5232 Villigen PSI, Switzerland

[2] Rock Water Interaction, Institute of Geological Sciences, University of Bern, Baltzerstrasse 3, CH-3012 Bern, Switzerland

[3] University of La Corunã, La Corunã 15071 Spain

Keywords: density driven flow, solid solution, clogging.

1. Introduction

Water-rock interactions are important processes that govern the evolution of many natural and anthropogenic systems in the underground. These interactions include mineral precipitation and mineral dissolution, sorption processes and redox reactions. Mineral precipitation and dissolution generally modify the pore space geometry of rocks, which in turn changes flow and influences transport properties. Porosity changes induced by chemical interactions may alter the behaviour or performance of natural and engineered systems including treatment for contaminated groundwater, CO_2 storage in deep geological formations, CO_2 enhanced oil recovery in carbonate reservoirs, and also at clay/cement interfaces in high level nuclear waste repositories.

The investigation of many natural and artificial geo-systems in which the coupling of chemical reactions and transport is important is often done by means of reactive transport models because information on their geochemical evolution in space and time is scarce. Reactive transport models are numerical codes that solve a coupled set of equations which describe the transport of mobile chemical species together with a variety of geochemical reactions. However, the predictions of reactive transport codes are sensitive to the intrinsic coupling of transport and chemical operators. Application of reactive transport models includes geothermal systems (Alt-Epping et al. 2013a; 2013b; Wanner et al., 2014; Diamond and Alt-Epping, 2014), nuclear waste repositories (De Windt et al., 2004; Gaucher and Blanc, 2006; De Windt et al., 2007; Kosakowski and Berner, 2013; Berner et al. 2013), geologic carbon dioxide storage (Gauss et al., 2005; Class et al., 2009; Bildstein et al., 2010), and environmental remediation (Wanner et al., 2012; Jamieson-Hanes et al., 2012; Wanner and Sonnenthal, 2013).

There is a need to evaluate the capabilities and the correctness of the implemented features and the performance of reactive transport codes. This process is called “benchmarking” and is normally done by comparing model results with analytical solutions, by reproducing results from laboratory or field experiments and by code inter-comparison. Benchmarking with porosity enhancement, reduction or clogging is of great interest because of their strong influence on the coupling between transport and chemistry, commonly encountered in real geosystems.

Finding the exact solution for simplified 1D and 2D systems is important to test the correctness of the numerical implementation of reactive transport codes. Analytical solutions for problems coupled with porosity changes are few. The only investigations on this topic include Lagneau and van der Lee (2010), and Hayek et al., (2011, 2012). Lagneau and van der Lee (2010) proposed an analytical solution for a one dimensional system containing one species and one mineral. The analytical solution was used to verify implementation of porosity changes in the reactive transport code HYTEC (van der Lee et al., 2003). Their solution was only applicable to small and moderate porosity changes. Hayek et al. (2011) developed analytical solutions for a 1-D coupled diffusion-reaction problem with feedback on porosity change for benchmarking reactive transport. Their numerical experiment consisted in the precipitation of a solid phase from two aqueous species inside a porous medium leading to strong porosity reduction and even clogging. They proposed analytical solutions that were only suitable for non-equilibrium chemistry. Good agreement between numerical and analytical solution was obtained when sufficient spatial and temporal discretization was used for the numerical solution. Their simulation also demonstrated, in agreement with Lagneau and van der Lee (2010) that numerical codes with explicit schemes did not always converge to the analytical solution. Only implicit schemes produced accurate solutions independent of time stepping. Analytical solutions describing transport of several aqueous species coupled with precipitation and dissolution of a single mineral in two and three dimensions with porosity change were proposed by Hayek et al. (2012).

In addition, simple laboratory experiments are gaining interest for the evaluation of specific concepts for reactive transport codes. Lagneau (2000) conducted column experiments to investigate the feedback of porosity changes on transport parameters in both diffusive and advective regimes. Porosity change was forced by the injection of a reactive solution which triggered the replacement of a primary mineral phase by secondary mineral phases of larger molar volumes. The advective experiments consisted in the injection of a zinc sulphate solution into a porous medium consisting of calcite which resulted in the formation of gypsum ($CaSO_{4(s)}$) and smithsonite ($ZnCO_{3(s)}$). In the diffusive system, the porous medium was replaced by portlandite ($Ca(OH)_2$) which after reaction was transformed to gypsum and zinc hydroxide ($Zn(OH)_2$). These experiments were used to test the feedback between chemistry and transport in the reactive transport code Hytec. Similarly, Tartakovsky (2008) and Katz et al. (2011) conducted mixing-induced calcite precipitation in porous media to test the validity of using the advection-dispersion reaction equation (ADRE) for describing pore scale porosity clogging phenomena. The authors demonstrated the inappropriateness of using the ADRE for such a description. Tartakovsky (2008) proposed a modified equation of the ADRE to include transport mixing indices in the reaction terms that could account for highly non-uniform pore scale concentration gradients and localised precipitation on the sub-grid scale.

Numerical benchmarks are also used to test specific existing and new concepts of reactive transport codes. SeS Bench is an initiative for benchmarking subsurface environmental simulation methods with a current focus on reactive transport processes. Xie et al. (2015) investigated the implementation of the Kozeny-Carman equation and Archie’s law in reactive transport codes and evaluated the porosity changes due to mineral precipitation and dissolution. The benchmark considered different processes including advective-dispersive transport in saturated media, kinetically controlled mineral precipitation and dissolution leading to porosity changes, and aqueous complexation. Results from reactive transport codes (HP1, MIN3P, Pflotran and TOUGHREACT) were in good agreement, although some differences were observed for scenarios involving clogging which could be attributed to different implementations of the permeability-porosity and tortuosity-porosity relationships, the activity correction model, and numerical methods. A similar numerical benchmark involving the evaluation of transport parameters such as diffusivity and permeability due to porosity changes was also proposed by Cochepin et al. (2008). The authors forced the dissolution of portlandite followed by the precipitation of calcium oxalate due to the ingress of sodium oxalate in a 2D setup. As the oxalate has a greater molar volume than portlandite, porosity clogging is forced with such a setup. Reactive transport codes (Hytec and Crunch) that participated in the benchmark were in fairly good agreement. Discrepancies were explained by the different models used for describing the reactive surface of precipitating and dissolving minerals. It should be stressed, that it was originally planned to also experimentally implement this setup, but these plans were never realised.

We proposed a reactive transport benchmark based on experiments by Poonoosamy et al. (2015) with 4 levels of complexity. The processes included are advective-diffusive transport of solutes, effect of liquid phase density on liquid flow and advective transport, kinetically controlled dissolution/precipitation reactions causing porosity, permeability and diffusivity changes, and the formation of pure mineral phases vs. the formation of a solid solution. Compared to the existing benchmarks, the inclusion of a density driven flow and solid solution precipitation is new. In this paper, we present and analyse the results of 4 reactive transport codes (i.e. TOUGHREACT, Pflotran, CORE2D and OpenGeoSys-GEM).

2. Benchmark problem setup

The experiment on which the benchmark is based is extensively described in Poonoosamy et al. (2015). Here we summarize only the information that is important for the benchmark implementation. The experiment was conducted in a flow cell using the setup depicted in Fig. 1. It consists of a **reactive porous layer** (Q2) of celestite ($SrSO_4$) between two **inert porous layers** (Q1 and Q3) composed of quartz (SiO_2). The flow cell has dimensions of 0.1 × 0.1 × 0.01 m, and it contains several ports for fluid injection and sampling. The inlet and outlet positions were chosen to create an asymmetric flow field. Our numerical simulations are based on this setup.

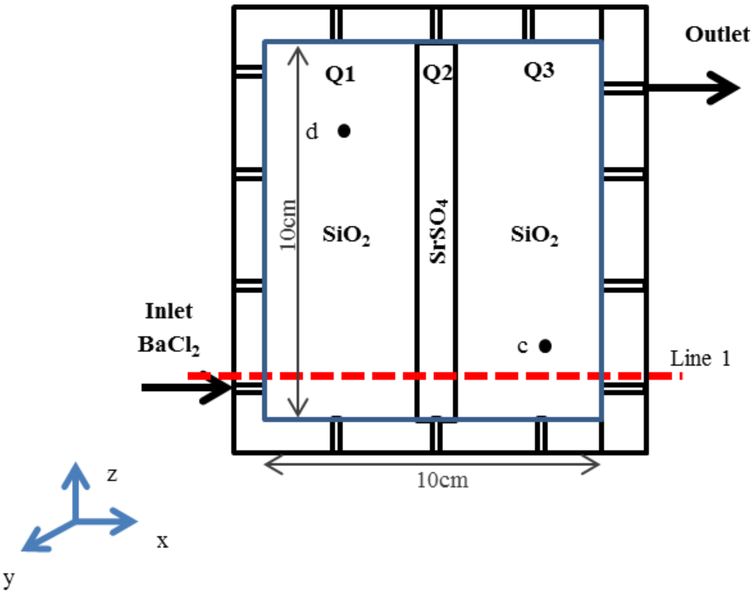

Fig. 1: Geometry of the numerical benchmark.

In Table 1, we list the properties of the different regions shown in Fig. 1 (Q1, Q2 and Q3), as well as the fluid properties and initial conditions used for the numerical calculations. The ports "c" and "d", where samples were withdrawn, are located at (0.08 m, 0.02 m) and (0.02 m, 0.08 m) respectively.

Model results are compared at the locations "c" and "d" for solute concentrations vs. time and along line 1 (z = 0.01 m) for mineral, porosity, and permeability profiles at selected times.

We define four different benchmark cases with increasing complexity. In **Case 1**, we study flow with conservative mass transport. **Case 2** extends Case 1 by considering density driven flow with conservative mass transport. In **Case 3**, we consider dissolution and precipitation of mineral phases leading to porosity changes. This case has two variants, *Case 3a* with small porosity changes and *Case 3b* with strong porosity changes. Finally, **Case 4** extends Case 3 by considering the formation of a $BaSO_4$-$SrSO_4$ solid solution. Table 2 provides additional information on the inlet and outlet conditions for the case studies. For Cases 3 and 4, density driven flow due to the injection of a concentrated solution of $BaCl_2$ was ignored, because in most codes, the fluid density is not coupled to chemical reactions.

For all simulations performed using finite element codes (OpenGeoSys-GEM, CORE2D), we considered a discretization of the square geometry in Fig. 1 by triangular or quadrilateral elements. For Cases 1, 2 and 4, a node distance of 1 mm was chosen, while for Cases 3a and 3b a more refined mesh was adopted, with a node distance of 0.5 mm for OpenGeoSys-GEM. For finite volume codes (PFLOTRAN, TOUGHREACT), the domain was discretized into rectangular grid blocks with a nodal distance of 1 mm, yielding a total number of 10000 grid blocks.

Table 1: Properties of the different regions of porous media.

Characteristics	**Q1**	**Q2**	**Q3**
Length [m] Case 1, 2 & 3a	0.045	0.01	0.045
Length [m] Case 3b and 4	0.045	0.005	0.055
Initial porosity (w_0) [-] Case 1, 2 & 3a	0.34	0.33	0.40
Initial porosity (w_0) [-] Case 3b	0.34	0.10	0.40
Initial porosity (w_0) [-] Case 4	0.34	0.40	0.40
Initial permeability k_0 [m^2] Case 1, 2 & 3a	1.82×10^{-11}	1.8×10^{-14}	1.82×10^{-11}
Initial permeability k_0 [m^2] Case 3b	1.82×10^{-11}	5.0×10^{-16}	1.82×10^{-11}
Initial permeability k_0 [m^2] Case 4	1.82×10^{-11}	3.0×10^{-14}	1.82×10^{-11}
Dispersivity α [m] Case 1 and 4	10^{-4}	10^{-4}	10^{-4}
Dispersivity α [m] Case 2, 3a, 3b	10^{-5}	10^{-5}	10^{-5}
Pore diffusion coefficient D_0 [m^{2}s^{-1}]	10^{-9}	10^{-9}	10^{-9}
Volume fraction of SiO_2 case 1, 2 3 & 4 [-]	0.66	0	0.60
Total volume fraction of $SrSO_4$ Case 1, 2 & 3a [-]	0	0.67	0
Volume fraction small $SrSO_4$ grains Case 3a [-]		0.223	
Volume fraction large $SrSO_4$ grains Case 3a [-]		0.447	
Total volume fraction of $SrSO_4$ Case 3b [-] (one $SrSO_4$ grain size only)	0	0.90	0
Total volume fraction of $SrSO_4$ Case 4 [-] (one $SrSO_4$ grain size only)	0	0.60	0
Initial pH (fixed by initial chemical set up)	5.6	5.6	5.6

N.B: In the case of CORE2D and OpenGeosys dispersivity is isotropic including longitudinal and transversal dispersive length. In Case 3a, the Q2 region is composed of bimodal grain size distribution of $SrSO_4$ crystals (mixture of large and small grains).

Case 1: Conservative mass transport.

Here we consider the injection of a non-reacting solution into the flow cell. An injection of 0.5 mL of a conservative tracer at the inlet is carried out at a rate of 20 µL min^{-1}, followed by the inflow of the solution for 24 hours. The Q2 region, composed of $SrSO_4$, is assumed to be unreactive in this case study.

The system was simulated for 24 hours.

Table 2: Characteristics of the inlet and outlet.

Characteristics	**Case 1**	**Case 2**	**Case 3a**	**Case 3b**	**Case 4**
Inlet (x=0 m; z=0.00965 m) length [m]	0.0033	0.0033	0.0033	0.0033	0.0033
Outlet (x=0 m; z=0.0902 m) length [m]	0.0033	0.0033	0.0033	0.0033	0.0033
Source term [μL min^{-1}] at inlet	20.0	20.0	20.0	20.0	10.0
NaCl concentration [mol L^{-1}] at inlet	NA	1.4	NA	NA	NA
$BaCl_2$ concentration [mol L^{-1}] at inlet	NA	NA	0.3	0.3	0.001
$SrCl_2$ concentration [mol L^{-1}] at inlet	NA	NA	NA	NA	0.099
Pressure at outlet [Pa]	101325	101325	101325	101325	101325
Amount [mL] of dye tracer injected	0.5	0.5	NA	NA	NA
Concentration of dye tracer	3gL^{-1}	3×10^{-6} molL^{-1}	NA	NA	NA
Modelling time duration [hours]	24	24	300	200	600

NA: not applicable

Case 2: Conservative mass transport coupled with a density driven flow.

The injection of a highly concentrated solution of sodium chloride into a flow cell initially saturated with water is considered. The injected solution is also saturated with respect to strontium sulfate. As in Case 1, 0.5 mL of a 3×10^{-6} M conservative tracer of molar mass of 39.948 g mol^{-1} is injected at the inlet at a rate of 20 μL min^{-1} when inflowing with a sodium chloride solution. The calculation time is set to 24 hours.

Case 3a: Mineral dissolution and precipitation with small porosity changes.

A highly concentrated solution of barium chloride ($BaCl_2$) is injected into a flow cell. The injection of $BaCl_2$ enhances the dissolution of $SrSO_4$ and causes barite ($BaSO_4$) to precipitate according to the reaction:

$$BaCl_{2(aq)} + SrSO_{4(s)} \rightarrow BaSO_{4(s)} + SrCl_{2(aq)} \qquad (1)$$

Porosity changes are likely to occur, given that $BaSO_4$ has a larger molar volume than $SrSO_4$. As a result, permeability and diffusivity will equally change.

The reactive layer Q2 has an initial porosity of 33% and is composed of two grain size populations of $SrSO_4$ (i.e., celestite 1 and celestite 2). Celestite 1 corresponds to $SrSO_4$ with a smaller grain size than celestite 2. Different kinetic rates of dissolution are used for these two grains population (see section 3.3.4.). The following reactive surface areas (per mineral volume unit) were attributed to the small and large crystals respectively: 20 000 m^2 $m^{-3}_{mineral}$ and 100 m^2 $m^{-3}_{mineral}$. We assumed no kinetic constraints on the precipitated barite ($BaSO_{4(s)}$) phase.

The simulation time is set to 300 hours.

Case 3b: Mineral dissolution and precipitation with strong porosity changes.

Case3b considers a reactive medium of celestite with an initially lower porosity of 0.1. The injection of a highly concentrated solution of barium chloride induces a stronger porosity decrease than in Case 3a. The reactive medium is composed of celestite with a single grain size population. The reactive surface area, $a_{(SrSO4)}$, is 20 000 m^2 $m^{-3}_{mineral}$.

The simulation time is set to 200 hours.

Case 4: Reactive transport involving the formation of a solid solution.

Here the reactive medium is composed of celestite with a single grain size population of 63 - 125 µm. The reactive surface area, $a_{(SrSO4)}$, is 10 000 m^2 $m^{-3}_{mineral}$. A solution composed of 0.099 mol L^{-1} $SrCl_2$ and 0.001 mol L^{-1} $BaCl_2$ is injected at the inlet at a flow rate of 10 µL min^{-1}.

The simulation time is set to 600 hours.

3. Mathematical model formulations and numerical implementations

All codes implemented the same flow and advection-dispersion equations for porous media. The generalized governing equations for multicomponent reactive transport are provided in Steefel et al. (2015) and are therefore not repeated here.

The thermodynamic data (standard Gibbs energy of formation [kJ mol^{-1}]) of aqueous, gaseous and solid species considered in our chemical system and the molar volumes [m^3 mol^{-1}] are given in Table 3.

3.1. Numerical codes

3.1.1. OpenGeoSys-GEM

The fluid flow and mass transport equations are solved by OpenGeoSys based on a standard finite element formulation, and the chemical processes by the GEMS3K kernel code of GEM-Selektor V3 (Kulik et al., 2013). The coupling of these two codes is referred to as OpenGeoSys-GEM, and its capabilities are described in Shao et al. (2009) and Kosakowski and Watanabe (2014). Mass transport and chemical reactions are solved in a sequential non-iterative approach (SNIA), i.e. the transport and reaction equations are solved separately in a sequential manner without iteration between them.

The GEM approach as implemented in GEMS3K consists of calculating the equilibrium state of a chemical system via minimization of its Gibbs free energy. The minimization is constrained by mass balance equations where the given total amounts of chemical elements are conserved. An additional charge balance equation is also imposed to enforce the electroneutrality condition of the system. The equilibrium state calculated by GEMS3K provides the mole amounts of every species in the system and the composition of all solid, liquid or gaseous phases (Wagner et al., 2012). In addition, other chemical quantities such as species activities or saturation indices that are needed for the calculation of kinetic rates of mineral dissolution are provided.

3.1.2. CORE2D

The reactive transport code CORE2D V4 is described in Samper et al. (2003). CORE2D V4 is a finite element code for modelling partly or fully saturated water flow, heat transport, and multicomponent reactive solute transport under both local chemical equilibrium and kinetic conditions (Samper et al., 2009). Coupled transport and chemical equations are solved by using the sequential iterative approach (SIA).

3.1.3. TOUGHREACT

A detailed description of TOUGHREACT and its capabilities is given in Xu et al. (2011) and Steefel et al. (2015). TOUGHREACT was developed by coupling geochemical reactions to the TOUGH2 V2 family of multiphase flow simulators (Pruess et al., 1999). The primary governing equations for multiphase fluid and chemical transport are derived from the principle of mass (or energy) conservation. The mass and energy balance equations are solved implicitly by Newton-Raphson iterations. Space discretization involves an unstructured finite volume scheme (integral finite differences). Reactive transport is solved by an operator-splitting approach that can be either iterative or non-iterative. Reactive processes considered include aqueous and surface complexation, ion exchange, mineral precipitation/dissolution, microbial mediated biodegradation, and gas exsolution/dissolution.

3.1.4. Pflotran

A detailed description of Pflotran and its capabilities is given in Lichtner et al. (2015) and Steefel et al. (2015). The reactive transport equations can be solved using either a fully implicit Newton-Raphson algorithm or the less robust operator splitting method. Reactive processes include aqueous complexation, sorption, mineral precipitation/dissolution, and microbial mediated biodegradation. Subsurface and surface flow equations are discretized using the finite volume method.

3.2. Model formulations

3.2.1. Density Flow

Three codes, namely OpengeoSys-GEM, Pflotran and TOUGH2 allow the modelling of flow influenced by the density of the liquid. In all three codes, the Boussinesq approximation is considered, i.e. the density variation is neglected in the mass conservation equation of the fluid phase. Density variations are included by the buoyancy term of the Darcy equation only. For variable-density flow in porous media the Darcy velocity $\boldsymbol{q}$ (m s^{-1}) is given as:

$$\boldsymbol{q} = -\frac{k}{\mu}(\nabla p - \rho \boldsymbol{g}), \qquad (2)$$

where k is the permeability (m^2), μ is the dynamic viscosity (Pa s) of fluid, ∇p (Pa) is the pressure gradient, ρ is the density of fluid (kg m^{-3}) and $\boldsymbol{g}$ is the gravity vector (m s^{-2}).

In OpenGeoSys-GEM the density of the aqueous phase is calculated by GEMS3K which is dependent on its molar composition. This is done by calculating the partial molar volumes of each aqueous species at the temperature and pressure of interest. Then the products of these partial molar volumes with the corresponding molar amounts of the aqueous species are summed up in order to obtain the overall volume of the aqueous phase. The total mass of the aqueous phase divided by this volume gives the density of the aqueous phase. This density is updated after each chemical equilibrium calculation and passed along to the fluid flow solver for calculation of the next time step.

In Pflotran, the mass of fluid increase in combination with the volume increase is expressed as a linear function of the total dissolved salt (TDS): $\Delta\, density = \frac{d(\, density)}{d(TDS)}$×TDS. For the calculations of Case 2 $\frac{d(\, density)}{d(TDS)}$ was set to 0.688.

It is worth noting that this formulation of density of fluid is not included in the original version of Pflotran but was implemented by the co-authors for the purpose of this work.

TOUGHREACT does not consider changes in fluid density as a function of the chemical composition. For this benchmark, flow influenced by density was therefore simulated using TOUGH2-EOS7 (Pruess et al., 1999). This equation of state represents the fluid phase as a mixture of water and brine and the salinity is described by means of the brine mass fraction X_b. In doing so, fluid density, ρ is interpolated from the values of the water (ρ_w) and brine end members (ρ_b):

$$\frac{1}{\rho} = \frac{1 - X_b}{\rho_w} + \frac{X_b}{\rho_b} \qquad (3)$$

For the simulation of Case 2, the density of the brine was set to 1057 kg m^{-3}. The diffusive flux J_D is calculated as

$$J_D = wD\rho \frac{\Delta Xb}{\Delta X} \qquad (4)$$

where D is the diffusion coefficient, ρ is the liquid density and $\frac{\Delta Xb}{\Delta X}$ is the gradient of the brine mass fraction. Equation 3 demonstrates that in TOUGH2-EOS7, the effective diffusion coefficient is not only a function of porosity and intrinsic diffusion coefficient, but also depends on the fluid density. As the fluid density is changing with time and space, the effective diffusion coefficient is not constant throughout the simulation.

3.2.2. Porosity, diffusivity and permeability

As a result of dissolution/precipitation reactions, porosity changes occur. Transport properties of the medium like effective diffusion coefficients D_e and the permeability k_s, are commonly parameterized as a function of porosity.

For the dependence of the effective diffusion coefficient on porosity we used a simplified Archie relation (Archie, 1942):

$$D_e = D_0 w^m \qquad (5)$$

where D_0 [m^2 s^{-1}] is the pore diffusion coefficient, w [-] is the porosity and m [-] is an empirical coefficient. In this study m was set to 1.

For TOUGHREACT, changes of permeability, k_s [m^2], with porosity are calculated from the Kozeny-Carman relation (Bear, 1972):

$$k_s = k_0 \frac{(1-w_0)^2}{(1-w)^1} \left(\frac{w}{w_0}\right)^3 \qquad (6)$$

For OpenGeoSys-GEM and PFlotran, changes of permeability, k_s [m^2], with porosity are given by a modified Kozeny-Carman equation:

$$k_s = k_0 \left(\frac{w}{w_0}\right)^3 \qquad (7)$$

where k_0 [m^2] is the initial permeability, and w and w_0 are the current and initial porosities, respectively.

In CORE2D, calculations are done without an update of the porosity and permeability fields, which therefore retain their initial values.

3.2.3. Activity corrections

In all participating codes, the activity coefficients for all dissolved species (γ_j) are calculated according to the extended Debye-Hückel equation (Helgeson et al., 1981). A detailed description is reported in Wagner et al. (2012). Equation 8 relates the activity coefficients of an aqueous ion to its charge (Z_j) and ionic strength (I):

$$log_{10}\gamma_j = \frac{-A_\gamma Z_j^2 \sqrt{I}}{1+\dot{a} B_\gamma \sqrt{I}} + b_\gamma \, I \qquad (8)$$

Where $\dot{a}$ (in Å) is an average distance of approach of two ions of opposite charges, b_γ is a semi-empirical coefficient, either individual for a given electrolyte or common for all aqueous species. $\dot{a}$ and b_γ were set to 3.72 and 0.064 respectively for all the ionic species (Helgeson et al., 1981). These are values for the well calibrated sodium chloride electrolyte which will also be used for the concentrated barium chloride and strontium chloride solution. A_γ and B_γ are temperature dependent coefficients obtained internally from SUPCRT92 subroutines (Johnson et al., 1992) incorporated into the GEM3K code. At a temperature of 25 ^{o}C and pressure of 1 bar, $A_\gamma \approx 0.5114$ and $B_\gamma \approx 0.3288$. Activity coefficients, γ_j for neutral species (dissolved gases) and water were set to unity.

3.2.4. Kinetics of precipitation and dissolution reactions of minerals

The transformation from celestite to barite, and consequently also the porosity evolution, does not only depend on the transport of $BaCl_2$ and the chemical reactions, the rate of transformation is also influenced by reaction kinetics. The kinetic rates, dm/dt [mol s^{-1}], are calculated following Palandri and Kharaka (2004).

In our simulations, barite was assumed to precipitate instantaneously (very fast kinetics) and only the dissolution kinetics of celestite were taken into account. The dissolution rate of celestite at pH = 5.6 (pH of the experiment) is calculated based on the equation given in Palandri and Kharaka (2004) with parameters from Dove and Czank (1995).

$$\frac{dm}{dt} = -\mathrm{SA}k^{\circ}(1 - \Omega) \qquad (9)$$

where SA [m^2] is the reactive surface area of the celestite mineral phase, $k^{\circ} = 10^{-5.66}$ mol m^{-2} s^{-1} is the dissolution rate constant at 298.15 K and Ω is the ration of ion activity product of the mineral to equilibrium constant.

In our simulations, a very simple reactive surface area *SA* model was chosen

$$\mathrm{SA} = Va \qquad (10)$$

where V [m^3] is the volume of the mineral and a [m^2 $m_{mineral}^{-3}$] is a mineral's specific surface area (i.e., surface area per volume of the mineral phase). The reactive surface area of each mineral phase was calculated using equation 10.

This approach is implemented in the reactive transport codes TOUGHREACT and Pflotran. For CORE2D, SA is the calculated initial value and remains constant during the course of the numerical experiment.

3.2.5. Solid solution

A solid solution phase is defined as a mixture of solids forming a homogeneous crystalline structure. The thermodynamics of solid solutions has been described in detail by Bruno et al. (2007). Solid solution formation is considered in Case 4 and only OpenGeoSys-GEM and Toughreact allow the calculation of solid solutions.

The Gibbs energy of an ideal solid solution (composed of n components) can be split into the weighted Gibbs energy of pure end-members ($G_i^0 X_i$) and the ideal Gibbs energy of mixing (ΔG_{mix}^{id}):

$$\Delta G_{total}^{real} = \sum_{i=1}^{n} G_i^0\, X_i + \Delta G_{mix}^{id} \qquad (11)$$

ΔG_{mix}^{id} is given by the following formula:

$$\Delta G_{mix}^{id} = \Delta H - T\Delta S = RT(X_{BaSO_4} ln X_{BaSO_4} + X_{SrSO_4} ln X_{SrSO_4}) \qquad (12)$$

where ΔH is the enthalpy of mixing (zero for ideal solid solutions), ΔS is the entropy of mixing, T is the temperature (K), R is the gas constant and X_i the mole fraction of end member *i*.

Because the formation of a solid solution increases the disorder of the crystal lattice by the random substitution of ions, the entropy term of mixing is always positive. This decreases the Gibbs energy of the ideal solid solution and favours the formation of the solid solution compared to the formation of pure phases. Fig. 2 shows the Lippmann diagram (total solubility product ($\sum\prod$) versus mole fractions of aqueous Ba^{2+} and solid $BaSO_4$) for an ideal solid solution of $BaSO_4$ and $SrSO_4$. The total solubility product ($\sum\prod$) is defined as the sum of the partial activity products contributed by the individual end members of the solid solution. In thermodynamic equilibrium, the total activity product ($\sum\prod_{eq}$) expressed as a function of solid solution composition, yields the solidus curve. Similarly, the solutus curve expresses $\sum\prod_{eq}$ as a function of the aqueous solution composition. Equations for the derivation of the solutus and solidus curves are given in the appendix. The Lippmann diagram shows that solid solution is only possible when the concentration of Ba^{2+} in solution is relatively low (indicated by the arrows). A molar aqueous fraction of Ba^{2+} ($X_{Ba2+,aq}$) above 0.05 will result in the precipitation of pure barite. Although solid solution of $BaSO_4$-$SrSO_4$ occurs in nature, the large difference in the solubility product of the end-members ($\Delta \log K \approx 3.4$), renders its formation difficult under laboratory conditions. To make Case 4 as realistic as possible, the injection of a solution consisting of a mixture of Ba^{2+} and Sr^{2+} (with respective molar fractions of 0.01 and 0.99) was considered to trigger the formation of a solid solution.

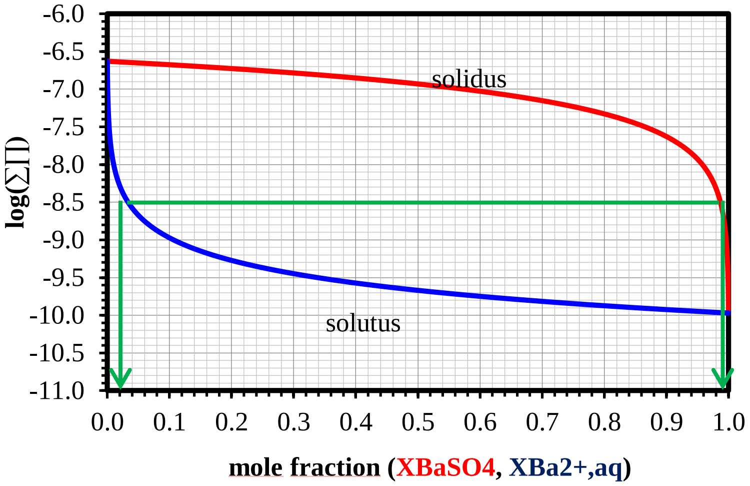

Fig. 2: Lippmann diagram of an ideal solid solution of $SrSO_4$ and $BaSO_4$.

In GEMS, the Gibbs energy of mixing is considered in the evaluation of equilibrium concentrations.

In TOUGHREACT the ideal solid solution model is only available for minerals that react under kinetic constraints.

The overall precipitation rate of the solid solution, r_{ss}, is the sum of precipitation rates of the two end-members (Wanner et al., 2015).

$$r_{ss} = r_{SrSO_4} + r_{BaSO_4} \qquad (13)$$

The precipitation rates r_{SrSO_4} and r_{BaSO_4} of the end-members are calculated according to:

$$r_{SrSO_4} = A_{ss}.k_{ss}.\left(1 - \frac{Q_{SrSO_4}}{K_{SrSO_4}}\right) + A_{ss}.k_{ss}.(x_{SrSO_4} - 1) \qquad (14)$$

$$r_{BaSO_4} = A_{ss}.k_{ss}.\left(1 - \frac{Q_{BaSO_4}}{K_{BaSO_4}}\right) + A_{ss}.k_{ss}.(x_{BaSO_4} - 1) \qquad (15)$$

where A_{ss} ($m^2\ kg_{H2O}^{-1}$) refers to the reactive surface area of the solid solution, k_{ss} is the reaction rate constant of the solid solution ($mol\ kg^{-1}\ m^{-2}\ s^{-1}$), Q_{SrSO_4} and Q_{BaSO_4} are the ion activity product of the $SrSO_4$ and $BaSO_4$ minerals, K_{SrSO_4} and K_{BaSO_4} are the corresponding equilibrium constants, and x_{SrSO_4} and x_{BaSO_4} are the mole fractions of the precipitating end-members. The first terms in equations 14 and 15 refer to the precipitation of the end members as pure minerals (i.e., maximum rate). The second terms ensure that the precipitation rates of the end-members decrease linearly with decreasing mole fractions (as $x_{BaSO_4} - 1 < 0$).

To ensure that the volume ratios of these end-members reflect the fluid composition, x_{SrSO_4} and x_{BaSO_4} are calculated according to

$$x_{SrSO_4} = \frac{Q_{SrSO_4}/K_{SrSO_4}}{Q_{SrSO_4}/K_{SrSO_4} + Q_{BaSO_4}/K_{BaSO_4}} \qquad (16)$$

$$x_{BaSO_4} = \frac{Q_{BaSO_4}/K_{BaSO_4}}{Q_{SrSO_4}/K_{SrSO_4} + Q_{BaSO_4}/K_{BaSO_4}} \qquad (17)$$

In order to get a saturation index of the solid solution that is very close to zero within Q2, which is what is calculated by OpenGeosys-GEM, the corresponding surface area (A_{ss}) and rate constant (k_{ss}) were set to 5 957 $m^2\ kg_{H2O}^{-1}$ (10 000 $cm^2\ g_{mineral}^{-1}$) and 1×10^{-5} mol $Kg^{-1}\ m^2\ s^{-1}$, respectively to ensure fast precipitation.

Table 3: Thermodynamic database of aqueous, gaseous and solid species present under standards conditions for OpenGeoSys-GEM.

Phase	**Component**	**Standard Gibbs energy of formation ΔG^0_f [kJ mol^{-1}]**	**Molar volume [10^{-5} m^3 mol^{-1}] under standard conditions**
Aqueous	$Ba(CO_3)$	-1104.251[a]	-1.1798542[c]
	$Ba(HCO_3)^+$	-1153.325[a]	1.917225[c]
	$Ba(SO_4)$	-1320.652[a]	0.818138[c]
	Ba^{+2}	-560.782[b]	-1.2901389[b]
	$BaOH^+$	-721.077[a]	0.91585235[b]
	$Sr(CO_3)$	-1107.830[a]	-1.5228401[c]
	$Sr(HCO_3)^+$	-1157.538[a]	1.4082323[c]
	$Sr(SO_4)$	-1321.366[a]	0.50248447[c]
	Sr^{+2}	-563.836[b]	-1.7757955[b]
	$SrOH^+$	-725.159[a]	0.70988636[b]
	CO_2	-386.015[a]	3.2806681[d]
	CO_3^{-2}	-527.982[a]	-0.60577246[b]
	HCO_3^-	-586.940	2.4210897[b]
	Cl^-	-131.290[a]	1.7340894[b]
	H_2	17.729[a]	2.5264358[d]
	O_2	16.446[a]	3.0500889[d]
	HSO_4^-	-755.805[a]	3.484117[b]
	SO_4^{-2}	-744.459	1.2917656[b]
	OH^-	-157.27[a]	-0.470784[b]
	H^+	0.00	0.00
	H_2O	-237.18138[c]	1.807[c]
Gaseous	CO_2	-394.393[a]	2478.9712[e,f]
	H_2	0.00[a]	2478.9712[e,f]
	O_2	0.00[a]	2478.9712[e,f]
Solid	$Ba(CO_3)$	-1137.634[a]	5.03[c]
	$Ba(SO_4)$	-1362.152[a]	5.21[g]
	Quartz	-854.793[a]	2.2688[g]
	$Sr(CO_3)$	-1144.735[a]	3.901[g]
	$Sr(SO_4)$	-1346.15[a]	4.625[g]

The standard Gibbs energy of formation [kJ mol-1] were calculated from the equilibrium constants reported in “a” and “b” corresponding to Hummel et al. (2002) and Shock et al. (1997) respectively. “c” “d”, “e” and “f” are references from Sverjensky et al. (1997), Shock et al. (1989), Wagman et al. (1982), Kelley (1960) and Helgeson et al. (1978), respectively.

4. Results

4.1. Case 1

Case 1 considers the injection of a non-reacting solution into a porous medium saturated with water. The flow field is visualized by the addition of a tracer pulse at the inlet. The temporal tracer profiles are shown in Fig. 3. At the beginning of the simulation, concentric circles of the tracer are observed. The circles get slightly distorted as the fluid moves towards a region of lower permeability (celestite layer) as shown by the picture taken after 8 hours. The simulated tracer profiles of OpenGeoSys, CORE2D, TOUGHREACT and Pflotran are visually in good agreement (only the tracer profile of CORE2D is presented below).

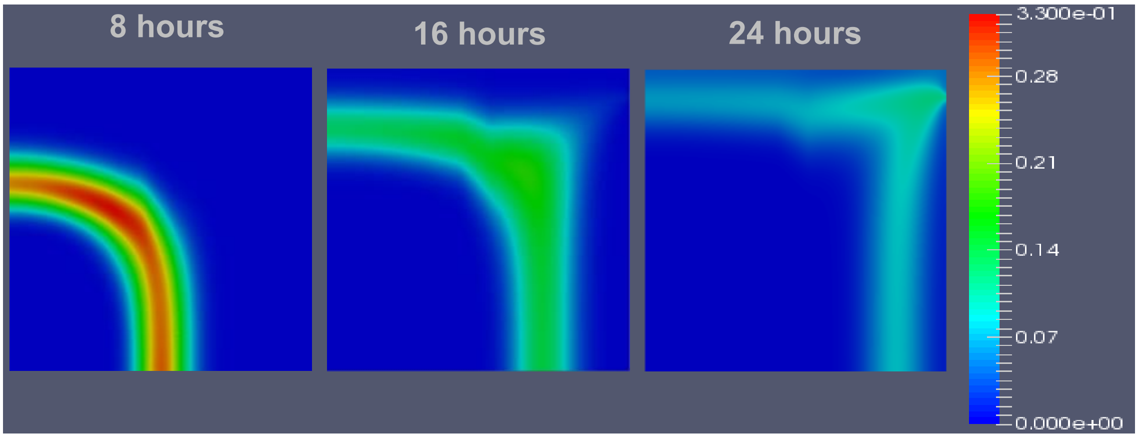

Fig. 3: Temporal tracer profile produced by CORE2D. A scale ranging from 0 to 0.33 g L^{-1} is used here for all temporal profiles.

The temporal evolution of the total amount of tracer in the flow cell is shown in Fig. 4. For the first 8 hours the amount of tracer present inside the flow cell is constant. Afterwards, there is a constant decrease ~ -5.2 × 10^{-4} g h^{-1} (1.4×10^{-7} g s^{-1}) in the total amount of the tracer as the front moves towards the outlet. After 18 hours, the decrease is more pronounced ~ -2.1 × 10^{-3} g h^{-1} (5.8×10^{-7}g s^{-1}) as the fluid from the two corners merges to the outlet. The different codes produced the same result.

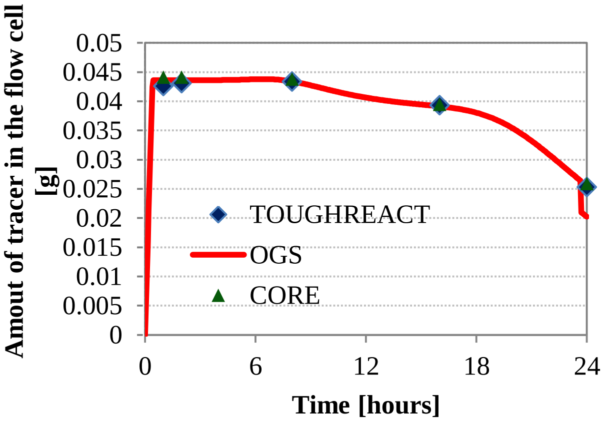

Fig. 4: The evolution of the total amount of tracer [g] in the flow cell with time.

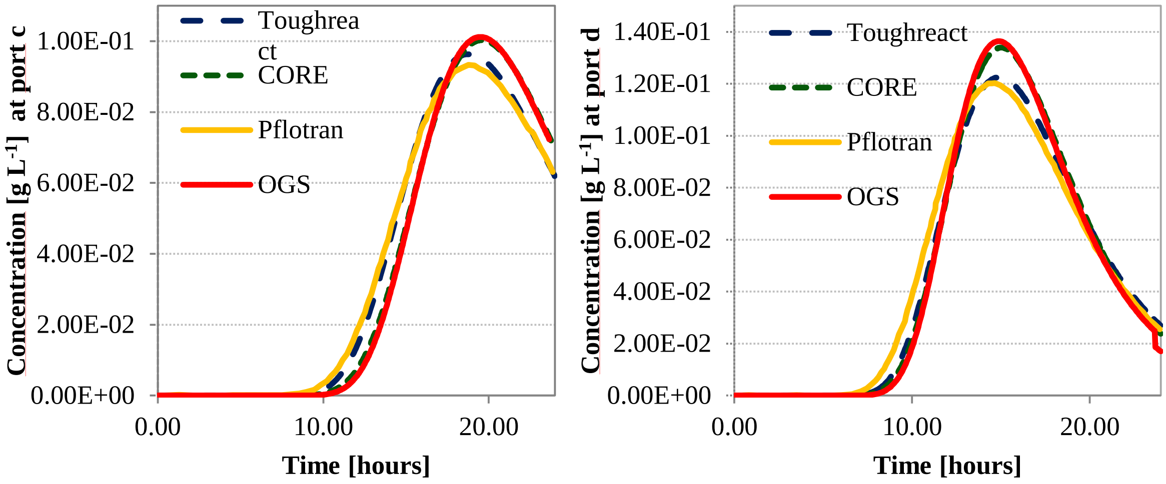

Fig. 5: Concentration of tracer measured at ports ‘c’ (left) and ‘d’ (right) at different times.

In addition, the calculated breakthrough curves of the tracer at ports “c” and “d” are shown in Fig. 5. In the case of OpenGeoSys, both triangular and quadrilateral mesh discretization were tested. Both resulted in the same tracer distribution profiles.

The simulated tracer nodal concentrations of TOUGHREACT and PFlotran differ from those produced by OpenGeoSys and CORE. The reason for this difference is not completely clear, but several possible differences in the model setup could be identified, which will be discussed as follows.

Fig. 6 compares the spatial differences in velocity magnitudes in the flow cell produced by OpenGeoSys and TOUGHREACT. The velocities of OpenGeoSys were used as reference for the calculation of the relative difference in velocity magnitude. The differences in velocity magnitude are observed at the inlet, outlet and the boundaries of the Q2 region.

The resulting difference in the flow fields observed was first attributed to the number of nodes considered at the inlet for the injection of the fluid. OpenGeoSys distributes the injection of the fluid evenly across 4 nodes while for TOUGHREACT only one side of an element volume is considered. In the case of TOUGHREACT, this could result in an increase in velocity in the x-direction which leads to differences in tracer distribution. Fig. 7 shows the relative difference in tracer concentration (g L^{-1}) between TOUGHREACT and OpenGeoSys after 1 hour of fluid injection. As such, a sensitivity analysis on changing the number of nodes over which fluid injection is distributed at the inlet was tested with TOUGHREACT. However, the effect on the results was insignificant (not visible in direct comparison plots).

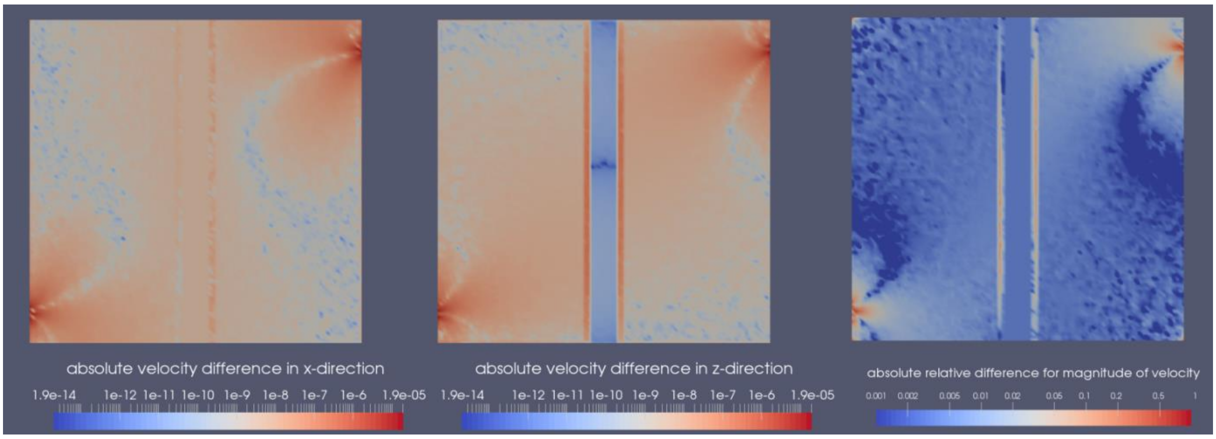

Fig. 6: Absolute velocity differences in x-direction, z-direction and magnitude of velocity (from left to right) between TOUGHREACT and OpenGeoSys.

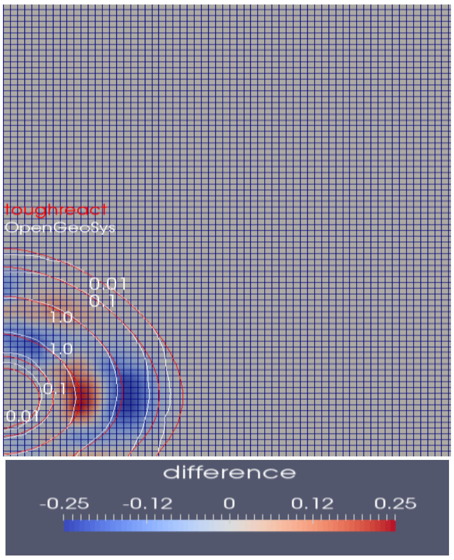

Fig. 7: Difference in tracer distribution between TOUGHREACT and OpenGeoSys after 1 hour of fluid injection.

A difference in the implementation of diffusive-dispersive transport was found. For OpenGeoSys and CORE2D the longitudinal and transversal dispersivity was set to the same value. In PFlotran only longitudinal dispersivity was considered, which results in areas with high velocities, a significant lower transversal dispersion. Test calculations with PFlotran using a 2 times higher diffusion coefficient gave breakthrough curves similar to those for OpenGeoSys. Last but not least, the intrinsic properties of the finite element and finite volume methods in solving the ADE equation might result in different values for numerical dispersion and influence the breakthrough curves. The effect of grid discretization for FE codes was tested and indicated that numerical dispersion is reduced for finer grids. The results from calculations with CORE2D are given in Fig. 18 in the appendix.

Overall, the breakthrough curves indicate that the evolution of the system is consistently described by all four codes, showing the maximum peaks between 18.5 and 19.4 hours for port ‘c’ and between 14.4 and 14.6 hours for port ‘d’.

4.2. Case 2

Case 2 considers the injection of a non-reacting saline solution into a porous medium initially filled with a liquid of lower density. This induces a transient flow regime, typical for density driven flow. On the long term the flow converges again to the stationary flow regime of Case 1. The tracer profiles shown in Fig. 8 allow the visualization of the evolution of a tracer pulse which was injected together with the $BaCl_2$ solution at the beginning of the experiment. This case was solved by the reactive codes Pflotran, TOUGH2 and OpenGeoSys-GEM.

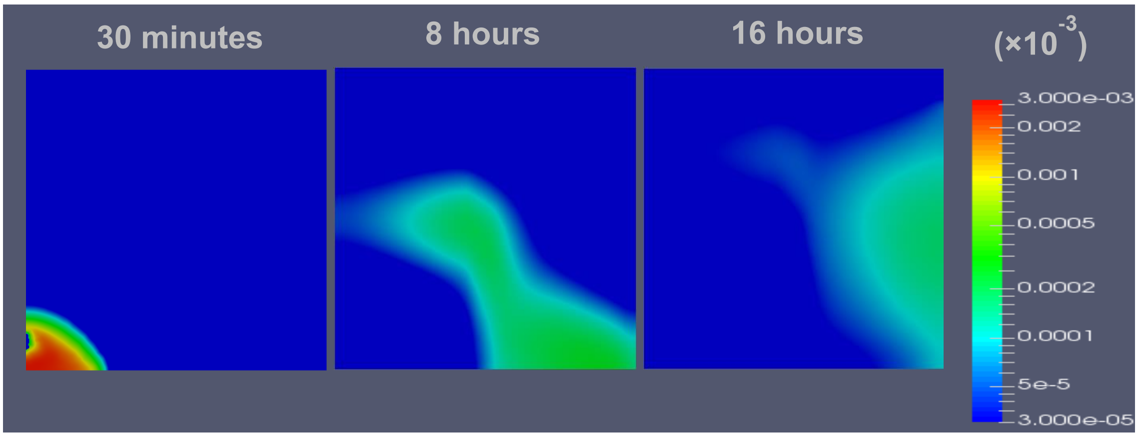

Fig. 8: Temporal tracer profiles produced by OpenGeoSys-GEM. The temporal profiles are mapped with a log scale with 3×10^{-11} mol L^{-1} and 3×10^{-6} mol L^{-1} as minimum and maximum.

Fig. 9 compares the fluid densities at ports “c” and “d” between OpenGeoSys, Pflotran and TOUGHREACT. In OpenGeoSys-GEM, the density of the fluid is calculated as the ratio of mass to volume of the fluid. The volume of the fluid is calculated based on the aqueous species present and the molar volumes of these aqueous species. As such, the volume of the fluid increases as salinity increases. The densities calculated by Pflotran being a linear function of total dissolved salts and OpenGeoSys-GEM are in qualitatively good agreement.

The fluid density correlates with the NaCl concentration. The NaCl breakthrough at the ports ‘c’ and ‘d’ showing similar trends as the fluid density (in Fig. 9) are thus not presented. The calculated NaCl concentrations (fluid densities) measured at ports ‘c’ and ‘d’ by TOUGH2 differ from those calculated by PFlotran and OpenGeoSys-GEM. As mentioned earlier, in TOUGH2, the effective diffusion coefficient is not only a function of porosity and intrinsic diffusion coefficient, but also depends on the density of the liquid. Therefore it is not constant throughout the experiment. The diffusion coefficient used for the calculations with TOUGH2 was set to 3×10^{-9} m^2 s^{-1} in order to approximate the constant value used by the other codes.

The breakthrough curves of NaCl (fluid density) at port ‘c’ and ‘d’ of OpenGeoSys-GEM and Pflotran in Fig. 9 show a similar trend. A higher dispersion is observed with OpenGeoSys-GEM. A refined spatial discretization and a Crank-Nicolson scheme were tested for OpenGeoSys-GEM, but similar results were obtained. As in Case 1, the differences between the breakthrough curves can be explained by a difference in the implementation of diffusive-dispersive transport. With OpenGeoSys-GEM, both longitudinal and transverse dispersive lengths of 1×10^{-5} m were considered, whereas with Pflotran a longitudinal dispersive length of 10^{-4} m was used.

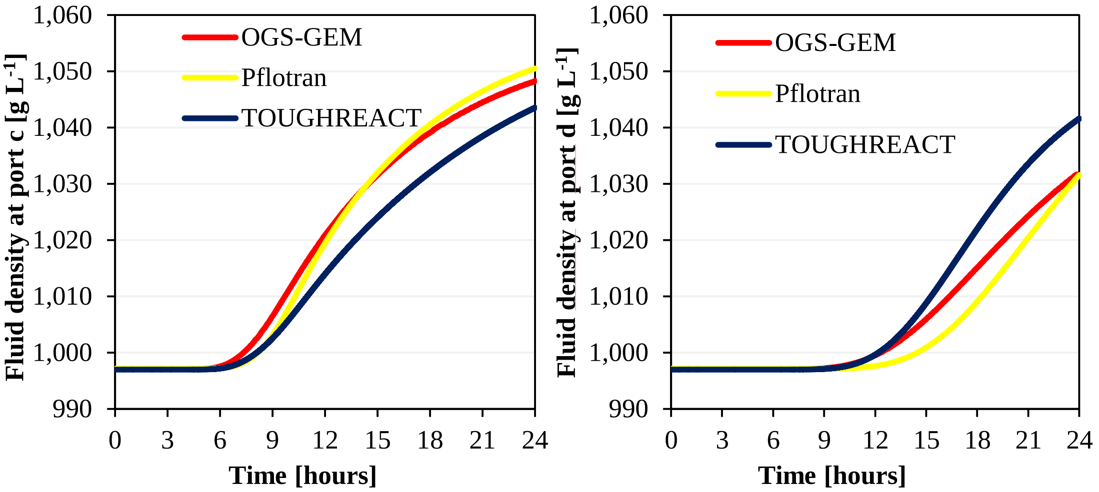

Fig. 9: Evolution of fluid density at ports ‘c’ (left) and ‘d’ (right) with time.

4.3. Case 3a

Case 3a extends Case 1 by considering dissolution and precipitation of minerals that change porosity and permeability (and the effective diffusion coefficient) in the flow cell. When a concentrated $BaCl_2$ solution reaches the reactive $SrSO_4$, layer Q2, the dissolution of celestite ($SrSO_4$) is triggered and barite ($BaSO_4$) precipitates. Fig. 10 shows the total amounts of $BaSO_4$ and $SrSO_4$ in the flow cell with time, which change due to either mineral dissolution or precipitation. During the first 150 hours, dissolution of $SrSO_4$ at a constant rate of 0.2 mmol per hour is observed. After 150 hours, this dissolution rate slows down. Similarly, the total amount of precipitated barite increases during the first 150 hours and slowly builds up to 0.043 mol at 300 hours. The initial fast precipitation of barite during the first 150 hours results from the dissolution of the smaller celestite particles (Cls 1). As the smaller celestite grains are consumed, aqueous SO_4^{2-} is supplied by the dissolution of larger grains of celestite (Cls 2) which is much slower due to its lower reactive surface area.

The total mineral dissolution and precipitation calculated with CORE2D differs from that of OpenGeoSys-GEM and TOUGHREACT. CORE2D considers a constant reactive surface area for small and large celestite crystals. In addition, CORE2D does not update the porosity for each time step; therefore also the permeability and diffusivity remain constant during the course of the simulation. This example also stresses the importance of the reactive surface area models during mineral dissolution and precipitation reactions in porous media. The results produced with an assumed constant reactive surface area are significantly different from the experimental results reported in Poonoosamy et al. (2015).

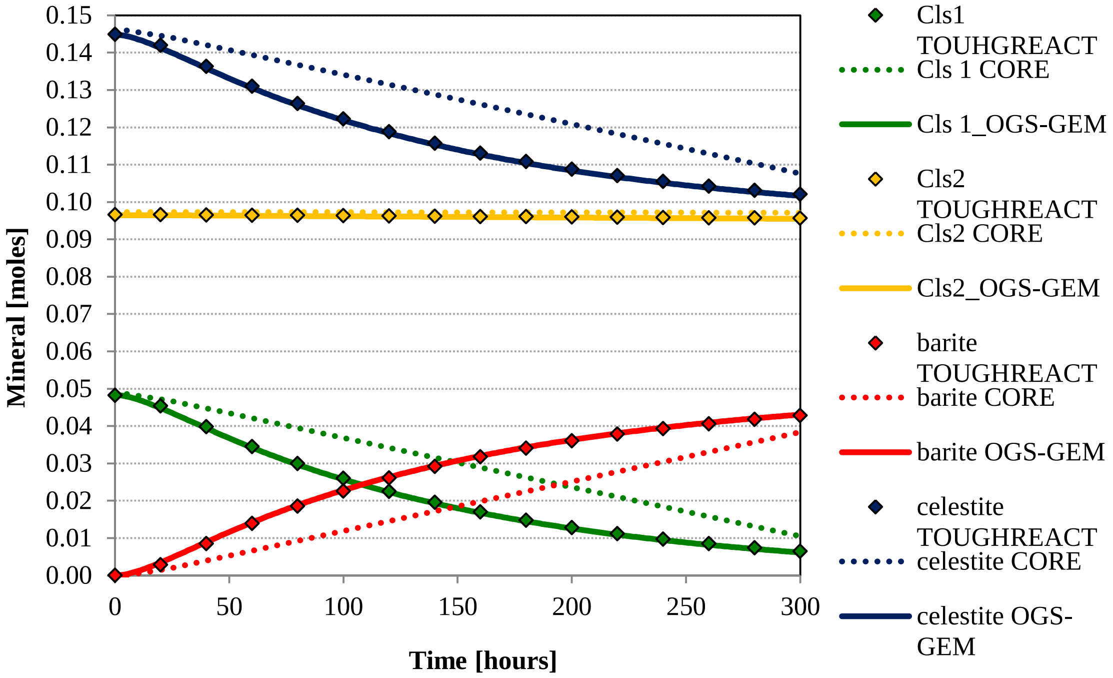

Fig. 10: Evolution of the bulk mineral composition in the flow cell with time.

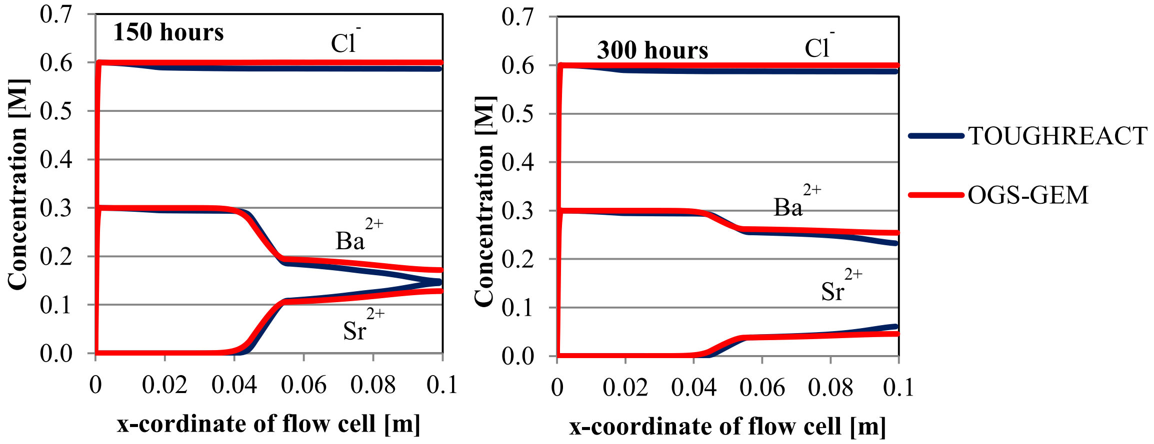

Fig. 11: Ionic concentrations measured across line 1 (z = 0.01 m) at 150 and 300 hours.

Fig. 11 compares the concentrations of major aqueous species across line 1 (Fig. 1) at 150 and 300 hours. Overall, the simulated concentrations match well although minor deviations are observed at greater distances from the inlet. It is difficult to pinpoint the exact cause for these differences, as they may be related to several reasons including differences in the implementation of diffusive-dispersive transport (as reported for Case 1), variations in the implementation of transport schemes, differences in time stepping, small deviations in databases due to the use of different components and differences in coupling schemes between transport and reactions.

The transformation of celestite to barite involves a volume increase of about 12%. The resulting porosity decrease and associated permeability changes are shown in Fig. 12. The porosity changes due to mineral transformation calculated by OpenGeoSys-GEM and TOUGHREACT are the same. The associated changes in permeability simulated by TOUGHREACT and OpenGeoSys-GEM due to the small porosity decrease (6%) are in good agreement. There are small deviations between the porosity and permeability at the interfaces between OpenGeosys-GEM and Thoughreact which are explained by the different spatial discretization used by the two codes and the processing of the results using the software ParaView (www.paraview.org/).

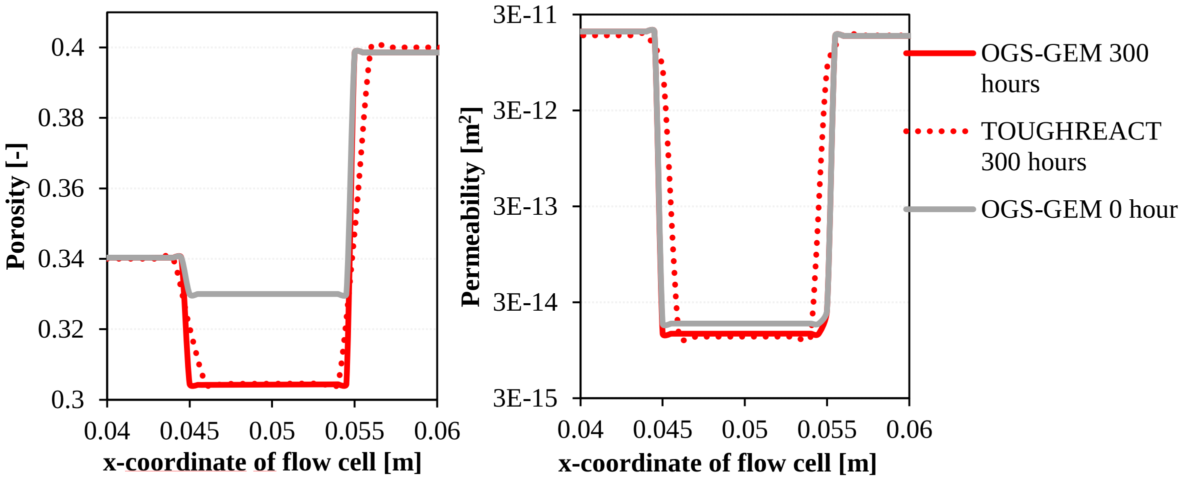

Fig. 12: Calculated porosity change (left) and permeability change (right) along line 1.

4.4. Case 3b

Case 3b is similar to Case 3a but considers a stronger change in porosity due to mineral dissolution/precipitation. This was implemented as only small grained $SrSO_4$ crystals were considered which results in a generally faster dissolution of celestite within the time window considered. After 200 hours of $BaCl_2$ injection, about 60 % of $SrSO_4$ was converted to $BaSO_4$ leading to localized clogging. Fig. 13 compares the evolution of the bulk mineral composition with time in the flow cell as calculated by TOUGHREACT and OpenGeoSys-GEM. The results of the two codes are in nearly perfect agreement.

Fig. 14 compares the simulated concentrations of major aqueous species measured across line 1 at 100 and 200 hours. The results from TOUGHREACT and OpenGeoSys-GEM are qualitatively in good agreement. As for Case 3a, some discrepancies exist between the two codes which can be explained by the differences in the implementation of diffusive-dispersive transport.

The associated porosity and permeability decrease induced by the mineral transformation along line 1 is shown in Fig. 15. Calculated porosities and permeability profiles are very similar. Differences can be explained by the different formulations of the relationship between porosity and permeability implemented in the two codes (equations 5 and 6). These differences become more pronounced as porosity decreases.

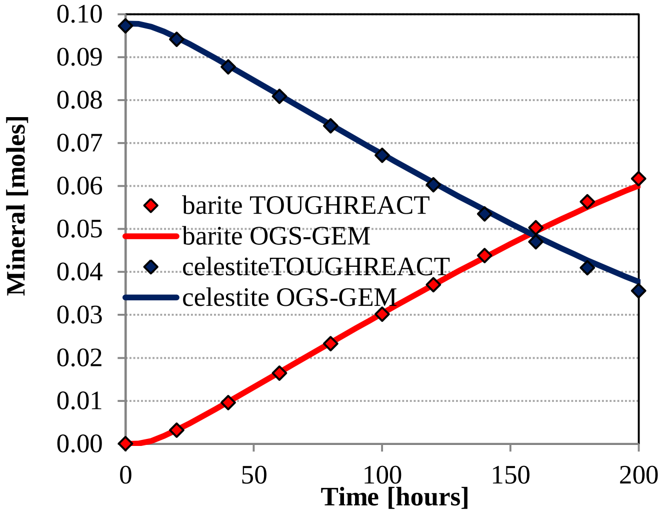

Fig. 13: Evolution of the bulk mineral composition in the flow cell with time.

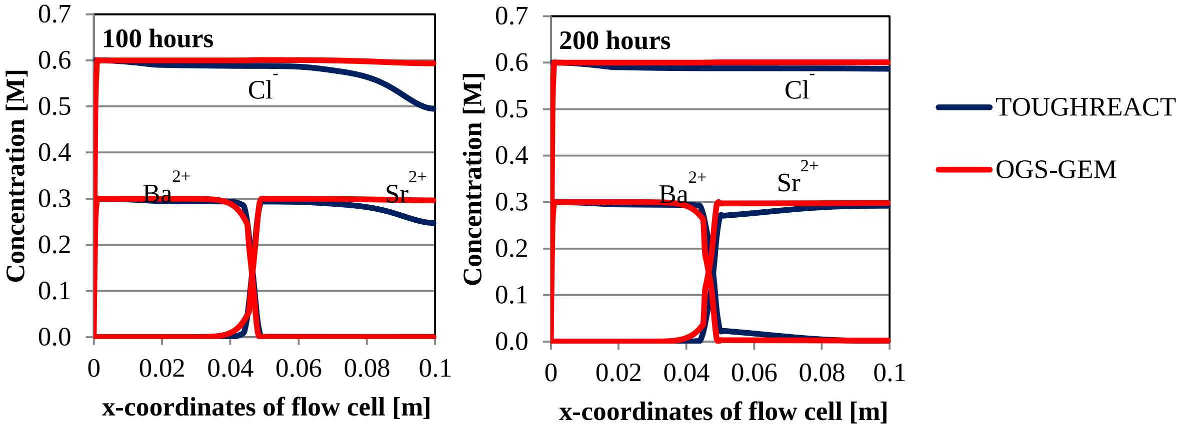

Fig. 14: Ionic concentrations measured across line 1 (z = 0.01 m) at 100 and 200 hours.

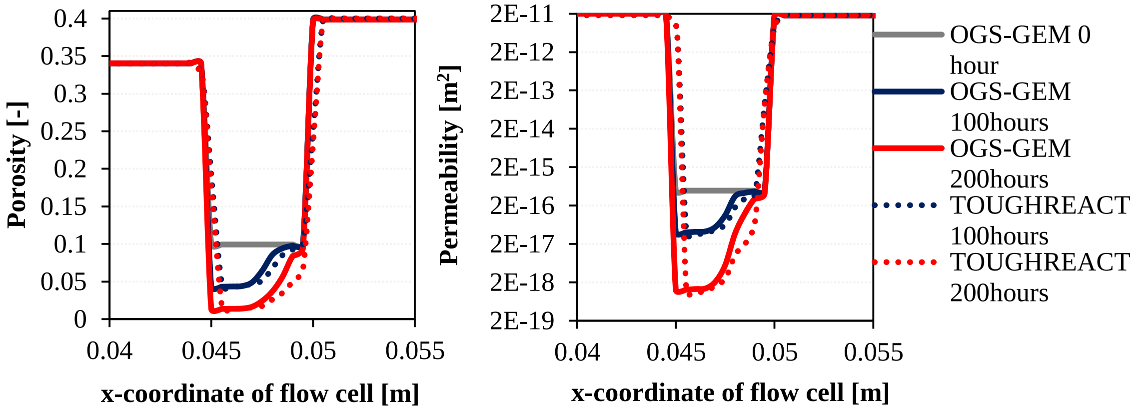

Fig. 15: Calculated porosity change (left) and permeability change (right) along line 1.

4.5. Case 4

In this case, the precipitation of a $SrSO_4$-$BaSO_4$ solid solution is considered instead of pure $BaSO_4$, which was the case for Case 3. The injection of a solution composed of 0.001 mol L^{-1} barium chloride and 0.099 mol L^{-1} of strontium chloride is likely to produce a solid solution. When no Ba^{2+} is present, $SrSO_4$ exists as a pure celestite phase. When the concentration of Ba^{2+} exceeds the solubility of the solid solution, a solid solution having a greater stability compared to the pure barite phase (higher solubility compared to solid solution) will be formed preferentially. The transformation to a solid solution is kinetically controlled by the dissolution of the initial pure celestite phase.

Fig. 16 shows the total amount of mineral phases present in the flow cell as a function of time. Although the temporal evolution of the system calculated by OpenGeosys-Gem and TOUGHREACT are qualitatively in good agreement, there are differences in the composition of the solid solution calculated by each code. Fig. 17 shows the molar amounts of the barium and strontium end members in the solid solution formed across line 1 at 600 hours.

In GEM, the thermodynamic stability of a solid solution is increased by the consideration of the Gibbs energy of mixing (equal to the minus entropy of mixing times temperature for an ideal solid solution). This term further decreases the solubility product of the solid solution compared to pure phases. Thus, minute amounts of barite present induce the transformation of celestite to a more stable solid solution ($Sr_{1-x}Br_xSO_4$) if no kinetic constraint for the formation of the solid solution is considered. On the other hand, TOUGHREACT only considers mechanical mixing without Gibbs energy of mixing. This is usually a good approximation for homogeneous solid solutions but in many cases, including $BaSO_4$-$SrSO_4$ solid solutions, this is not appropriate.

The main difference between the two codes lies in the evaluation of equilibrium: OpenGeoSys-GEM calculates thermodynamic equilibrium of the solid solution while TOUGHREACT considers mechanical mixing (i.e. equilibrium is calculated for each phase independently).

The porosity decrease and the corresponding permeability changes in this case study are insignificant and are therefore not presented.

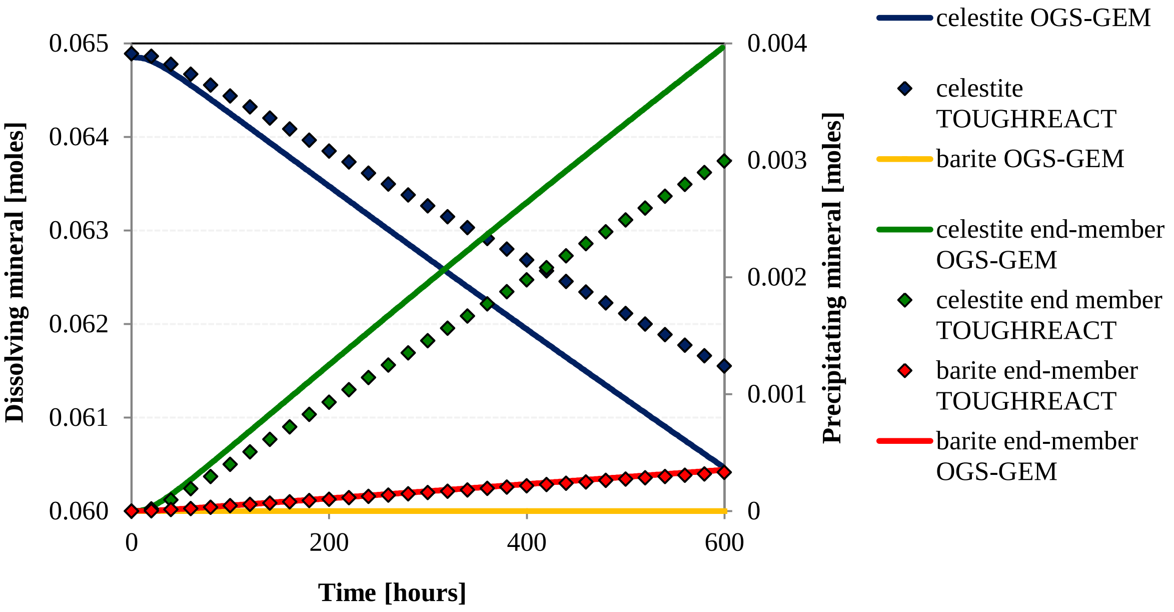

Fig. 16: Evolution of the bulk mineral composition in the flow cell with time. The left axis refers to dissolving pure celestite while the right axis refers to the precipitating phases (end members of the solid solution).

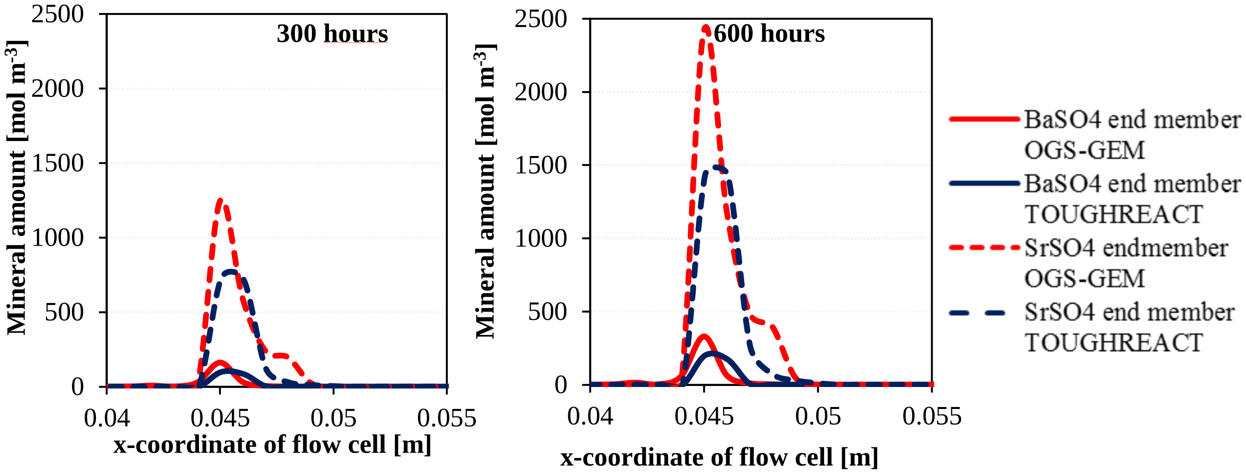

Fig. 17: Amount of $SrSO_4$ and $BaSO_4$ end members across line 1 at 300 and 600 hours.

5. Conclusions

We conducted 2D numerical experiments to benchmark fluid flow and reactive transport calculations. In the 4 presented benchmark cases, we studied several process couplings, such as flow and conservative mass transport and the effect of liquid phase density on the advective-diffusive transport of solutes. In addition, kinetically controlled dissolution/precipitation reactions causing porosity changes, and mineral changes involving the formation of a solid solution were investigated. Codes involved in the testing were OpenGeoSys-GEM, PFlotran, TOUGH2 and CORE2D. In all cases a good qualitative agreement of the results were observed, as long as the same material parameters and parameterization were considered (same reactive surface area model, porosity update and the same porosity-permeability relationship). Differences in the implementation of directional dispersion tensor explained most of the observed small differences, even for the more complex cases. The investigated system behaviour is robust against such differences. For the solid solution case, the implemented conceptual models and formulations of solid solution phases in the different codes matter a lot, in particular for calculating the solubility-controlled concentration of dissolved species. In contrast, the porosity evolution is not sensitive on the implemented solid solution approach.

References

Archie, G., 1942. The electrical resistivity log as an aid in determining some reservoir characteristics. Trans. AIME, 146, 54-62.

Alt-Epping, P., Diamond, L.W., Häring, M.O., Ladner, F., Meier, D.B., 2013a. Prediction of water-rock interaction and porosity evolution in a granitoid-hosted enhanced geothermal system, using constraints from the 5 km Basel-1 well. Appl. Geochem., 38, 121-133.

Alt-Epping, P., Waber, H.N., Diamond, L.W., Eichinger, L., 2013b. Reactive transport modeling of the geothermal system at Bad Blumau, Austria: Implications of the combined extraction of heat and CO_2. Geothermics, 45, 18-30.

Bear, J., 1972. Dynamics of Fluids in Porous Media. Dover Publications Inc., New York.

Berner, U., Kulik, D.A., Kosakowski, G., 2013. Geochemical impact of a low-pH cement liner on the near field of a repository for spent fuel and high-Level radioactive waste. Phys. Chem. Earth, 64, 46-56.

Bildstein, O., Kervévan, C., Lagneau, V., Delaplace, P., Crédoz A., Audigane, P., Perfetti, E., Jacquemet, N., Jullien, M., 2010. Integrative modeling of caprock integrity in the context of CO_2 storage: Evolution of transport and geochemical properties and impact on performance and safety assessment. Oil Gas Sci. Technol. IFP, 65(3), 485-502.

Bruno, J., Bosbach, D., Kulik, D., Navrotsky, A., 2007. Chemical thermodynamics of solid solutions of interest in radioactive Waste Manage.: A state-of-the art report. Chemical Thermodynamics, 10. Eds. F.J. Mompean, M. Illemassene, J. Perrone, OECD, Issy-les-Moulineaux.

Class, H., Ebigbo, A., Helmig, R., Dahle, H.K., Nordbotten, J.M., Celia, M.A., Aubigane, P., Darcis, M., Ennis-King, J., Fan, Y., Flemisch, B., Gasda, S.E., Jin, M., Krug, S., Labregere, D., Beni, A.N., Pawar, R.J., Sbai, A., Thomas, S.G., Trenty, L., Wei, L., 2009. A benchmark study problems related to CO_2 storage in geologic formations. Computat. Geosci., 13(4), 409-434.

Cochepin, B., Trotignon, L., Bildstein, O., Steefel, C.I., Lagneau, V., van der Lee, J., 2008. Approaches to modelling coupled flow and reaction in a 2D cementation experiment. Adv. Water Resour., 31(12), 1540-1551.

Diamond, L.W., Alt-Epping, P., 2014. Predictive modelling of mineral scaling, corrosion and the performance of solute geothermometers in a granitoid-hosted, enhanced geothermal system. App. Geochem., 51, 216-228.

De Windt, L., Pellegrini, D., van der Lee, J., 2004. Coupled modeling of cement/claystone interactions and radionuclide migration. J. Contam. Hydrol., 68(3-4), 165-182.

De Windt, L., Badredinne, R., Lagneau, V., 2007. Long-term reactive transport modelling of stabilized/solidified waste: from dynamic leaching tests to disposal scenarios. J. Hazard. Mater., 139(3), 529–536.

Dove, P.M., Czank, C.A., 1995. Crystal chemical controls on the dissolution kinetics of the isostructural sulfates: Celestite, anglesite, and barite. Geochim. Cosmochim. Acta, 56(10), 4147-4156.

Gaucher, E.C., Blanc, P., 2006. Cement/clay interaction - a review: Experiments, natural analogues, and modelling. Waste Manage., 26(7), 776-788.

Gaus, I., Azaroual, M., Czernichowski-Lauriol, I., 2005. Reactive transport modelling of the impact of CO_2 injection on the clayey cap rock at Sleipner (North Sea). Chem. Geol., 217(3-4), 319–337.

Hayek, M., Kosakowski, G., Churakov, S., 2011. Exact analytical solutions for a diffusion problem coupled with a precipitation-dissolution reaction and feedback of porosity change, Water Resour. Res., 47, W07545.

Hayek, M., Kosakowski, G., Jakob, A., Churakov, S.V., 2012. A class of analytical solutions for multidimensional multispecies diffusive transport coupled with precipitation-dissolution reactions and porosity changes, Water Resour. Res., 48, W03525.

Helgeson, H.C., Delany, J.M, Nesbitt, H.W., Bird, D.K., 1978. Summary and critique of the thermodynamic properties of Rock-Forming Minerals, Amer. J. Sci., 278A, 229.

Helgeson, H.C., Kirkham, D.H., Flowers, G.C., 1981. Theoretical prediction of the thermodynamic behavior of aqueous electrolytes at high pressures and temperatures: IV. calculation of activity coefficients, osmotic coefficients, and apparent molal and standard and relative partial molal properties to 600°C and 5 KB. Am. J. Sci., 281, 1249-1516.

Hummel, W., Berner, U., Curti, E., Pearson, F.J., Thoenen, T., 2002. Nagra/PSI chemical thermodynamic data base 01/01. Universal Publishers, Parkland, Florida.

Jamieson-Hanes, J.H., Amos, R.T., Blowes, D.W., 2012. Reactive transport modeling of Chromium Isotope Fractionation during Cr(IV) Reduction. Environ. Sci. Technol., 46(24), 13311-13316.

Johnson, J.W., Oelkers, E.H., Helgeson, H.C., 1992. SUPCRT92: A software package for calculating the standard molal thermodynamic properties of minerals, gases, aqueous species, and reactions from 1 to 5000 bar and 0 to 1000 °C. Computat. Geosci., 18(7), 899-947.

Katz, G.E., Berkowitz, B., Guadagnini, A., Saaltink M.W., 2011. Experimental and modeling investigation of multicomponent reactive transport in porous media. J. Contam. Hydrol., 120-121, 27-44.

Kelley, K.K., 1960, Contributions to the data in theoretical metallurgy XIII: High temperature heat content, heat capacities and entropy data for the elements and inorganic compounds. U.S. Bureau of Mines Bulletin 584. United States.

Kosakowski, G., Berner, U., 2013. The evolution of clay rock/cement interfaces in a cementitious repository for low and intermediate level radioactive waste. Phys. Chem. Earth, A/B/C, 64, 65-86.

Kosakowski, G., Watanabe, N., 2014. OpenGeoSys-Gem: A numerical tool for calculating geochemical and porosity changes in saturated and partially saturated media. Phys. Chem. Earth, 70-71, 138-149.

Kulik, D.A., Wagner, T., Dmytrieva, S.V., Kosakowski, G., Hingerl, F.F., Chudnenko, K.V., Berner, U., 2013. GEM-Selektor geochemical modeling package: revised algorithm and GEMS3K numerical kernel for coupled simulation codes. Computat. Geosci., 17(1), 1-24.

Lagneau, V., 2000. Influence des processus géochimiques sur le transport en milieu poreux : application au colmatage de barrières de confinement potentielles dans un stockage en formation géologique. PhD Thesis, Ecole des Mines de Paris.

Lagneau, V., van der Lee, J., 2010. Operator-splitting-based reactive transport models in strong feedback of porosity change: The contribution of analytical solutions for accuracy validation and estimator improvement. J. Contam. Hydrol., 112(1-4), 118-129.

Lichtner, P., Karra, S., Hammond, G., Lu, C., Bisht, G., Kumar, J., Mills, R., Andre, B., 2015. PFLOTRAN user manual: A massively parallel reactive flow and transport model for describing surface and subsurface processes. United States.

Palandri, J.L., Kharaka, Y.K., 2004. A compilation of rate parameters of water mineral interaction kinetics for application to geochemical modelling. US Geological Survey, Menlo Park, California.

Poonoosamy, J., Kosakowski, G., Van Loon L. R. and Mäder, U., 2015. Dissolution-precipitation processes in tank experiments for testing numerical models for reactive transport calculations: Experiment and modelling. J. Contam. Hydrol., 177-178, 1-17.

Prieto, M., 2009. Thermodynamics of solid solution-aqueous solution systems. Rev. Mineral. Geochem., 70, 47-85.

Pruess, K., Oldenburg, C.M., Moridis, G., 1999. TOUGH2 User's Guide, Version 2.0. Lawrence Berkeley National Laboratory Report LBNL-29400. Berkeley, California.

Samper, J., Yang, C., Montenegro, L., 2003. CORE2D version 4: A code for non-isothermal water flow and reactive solute transport. User's manual. University of La Caruna, Spain.

Samper, J., Xu, T., Yang, C., 2009. A sequential partly iterative approach for multicomponent reactive transport with CORE2D. Computat. Geosci., 13, 301-316.

Shao, H., Dmytrieva, S.V., Kolditz, O., Kulik, D.A., Pfingsten, W., Kosakowski, G., 2009. Modeling reactive transport in non-ideal aqueous–solid solution system. Appl. Geochem., 24(7), 1287-1300.

Shock, E.L., Helgeson, H.C., Sverjensky, D.A., 1989. Calculation of the thermodynamic and properties of aqueous species at high pressures temperatures: Standard partial molal properties inorganic neutral species. Geochim. Cosmochim. Acta, 53(9), 2157-2183.

Shock, E.L, Sassani, D.C., Willis M., Sverjensky, D.A., 1997. Inorganic species in geologic fluids: Correlations among standard molal thermodynamic properties of aqueous ions and hydroxide complexes. Geochim. Cosmochim. Acta, 61(5), 907-950.

Steefel, C.I., Appelo, C.A.J., Arora, B., Jacques, D., Kalbacher, T., Kolditz, O., Lagneau, V., Lichtner, P.C., Mayer, K.U., Meeussen, J.C.L., Molins, S., Moulton, D., Shao, H., Šimůnek, J., Spycher, N.F., Yabusaki, S.B., Yeh, G.T., 2015. Reactive transport codes for subsurface environmental simulation. Computat. Geosci., 19, 445-478.

Sverjensky, D.A., Shock, E.L., Helgeson, H.C., 1997. Prediction of the thermodynamic properties of aqueous metal complexes to 1000°C and 5 kb. Geochim. Cosmochim. Acta, 61, 1359-1412.

Tartakovsky, A.M., Redden, G., Lichtner, P.C., Scheibe, T.D., Meakin, P., 2008. Mixing-induced precipitation: Experimental study and multiscale numerical analysis. Water Resour. Res., 44, W06S04.

van der Lee, J., De Windt, L., Lagneau V., Goblet, P., 2003. Module oriented modeling of reactive transport with HYTEC. Comput. Geosci., 29(3), 265-275.

Wagner, T., Kulik, D.A., Hingerl, F.F., Dmytrieva, S.V., 2012. GEM-Selektor geochemical modeling package: TSolMod C++ class library and data interface for multicomponent phase models. Can. Mineral., 50, 1173-1195.

Wanner, C., Eggenberger, U., Mäder, U., 2012. A chromate-contaminated site in southern Switzerland –part 2: Reactive transport modeling to optimize remediation options. Appl. Geochem., 27(3), 655-662.

Wanner, C., Sonnenthal, E.L., 2013. Assessing the control on the effective kinetic Cr isotope fractionation factor: A reactive transport modeling approach. Chem. Geol., 337-338, 88-98.

Wanner, C., Peiffer, L., Sonnenthal, E.L., Spycher, N., Iovenitti, J., Kennedy, B.M., 2014. Reactive transport modeling of the Dixie Valley geothermal area: Insights on flow and geothermometry. Geothermics, 51, 130-141.

Wanner, C., Druhan, J.L., Amos, R.T., Alt-Epping, P., Steefel C.I., 2015. Benchmarking the simulation of Cr isotope fractionation. Computat. Geosci., 19, 497-521.

Wagman, D.D., Evans, W.H., Parker, V.B., Schumm, R.H., Halow, I., Bailey, S.M., Churney, K.L., Nuttall, R.L., 1982. The NBS Tables of chemical and thermodynamic properties. Selected values for inorganic and C1 and C2 organic substances in SI units. Jour. Phys. Chem. Ref. Data, 11(2), 392.

Xie, M., Mayer, K.U., Claret, F., Alt-Epping, P., Jacques, D., Steefel, C., Chiaberge, C., Šimůnek, J., 2015. Implementation and evaluation of permeability-porosity and tortuosity-porosity relationships linked to mineral dissolution-precipitation. Computat. Geosci., 19, 655-671.

Xu, T., Spycher, N., Sonnenthal, E., Zhang, G., Zheng, L., Pruess, K., 2011. TOUGHREACT Version 2.0: A simulator for subsurface reactive transport under non-isothermal multiphase flow conditions. Comput. Geosci., 37(6), 763-774.

Appendix

Solid solution: Activities of the end-members of a solid solution in thermodynamic equilibrium are related to activities of aqueous ions by the following set of equations (Prieto, 2009):

$$\{SO_4^{2-}\} = a_{SrSO_4}{K^0}_{SrSO_4} = \gamma_{SrSO_4}X_{SrSO_4}{K^0}_{SrSO_4} \qquad (18)$$

$$\{SO_4^{2-}\} = a_{BaSO_4}{K^0}_{BaSO_4} = \gamma_{BaSO_4}X_{BaSO_4}{K^0}_{BaSO_4} \qquad (19)$$

where a_i, γ_i and X_i are the activity, the activity coefficient, and the mole fraction of end member i, respectively. For a simple ideal solid solution, γ_i is equal to 1 such that the activity of an end-member is equal to its mole fraction:

$$a_{BaSO_4} = X_{BaSO_4} \qquad (20)$$

$$a_{SrSO_4} = X_{SrSO_4} \qquad (21)$$

The solidus and solutus curves are derived from the following formula:

$$log\sum\prod(solidus) = \log\left(a_{SrSO_4}{K^0}_{SrSO_4} + a_{BaSO_4}{K^0}_{BaSO_4}\right) \qquad (22)$$

$$log\sum\prod(solutus) = \log\left(\frac{1}{x_{Ba^{2+}}/{K^0}_{BaSO_4} + x_{Sr^{2+}}/{K^0}_{SrSO_4}}\right) \qquad (23)$$

The solidus x-scale refers to the mole fraction of the end members while the solutus x-scale is calculated as:

$$x_{Ba^{2+}} = \frac{a_{BaSO_4}{K^0}_{BaSO_4}}{\sum\prod(solidus)} \qquad (24)$$

$$x_{Sr^{2+}} = 1 - x_{Ba^{2+}} \qquad (25)$$

N.B: in this section only (appendix), ‘a’ refers to activity different from ‘a’ used in the manuscript which refers to surface area per volume of the mineral phase.

Influence of grid discretization: Breakthrough curves for ports ‘c’ and ‘d’ for different discretization.

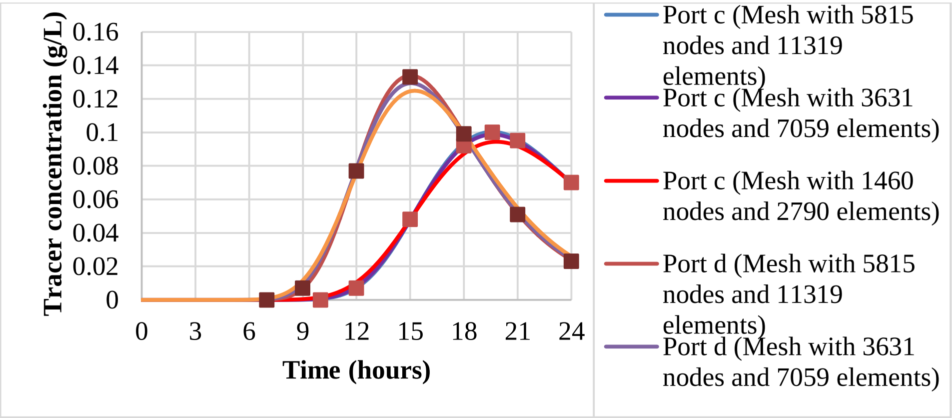

Fig. 18: Effect of grid discretization produced by CORE2D.

Chapter 6: Concluding remarks and future work

Concluding remarks and future work

We developed a reactive transport experiment where porosity changes were induced by chemical reactions. It can be used to develop upscaling concepts and test concepts implemented in continuum scale reactive transport codes. Our experiment was carried out in a flow cell, which was filled with a porous reactive layer of celestite ($SrSO_4$) sandwiched between two layers of non-reactive quartz sand (SiO_2). The reactive layer consisted of a bimodal grain size distribution of celestite crystals with grain diameters below 63 µm and between 250 - 400 µm. The pore diameter in the reactive layer varied between 10 - 500 µm. The inlet and outlet of the tank were positioned to create an asymmetric flow field. A 0.3 M barium chloride solution was injected into the fully saturated porous media at a flow rate of 20 µL min^{-1}. During the course of the experiment, the compositions of the effluent and the pressure in the tank were monitored.

The injection of a highly concentrated barium chloride solution into the porous medium that contained a pore water of lower density changed the initially stationary flow field and introduced density-driven flow. As the barium chloride reached the celestite region, dissolution of celestite was initiated and barite precipitated. The replacement of celestite by barite induced a porosity decrease. The change in solute composition also affected the fluid density. A dye tracer pulse injected in the tank for visualization of the flow field before and after reaction, as well as pressure measurements suggested a strong decrease in permeability of the reactive layer. The permeability decrease is explained by newly formed barite phases in the pore space.

Post mortem analysis involving synchrotron based µ-XRF, µ-XRD and scanning electron microscopy (SEM) were used to investigate the changes at pore scale in the reactive medium. The newly formed phases were found, an oriented growth of barite micro-crystals on large celestite crystals (epitaxial growth) and a nano-crystalline barite phase with residues of celestite crystals in the pore interstices. The observed temporal precipitation sequence showed that at least in the first stages of the reaction, the formation of a nano-crystalline barite phase resulting from homogeneous nucleation appears before the epitaxial barite which is formed by heterogeneous nucleation. However, classical nucleation theory predicts that the induction time for homogeneous nucleation and heterogeneous nucleation is 9 hours and 1 hour respectively. This apparent inconsistency may be resolved by considering that heterogeneous growth on celestite substrates cannot be detected in early stages of the process. From SEM images, a rim thickness of 3 µm in 300 hours is detected for epitaxial barite which corresponds to a growth rate of 10 nm $hour^{-1}$. At very high supersaturation of $BaSO_4$, both phases start to build. However, whereas homogeneous nucleation once started, is a chain-reaction like process (very fast), epitaxial growth of barite on the celestite crystals will proceed at considerably slower rates. Once the small celestite crystals are consumed or isolated from the solution, or the supply of $BaCl_2$ is locally interrupted, the supersaturation of barite decreases rapidly. The supply of sulfate is slower since only larger celestite crystals with low specific surface area are involved. Under such conditions, homogeneous nucleation is excluded and only epitaxial growth is possible. The rim of crystalline barite grows on the surface of the large celestite crystals. The nano-crystalline phase cements all the thinner and larger celestite particles together, creates bottlenecks and isolates pores in some cases.

It should be noted that the recrystallization of nano-crystalline to micro-crystalline (epitaxial) barite is also possible. The driving force for this replacement process is explained by the larger surface area contribution to the Gibbs free energy of the nanocrystals which results in a higher solubility of the nano-crystalline barite compared to that of epitaxial barite. As long as nano-crystalline barite is present, the ion activity product $[Ba^{2+}][SO_4^{2-}]$ will be slightly larger than the solubility product of macro-crystalline barite, i.e. there will be a tendency for further precipitation of macro-crystalline barite and dissolution of nano-crystalline barite. This particle size effect has been described in detail by Schindler (1967). Recrystallization processes can be considered in pores where both nano-crystalline and micro-crystalline barite phases are present and when a diffusive transport regime is reached.

Putnis and Mauthe (2001), Stack et al. (2014) and Prieto (2014) reported the dependence of nucleation kinetics on pore size in porous medium. The effect of reducing the pore size is an inhibition for nucleation. In our experiments, the initial pore size distribution is quite heterogeneous with pore sizes varying between 10 and 500 µm. Initially, the non-cemented grains of celestite have a pore connectivity which is larger than in a porous rock (e.g. sandstone) where grains are cemented. In our experiments, nano-barite crystals appear first along the main flow pathways and afterwards across the entire celestite medium. A preferential formation of nano-barite in the larger pores was difficult to detect in our system, probably because pore connectivities are larger compared to the studies cited. For an averaged pore size of 100 µm, the calculated induction time for the formation of barite clusters for both nucleation mechanisms was less than 10 hours and even less for larger pores (500 µm). For small pores of size 10 µm, the induction time for was ~ 4 hours for heterogeneous nucleation and 319 hours for homogeneous nucleation. With our SEM measurements, it was difficult to observe a dependence of precipitation kinetics on pore-size. For a better evaluation of the possible dependence of nano-crystalline formation in larger pores, tomography measurements will be performed at the TOMCAT beamline at PSI. A test measurement was successfully performed and a scan of a cross-sectional cut is given in Fig. 1.

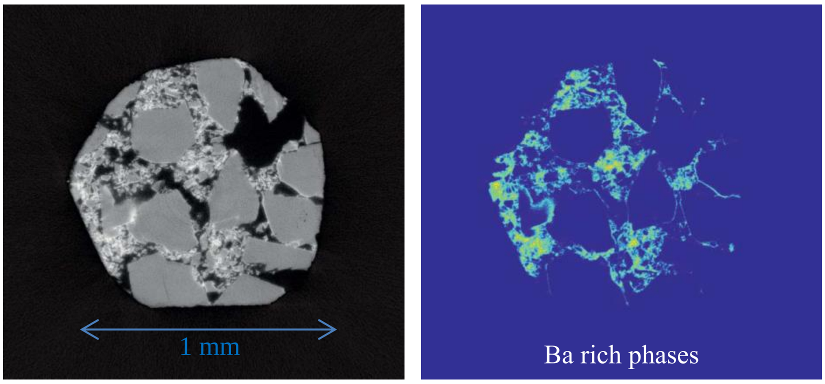

Fig. 1: Cross section of a core sample with 1 mm diameter of the reactive medium after 28 hours of barium chloride injection. Scan performed with a beam acceleration of 36 kV. The Ba-rich phases are present as nanophase and as a thin epitaxial barite rim on the larger celestite crystals.

At a continuum scale the experiments were modelled with the reactive transport code OpenGeosys-GEM. Tracer tests, with non-reactive tracers performed prior to barium chloride injection, as well as changes in the flow field due to injection of a non-reactive liquid with different (higher) liquid density, were well matched. For the successful reproduction of reactive transport experiments additional experimental data on the microstructure of the reactive medium were needed. Only a model that included two populations of celestite grains, with different kinetic rates for dissolution, successfully reproduced the experimentally observed evolution of the bulk amounts of minerals with time. Still this model did not match the measured pressure evolution, without changing the default parameters in the porosity-permeability relationship to extreme values. In the experiments, we observed an additional cemented zone at the interface between the sand and the reactive layer. We were not able to measure the initial and final porosity and transport properties of this layer, as we were unable to extract undisturbed samples of this interface. Therefore we modelled this with an additional 1 mm thick layer at the interface. This layer had the same porosity-permeability relationship as the reactive layer, although we had to modify the initial porosity in order to get a reasonable match to the experimental pressure evolution. It is important to stress that such a procedure does not produce properly upscaled model parameters and such a parametrized model cannot be used for predictions.

In some experiments, small fractures or preferential flow paths at the top of the reactive medium occurred after 100 hours of injecting $BaCl_2$, often only noticeable in pressure recordings. Each time a crack opened, the pressure difference in the tank dropped because of the larger permeability of the crack. The formation of cracks or preferential flow path controls the chemistry of the system. Reactants bypass large portions of the reactive medium leading to a complete change of kinetics and transport in the system. These processes were not taken into account in our modelling.

OpenGeoSys-GEM calculations were also compared to other codes namely PFlotran, TOUGH2 and CORE2D within the SeS bench initiative (Steefel et al., 2015). In all cases a good qualitative agreement of the results were observed, as long as the same material parameters and parameterization were considered. Differences in the implementation of directional dispersion tensor explained most of the observed small differences, even for the more complex cases. Such a comparison enabled code users and developers to verify the different couplings implemented in the different codes, but cannot be used to validate our parametrized model.

At the continuum scale kinetic model for the dissolution of celestite, the reactive surface area was a fitting parameter. In our model setup the reactive surface area is the only available parameter to adjust the dissolution rate; therefore it is used as a “fudge factor”. The reactive surface areas for the two celestite grain population were not set to the measured BET (Brunauer-Emmett-Teller) surface areas since this gave dissolution rates which were unrealistically large. The fitted values for reactive surface areas were orders of magnitude smaller than the BET surface area. As was reported by Molins et al. (2012), reactive surface which is measured by BET or geometrically estimated from the physical grain size does not consider the accessibility of water or aqueous solution to the reactive phases in the porous medium(Maher et al. 2006; Peters, 2009). The dissolution process is not homogeneous and the reactive surface area represents the portion of the mineral surface area exposed to the aqueous solution and actively participating in the reaction. It may be much lower than the total surface area (Helgeson et al., 1984). It is therefore generally considered that the total available surface area is between one and three orders of magnitude larger than the actual reactive surface area (Gaus et al., 2005; Xu et al., 2007; Scislewski and Zuddas, 2010). In addition, the reactive surface areas of large celestite crystals are further decreased in time by the precipitating barite phase coating and passivating their surfaces.

Tartakovsky et al. (2008a) showed that the use of the ADRE (advection-dispersion reaction equation) is not completely appropriate for describing very strong local concentration gradients resulting in localised precipitation. However, in contrast to Tartakovsky et al. (2008a) concentration gradients and mineral precipitation in our experiments are not completely controlled by diffusive/dispersive mixing of solutes. Concentration gradients are also heavily influenced by the kinetic control of the dissolving mineral phase. Slow mineral dissolution suppresses strong concentration gradients and localised precipitation.

Without detailed knowledge of micro-structural changes it was not possible to reproduce all aspects of the system. In this system setup, micro-features below the continuum scale exist and need to be approximated in the model, e.g., the existence of an additional thin reactive layer with different transport properties.

It should be noted that the experimental observations presented in chapter 3 showed the limits of the continuum scale reactive transport model presented in chapter 2. Although kinetic effects were implemented by fixing two distinct rates for the dissolution of large and small celestite crystals, instantaneous precipitation of barite was assumed as soon as oversaturation occurred. Precipitation kinetics and metastability of supersaturated solutions i.e. the conditions under which nucleation cannot occur despite high supersaturation (Prieto et al., 1990), were neglected. The results from mineralogical-microscopic investigation clearly show that precipitation kinetic effects related to metastability of supersaturated solutions and distinct nucleation mechanisms are important. In addition they depend on the transport regime and have certainly an impact on the evolution of porosity, permeability and diffusivity.

The validity of our kinetic approach for describing dissolution and precipitation reactions involved in our system can be tested by investigating the same reactive setup under different transport regime. We conducted additional experiments in a quasi 1D column with a constant flow rate. The column was filled with a porous medium consisting of small celestite grains (< 63 µm) sandwiched between two layers of sand. The average pore size for the column experiments was estimated to be 10 µm. 0.1 M $BaCl_2$ solution was injected in the system at a flow rate of 56.5 µL min^{-1} which results in higher advective fluxes than in the 2D tank experiment. Under such conditions, homogeneous nucleation leading to a nano-crystalline barite phase was completely suppressed. Barite precipitated as a coating on the surface of small celestite crystals (heterogeneous nucleation) as shown in Fig. 2a. The breakthrough curves (Fig 2b) show an initial peak in Ba^{2+} concentration which then decreased after 14 hours. The initial maximum Ba^{2+} concentration observed was due to the metastability of supersaturated solutions. Between 14 and 25 hours, the rate of dissolution for celestite and precipitation of barite is constant. Afterwards, the dissolution of celestite slowed down, decreasing the concentration of Sr^{2+} ions in the effluent. As barite precipitated as an overgrowth on the surface area of celestite crystals, this decreased the reactive surface slowing down the dissolution of the latter.

In Fig. 2b also results from the (continuum scale) reactive transport models, calibrated on the 2D experiments, are plotted. The calibrated model could qualitatively reproduce the experimental observation, however with some significant discrepancies visible in the cationic breakthrough.

Our model does not take into account metastable conditions and also passivation of celestite crystals. The modelled reactive surface area of celestite is a linear function of its volume amount, and therefore cannot reproduce the decrease in reactive surface area as the reaction proceeds. These results prompt for future improvements of the reactive transport model.

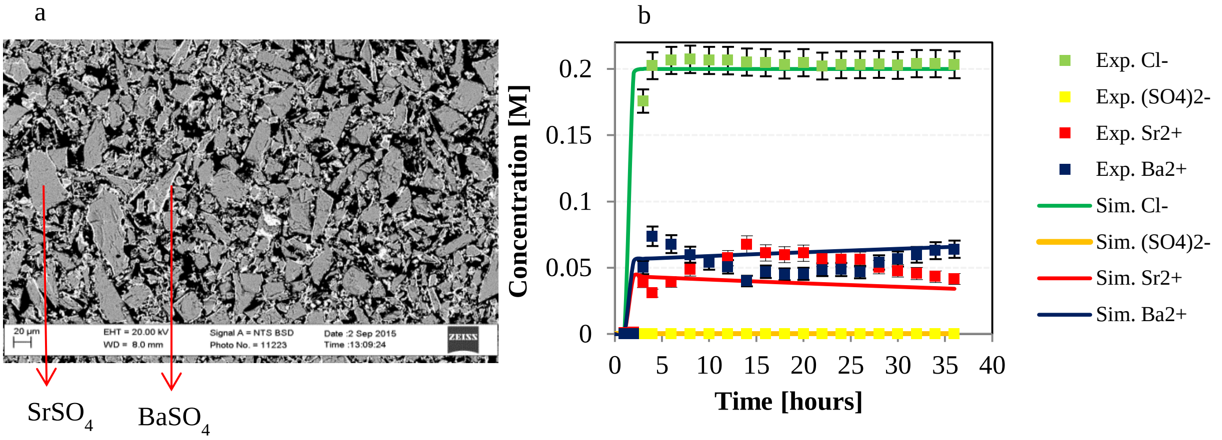

Fig. 2: (a) Scanning electron microscopy image (back scattered electron mode) of the reactive medium after reaction. The grey colour corresponds to celestite crystal while the brighter rims correspond to barite. (b) The experimental (Exp.) and simulated (Sim.) ionic breakthrough curves measured at the outlet for 1D setup.

Recently Chagneau et al. (2015), performed counter diffusion experiments. They investigated celestite precipitation in the pore space of a compacted sand column. After 15 days, the precipitation ceased, the pore space in the precipitation zone remained fully connected with about 25 % porosity reduction. They modelled their system evolution with a continuum reactive transport model which failed to reproduce the celestite precipitation accurately. Their continuum scale model either underestimated the remaining connected porosity in the precipitation zone, or overestimated the amount of precipitate. Their findings showed that pore-scale precipitation transforms a micro-porous system into a system consisting of micro and nano pores. They conclude that it is necessary to implement a modified, extended Archie's law to the reactive transport model. Fatnassi (2015) conducted similar counter diffusion experiments, involving the in situ precipitation of barite and gypsum in chalk. Although barite has a smaller molar volume than gypsum, its precipitation in chalk caused a decrease in diffusivity at an earlier stage than gypsum. This was explained by the difference in morphology/nature of the newly formed phases in the pore space which cannot be approximated by a continuum scale model (with Archie's law). The modelling of the experiments with a continuum scale model either overestimated the impact of gypsum precipitates in the pore space on diffusivity or underestimated the impact of barite precipitates in the pore space on diffusivity.

The inability of continuum reactive transport codes to accurately reproduce experimental data on porosity, permeability and diffusivity change is because these models consider the medium as averaged domains with macroscopic flow and transport properties. The averaging process also includes geochemical parameters such as reactive surface area and reaction rates. There is thus a need to properly upscale pore scale processes to the continuum scale. In terms of reactive transport, all relevant transport properties, as well as the relevant parameters controlling the reactions have to be upscaled in a consistent way. Pore scale modelling can be used to investigate physicochemical processes (nucleation mechanism, passivation of surfaces, creation of unconnected porosities etc...) that are not resolved in continuum scale models. The results can be used to parameterize constitutive equations to introduce pore-scale corrections into macroscopic (continuum) reactive transport models.

The next logical step in evaluation of the experiments described in this work would be thus to model the change of the pore space taking into account realistic approaches for celestite dissolution and barite precipitation. Molin et al. (2012) reviewed the different pore scale approaches: pore network (Li et al., 2006; Algive et al., 2010), Lattice Botlzmann (Kang et al., 2006; Van Leemput et al., 2007; Kang et al., 2010a; 2010b; Huber et al., 2014) and particle methods (Tartakovsky et al., 2007a; Tartakowski et al., 2007b; 2008b). Hybrid models combining the microscopic description of the pore scale approach and the continuum scale approach have also been developed (Van Leemput et al., 2007; Battiato et al., 2011). Lattice Boltzmann modelling is a suitable tool in the attempt of describing our celestite-barite system at the pore scale. Lattice Boltzmann methods have the advantage of considering complex geometries of the sample which can be extracted directly from our microscopic images and tomograms (Fig. 1). In addition, they allow modelling a wide range of transport regimes and at the same time getting estimates of averaged transport parameters. They can be used to parameterize porosity-permeability relationships in our system (Rosen et al., 2012), as well as the reactive surface area model. An upscaling of dissolution/precipitation rates from pore to continuum scale, as was done by Noirel et al. (2012) and Molins et al. (2014), could also be an option for the description of our system.

We would like to stress that microscopic understanding of the system is fundamental for modelling on pore and continuum scale. Our experimental approach consisting of a simple chemical setup cannot be used directly for safety assessment of engineered barrier systems (nuclear waste repositories, geologic CO_2 storage, etc.). However, they allow an understanding of pore scale processes as well as macroscopic changes. In the presented simplified example, in order to do realistic modelling in terms of time, a good knowledge of the system (pore size distribution, surface area of mineral) and different processes (nucleation, kinetics of dissolution and precipitation) are required. Such a detailed understanding of realistic complex systems (e.g. clay/cement interfaces in nuclear waste repositories) is needed in order to do meaningful predictive modelling.

References

Algive, L., Bekri, S., Vizika, O., 2010. Pore-network modeling dedicated to the determination of the petrophysical-property changes in the presence of reactive fluid. SPE J., 15(3), 618-633.

Battiato, I., Tartakovsky, D.M., Tartakovsky, A.M., Scheibe, T.D., 2011. Hybrid models of reactive transport in porous and fractured media. Adv. Water Resour., 34(9), 1140-1150.

Chagneau, A., Claret, F., Enzmann, F., Kersten, M., Heck, S., Madé, B., Schäfer, T., 2015. Mineral precipitation‑induced porosity reduction and its effect on transport parameters in diffusion‑controlled porous media. Geochem. Trans., 16:13.

Gaus, I., Azaroual, M., Czernichowski-Lauriol, I., 2005. Reactive transport modelling of the impact of CO_2 injection on the clayey cap rock at Sleipner (North Sea). Chem. Geol., 217(3-4), 319-337.

Helgeson, H.C., Murphy, W.M., Aagaard, P., 1984. Thermodynamic and kinetic constraints on reaction rates among minerals and aqueous solutions. II. Rate constants, effective surface area, and the hydrolysis of feldspar. Geochim. Cosmochim. Acta, 48(12), 2405-2432.

Huber, C., Shafei, B., Parmigiani, A., 2014. A new pore-scale model for linear and non-linear heterogeneous dissolution and precipitation. Geochim. Cosmochim. Acta, 124, 109-130.

Fatnassi, I., 2015. Impact de la variation de la porosité sur le transport diffusif :expérimentation vs simulation. PhD Thesis in press, Université Montpelier II.

Kang, Q., Lichtner, P.C., Zhang, D., 2006. Lattice Boltzmann pore scale model for multicomponent reactive transport in porous media. J. Geophys. Res., 111, B05203.

Kang, Q., Lichtner, P.C., Janecky, D.R., 2010a. Lattice Boltzmann method for reacting flows in porous media. Adv. Appl. Math. Mech., 2(5), 545-563.

Kang, Q., Lichtner, P.C., Viswanathan, H.S., Abdel-Fattah A.I., 2010b. Pore scale modeling of reactive transport involved in geologic CO_2 sequestration. Transp. Porous Med., 82(1), 197-213.

Li, L., Peters, C. A., Celia, M. A., 2006. Upscaling geochemical reaction rates using pore-scale network modeling. Adv. Water Resour., 29(9), 1351-1370.

Maher, K., Steefel, C.I., DePaolo, D.J., Viani, B.E., 2006. The mineral dissolution rate conundrum: insights from reactive transport modelling of U isotopes and pore fluid chemistry in marine sediments. Geochim. Cosmochim. Acta, 70(2), 337-363.

Molin, S., Trebotich, D., Steefel, C. I., Shen, C., 2012. An investigation of the effect of pore scale flow on average geochemical reaction rates using direct numerical simulation, Water Resour. Res., 48, W03527.

Molins, S., Trebotich, D., Yang, L., Ajo-Franklin, J.B., Ligocki, T.J., Shen, C., Steefel, C.I., 2014. Pore-scale controls on calcite dissolution rates from flow-through laboratory and numerical experiments. Environ. Sci. Technol., 48(13), 7453-7460.

Noiriel, C., Steefel, C. I., Yang, L., Ajo-Franklin, J., 2012. Upscaling calcium carbonate precipitation rates from pore to continuum scale. Chem. Geol., 318-319, 60-74.

Peters, C.A., 2009. Accessibilities of reactive minerals in consolidated sedimentary rock: An imaging study of three sandstones. Chem. Geol., 265(1-2), 198-208.

Prieto, M., Putnis, A., Fernández-Díaz, L., 1990. Factors controlling the kinetics of crystallization: supersaturation evolution in porous medium. Application to barite crystallization. Geol. Mag., 127(6), 485-495.

Prieto, M., 2014. Nucleation and supersaturation in porous media (revisited). Mineral. Mag., 78(6), 1437-1447.

Putnis, A., Mauthe, G., 2001. The effect of pore size on cementation in porous rocks. Geofluids, 1, 37-41.

Rosén, T., Eller, J., Kang, J., Prasianakis, N.I., Mantzaras, J., Buchi, F.N., 2012. Saturation dependent effective transport properties of PEFC gas diffusion layers. J. Electrochem. Soc. 159(9), F536-F544.

Schindler, P.W., 1967. Heterogeneous equilibria involving oxides, hydroxides, carbonates and hydroxides carbonates. Equilibrium Concepts in Natural Water Systems. Adv. Chem. Ser., 67, 197-221.

Scislewski, A., Zuddas, P., 2010. Estimation of reactive mineral surface area during water-rock interaction using fluid chemical data. Geochim. Cosmochim. Acta, 74(24), 6996-7007.

Stack, A.G., Fernandez-Martinez, A., Allard, L.F., Bañuelos, J.L., Rother, G., Anovitz, L.M., Cole, D.R. Waychunas, G.A., 2014. Pore-size-dependent calcium carbonate precipitation controlled by surface chemistry. Environ. Sci. Technol., 48(11), 6177-6183.

Steefel, C.I., Appelo, C.A.J., Arora, B., Jacques, D., Kalbacher, T., Kolditz, O., Lagneau, V., Lichtner, P.C., Mayer, K.U., Meeussen, J.C.L., Molins, S., Moulton, D., Shao, H., Šimůnek, J., Spycher, N.F., Yabusaki, S.B., Yeh, G.T., 2015. Reactive transport codes for subsurface environmental simulation. Computat. Geosci., 19(3), 445-478.

Tartakovsky, A.M., Meakin, P., Scheibe, T.D., Eichler West, R M., 2007a. Simulations of reactive transport and precipitation with smoothed particle hydrodynamics. J. Comp. Phys., 222(2), 654-672.

Tartakovsky, A.M., Meakin, P., Scheibe, T.D., Wood, B.D., 2007b. A smoothed particle hydrodynamics model for reactive transport and mineral precipitation in porous and fractured porous media. Water Resour. Res., 43, W05437.

Tartakovsky, A.M., Redden, G., Lichtner, P.C., Scheibe, T.D., Meakin, P., 2008a. Mixing-induced precipitation: experimental study and multiscale numerical analysis. Water Resour. Res., 44, W06S04.

Tartakovsky, A.M., Tartakovsky, D.M., Scheibe, T.M., Meakin, P., 2008b. Hybrid simulations of reaction-diffusion systems in porous media. SIAM J. Sci. Comput., 30(6), 2799-2816.

Van Leemput, P., Vandekerckhove, C., Vanroose, W., Roose, D., 2007. Accuracy of hybrid lattice Boltzmann/finite difference schemes for reaction-diffusion systems. SIAM. J. Multiscale Model. Simul., 6(3), 838-857.

Xu, T., Apps, J.A., Pruess, K., Yamamoto, H., 2007. Numerical modeling of injection and mineral trapping of CO_2 with H_2S and SO_2 in a sandstone formation. Chem. Geol., 242(3-4), 319-346.

Erklärung

on the basis of article 28 para. 2 of the RSL05 phil.-nat

Name/First Name: Poonoosamy Jenna

Matriculation Number: 12-132-973

Study program: Earth Sciences

Title of the thesis: Dissolution-Precipitation in Porous Media: Experiments and Modelling

I declare herewith that this thesis is my own work and that I have not used any sources other than those stated. I have indicated the adoption of quotations as well as to article 36 para. 1 lit. r of the University Act of 5 September, 1996 is authorised to revoke the title awarded on the basis of this thesis. I allow herewith inspection in this thesis.

Villigen, 4. January 2015

CV

Jenna Poonoosamy Lagrue

Born on May 25th 1987 in Port-Louis (Mauritius)
✉ : jenna.poonoosamy@gmail.com

Work Experience

Oct. 2012 to present

Paul Scherrer Institute (PSI) Switzerland
Supervised by Dr. Georg Kosakowski, Dr. Luc Van Loon and Dr. Urs Mäder

- **Ph.D. Thesis: Experimental benchmark for testing reactive transport codes.**
  Develop 2D reactive transport experiment involving porosity clogging and model the experiments with the reactive transport code, OpenGeosys-GEM.

2012, 5 months

Commissariat à l'Energie Atomique et aux Energies Alternatives (CEA) France
Supervised by Dr. Romain Dagnélie

- **Master Thesis: Effect of organic matter produced by the radiolysis of radioactive waste on the retention properties of clay**
  Batch sorption and desorption of europium in presence of organics on clay rocks: experiments and modelling.

2011, 5 months

Paul Scherrer Institute (PSI) Switzerland
Supervised by Dr. Claude Degueldre and Dr. Dmitrii Kulik

- **1st year of master internship report: Thermodynamic properties and redox behaviour of actinides in mixed oxide fuels (MOX) using GEM (Gibbs Energy Minimization) simulation**
  Reactions in heterogeneous and homogeneous MOX were approximated as reactions of separate actinide oxide phases and as reactions involving solid solution respectively. Prior to simulations, the solid-solution models were calibrated with experimental data.

2010, 7 weeks

Institut des Sciences Moléculaires d'Orsay (ISMO) France
Supervised by Dr. Sandrine Lacombe

- **3rd year of BSc internship report: Study of radio sensitizing effect of palladium nanoparticles**
  Synthesis of palladium nanoparticles by radiolysis. Measure of the radio sensitizing power of the palladium nanoparticles followed by a comparative study with platinum nanoparticles.

2009, 3 months

Institut de Physique Nucléaire d'Orsay (IPN) France
Supervised by Dr. Olivia Felix and Dr. Romuald Drot

- **2nd year of BSc internship report: Effect of temperature on the sorption of uranyl ion upon magnetite**
  Measure of the sorption edge of uranyl ion upon magnetite at different temperatures followed by a calorimetric approach to explain the unchanged sorption phenomena observed with an increase in temperature.

2006, 8 months

De Chazal Du Mée Consulting Ltd Mauritius
Trainee as financial auditor

Teaching experience France

2009-2010 Oral exams to 2nd year Bachelor students in chemistry in Technical Analysis at the University of Paris Sud 11

2009-2011 Private lessons to secondary school students in Mathematics, Chemistry & Physics.

Education

2013 – to present	**Doctoral degree** at Institute of Geological Sciences, University of Bern.
2009-2012	**High-Level Master of Molecular Physical Chemistry (magistère physico-chimie moléculaire)**. 3 years joint program of Ecole Normale Supérieure of Cachan and University of Paris Sud 11.
2011-2012	**International Master of Nuclear Energy-Fuel cycle with major in radiochemistry**. (Joint master program of University Paris Sud 11, INSTN, ParisTech, Supélec and Centrale Paris).
2007-2010	**Bachelor in Chemistry** at the University of Paris Sud 11.
November 2005	Higher School Certificate (GCE Advanced level) science side delivered by the University of Cambridge Local Examination Syndicate (UCLES)
November 2003	School Certificate (GCE Ordinary level) delivered by UCLES

Peered Reviewed Publications and Book Contributions

Descostes, M., Pointeau, I., Radwan, J., **Poonoosamy, J.**, Lacour, J.L., Menut, D., Vercouter, T., Dagnelie, R.V.H., Validity of EDTA Diffusion Parameters through Clay Rock. *Submitted for publication to Environmental Science & Technology.*

Poonoosamy, J., Curti, E., Kosakowski, G., Van Loon, L. R., Grolimund, D., Mäder U., Barite Precipitation following Celestite Dissolution in a Porous medium: a SEM/BSE and micro XRF/XRD study. *Submitted for publication to Geochimica et Cosmochimica Acta.*

Chollet, M., Martin, P., Degueldre, C., **Poonoosamy, J.**, Belin, R.C., Hennig, C., 2016. Neptunium Characterization in Uranium Dioxide Fuel: Combining a XAFS and a Thermodynamic Approach. Journal of Alloys and Compounds, 662, 448-454.

Poonoosamy, J., Kosakowski, G., Van Loon, L.R., Mäder, U., 2016. Chapter 12, Reactive Transport, in: Kolditz O., Görke U.J., Wang W., Shao H., Bauer S. (eds), Thermo-Hydro-Mechanical-Chemical Processes in Fractured Porous Media: Modelling and Benchmarking-Benchmarking Initiatives, Cham, Springer International Publishing AG.

Poonoosamy, J., Kosakowski G., Van Loon R., Mäder U., 2015. Dissolution-Precipitation Processes in Tank Experiments for Testing Numerical Models for reactive Transport Calculations: Experiments and Modelling. Journal of Contaminant Hydrology, 177-178, 1-17.

Degueldre, C., Pin, S**., Poonoosamy, J**., Kulik, D.A., 2014. Redox state of plutonium in irradiated mixed oxide fuels, Journal of Physics and Chemistry of Solids, 75, 358-365.